Old Dominion University
ODU Digital Commons

Electrical & Computer Engineering Theses & Disssertations

Electrical & Computer Engineering

Summer 2003

Photonic Crystals: Modeling and Simulation

Shangping Guo
Old Dominion University

Follow this and additional works at: https://digitalcommons.odu.edu/ece_etds

 Part of the Electromagnetics and Photonics Commons

Recommended Citation
Guo, Shangping. "Photonic Crystals: Modeling and Simulation" (2003). Doctor of Philosophy (PhD), dissertation, Electrical/Computer Engineering, Old Dominion University, DOI: 10.25777/kpwa-jt36
https://digitalcommons.odu.edu/ece_etds/78

This Dissertation is brought to you for free and open access by the Electrical & Computer Engineering at ODU Digital Commons. It has been accepted for inclusion in Electrical & Computer Engineering Theses & Disssertations by an authorized administrator of ODU Digital Commons. For more information, please contact digitalcommons@odu.edu.

PHOTONIC CRYSTALS: MODELING AND SIMULATION

by

Shangping Guo
B.S.E.E July 1993, Tsinghua University
M.S.E.E. March 1996, Northern Jiaotong University

A Dissertation Submitted to the Faculty of
Old Dominion University in Partial Fulfillment of the
Requirements for the Degree of

DOCTOR OF PHILOSOPHY

ELECTRICAL ENGINEERING

OLD DOMINION UNIVERSITY

August 2003

Approved by:

Sacharia Albin (Director)

John B. Cooper (Member)

Karl H. Schoenbach (Member)

Linda L. Vahala (Member)

Reproduced with permission of the copyright owner. Further reproduction prohibited without permission.

ABSTRACT

PHOTONIC CRYSTAL: MODELING AND SIMULATION

Shangping Guo
Old Dominion University, 2003
Director: Dr. Sacharia Albin

Photonic crystals are periodic electromagnetic media in optical wavelength scale. They possess photonic band gaps (PBGs) that inhibit the existence of light within the crystals in certain wavelength range. Such band gaps produce many interesting optical phenomena. In this dissertation, the frequency (plane wave method, PWM) and time domain (finite difference time domain method, FDTD) methods are developed for their modeling and simulation.

The theory and algorithm of plane wave method are studied in detail and implemented in a unique and efficient approach. PWM is used to obtain the gap and mode information of ideal and defective photonic crystals. Several material and structural parameters are shown to affect the band gap. Examples of devices studied include high-Q micro-cavities, linear waveguides, highly efficient sharp bend, and channel drop filters.

Effects of defects in photonic crystals are studied in detail. Results show that point defects can form resonator centers of very high quality factors, whereas line defects can form linear waveguides in low/high index material. Highly efficient energy transfer occurs between defect modes. A numerical analysis of the interaction mechanisms between them is carried out and the results serve as a theoretical guide for device designs.

Photonic crystal fiber (PCF) with periodic air holes in the cladding is analyzed using a modified PWM method. PCF is able to guide light in single mode in a very broad wavelength region, or it can guide light in air core, offering superior optical properties. By tailoring the microstructures of the cladding, mode shape and group velocity dispersion can be controlled.

Finally, a simulation tool using FDTD is developed to study and simulate the device design. The Order-N method using FDTD and periodic boundary conditions is also presented to reduce the heavy computation of PWM method. Light dynamics in PBG devices are simulated and analyzed using FDTD and Perfectly Matched Layer boundary conditions. Excitation sources, mode symmetry, and detection techniques are described to obtain complete and accurate information from the simulations. The combination of the time domain and frequency domain methods provides a powerful tool for analysis and design of PBG devices with high performance.

Reproduced with permission of the copyright owner. Further reproduction prohibited without permission.

ACKNOWLEDGEMENTS

I would like to thank my advisor Dr. Sacharia Albin for giving me the confidence to complete this goal. His wisdom and his patience have been very important for this project. I would also like to thank Dr. Linda Vahala, Dr. Karl Schoenbach and Dr. John Cooper for serving as my dissertation committee members and taking time away from their busy schedules to help me bring this research to a conclusion.

A special mention goes to Dr. Arnel C Lavarias. His experience and knowledge in optics and his kind help were most valuable to my work and life at Old Dominion University. I would also like to thank my colleagues, Bing Xiao, Feng Wu, Ron Bentley and Dr. Weihai Fu, in Photonics and Nanoelectronics Labs. I have enjoyed working and talking with each of them, and I am thankful to have learned much from them.

I would also like to acknowledge the Dominion Scholar Graduate Research Fellowship and the Graduate Assistantship from the Electrical and Computer Engineering department, which were vital to the completion of this research. Also, I am thankful to the ODU LIONS computing resources for all the computations and graphics.

Finally, I would like to dedicate my work to my beloved father in heaven and my mother in China. I would also like to thank my brothers and sisters in China for all their love and support. Last but not least, I am most thankful and ever indebted to my wife, Ms. Xia Su for her sincere support and sacrifice, which make all my efforts worthwhile.

Reproduced with permission of the copyright owner. Further reproduction prohibited without permission.

TABLE OF CONTENTS

Page

LIST OF TABLES v

LIST OF FIGURES vi

Chapter

I. INTRODUCTION 1
- 1.1 An Overview 1
- 1.2 Photonic Band Gaps 4
- 1.3 Scope Of Research 4

II. PLANE WAVE METHOD 6
- 2.1 Numerical Methods For PBG Calculations 6
- 2.2 Theory Of Plane Wave Method 6
- 2.3 Implementation Of The Algorithm 10
- 2.4 Algorithm Convergence, Accuracy And Stability 16
- 2.5 Discussion 26

III. TWO-DIMENSIONAL PHOTONIC CRYSTALS 28
- 3.1 Band Gaps: The Parameter Interplay 28
- 3.2 Property Of Ideal PBG With a 2D Square Lattice 35
- 3.3 Defective PBG 42
- 3.4 Discussion 62

IV. PHOTONIC CRYSTAL FIBER 64
- 4.1 Analysis Method 64
- 4.2 Index-Guiding PCFs 66
- 4.3 Air Guiding PCFs 78
- 4.4 Discussion 82

V. FINITE DIFFERENCE TIME DOMAIN METHOD 84
- 5.1 Introduction 84
- 5.2 Simulation Of PBG Devices Using FDTD Method 84
- 5.3 The Order-N Method For Ideal PBG Structures 91
- 5.4 PBG Dynamics Analysis Using FDTD 96
- 5.5 Discussion 106

VI. SUMMARY AND FUTURE WORK 107

APPENDICES
- I. DERIVATION OF PLANE WAVE METHOD 109
- II. DERIVATION OF THE PCF ALGORITHM USING E 111
- III. DERIVATION OF THE PCF ALGORITHM USING H 113

REFERENCES 115

VITA 119

Reproduced with permission of the copyright owner. Further reproduction prohibited without permission.

LIST OF TABLES

Table Page

1. Dimensions of main matrices in the computation of plane wave method 14
2. Comparison of several methods: Accuracy, convergence, time used 22
3. Defect frequency of TM mode in a 2D square lattice using a 7X7 supercell 24
4. Defect frequency vs. supercell size of a 2D square lattice 24
5. Geometry of various 2D lattice, lattice constant a is defined as the distance between the two closest 'atoms' 31
6. Frequency split due to interaction between two point defects 54
7. Frequency shift of point defect mode due to the neighboring waveguides 62
8. Effective index of cladding at long wavelength region 67
9. Defect mode frequencies and their symmetries 97
10. Excited defect modes in the microcavity by plane waves with different incident angles 99

Reproduced with permission of the copyright owner. Further reproduction prohibited without permission.

LIST OF FIGURES

Figure Page

1. Example of 1D, 2D, 3D PBG structures 1
2. Conversion of a triangular lattice with circular cylinders 12
3. Selection and iteration process of plane waves 14
4. Band structure of a 3D diamond lattice 16
5. Convergence of TM mode vs number of plane waves 17
6. Convergence of TE mode vs number of plane waves 18
7. Eigen frequency convergence vs grid resolution for TM mode 19
8. Eigen frequency convergence vs grid resolution for TE mode 20
9. Convergence of eigen-frequency at M in band 1 for TE and TM with different average approach 21
10. Supercell approximation of defective crystals in a 2D triangular lattice 22
11. Band folding using supercell method 23
12. Convergence of defect frequency for TM mode using different supercell size in a square lattice with the center rod being removed 25
13. Mode field of defect modes in a 2D square lattice using a 5X5 supercell 26
14. 2D square lattice with circular cylinder 'atoms' 29
15. 2D triangular lattice with circular cylinder 'atoms' 29
16. 2D honeycomb lattice with circular cylinder 'atoms' 30
17. 2D Kagome lattice 30
18. Gap map of a 2D square lattice with alumina (Al_3O_2) rods in air 33
19. Gap map of inverted 2D square lattice with air holes in alumina (Al_3O_2) material 33
20. Basic 'atom' shape 34
21. Band gap vs dielectric constant contrast for a 2D triangular lattice 35
22. Band structure of 2D square lattice with alumina rods in air, R=0.2a 36
23. Eigen-frequency for TM modes 37
24. Density of states of TM modes in a square lattice with alumina rods in air, R=0.2a 38
25. Reflection and transmission of a 5X5 PBG along the direction of Γ-X using Transfer Matrix Method 39
26. Displacement field (D) for TM mode in a 2D square lattice with alumina rods in air 40
27. Band structure of a 2D square lattice with Alumina rods in air, a defect is formed by removing the center rod 43

Reproduced with permission of the copyright owner. Further reproduction prohibited without permission.

Figure Page

28. Defect bands in the gap (TM mode) by changing the size of a single 'atom' in a 2D square lattice with alumina rods in air 44
29. Defect mode frequency tuning by changing the dielectric constants of a single rod in a 2D square lattice of alumina rods.R=0.20a 45
30. Defect mode formed by 'acceptors' and donors 47
31. Two-fold dipole mode pattern formed by a donor defect with R=0.30a 47
32. 1st two-fold hexapole mode pattern formed by a donor defect with R=0.80a 48
33. 2nd two-fold hexapole mode pattern formed by a donor defect with R=0.80a 48
34. Waveguide formed by removal of a column of rods in a 2D square lattice 50
35. Mode field pattern of guided modes in an air waveguide 51
36. Microcavity with two point defects separated by only one rod 52
37. Interaction between two point defects 53
38. Waveguide formed by periodic point defects, period=2a 56
39. The band structure of a linear waveguide formed by periodic point defects, period=3a 56
40. Bandwidth tuning using periodic point defects 57
41. Monopole is sensitive to the waveguide width and becomes lossy while it deviates from the regular place 57
42. Waveguide by periodic increased size rods, period=3a, R=0.60a 58
43. Higher modes supported by a hybrid waveguide are quite stable 58
44. Schematic of a guiding mode-localized mode coupling 59
45. Different signs to the coupling of different directions due to the symmetry of the localized states 60
46. The frequency changes of point defect due to neighboring waveguides 61
47. 100% add/drop filter.backward coupling through a doubly degenerate point defect (R=0.70a) with hexapole modes 61
48. Finding the dielectric constants of the two sided rods to force degeneracy 62
49. PCF with air holes in a triangular lattice.A 5X5 supercell is used to simulate the fiber 66
50. Effective index of the periodic cladding and V in a triangular 2D PBG PCF with air holes 67
51. Endless single mode PCF.a=2.3μm, air hole radius R=0.3μm 68
52. Fundamental mode at λ=0.6328μm 69
53. Effective mode index of the fundamental mode and higher order modes 69
54. Group velocity dispersion of a triangular photonic crystal fiber 70

Reproduced with permission of the copyright owner. Further reproduction prohibited without permission.

Figure Page

55. The PCF with capillary tubes.Left.a 5X5 supercell used in our calculation 71
56. V and effective index of the cladding 72
57. Transverse E field intensity of the x-polarized fundamental mode 73
58. Transverse mode E-field intensity pattern of a capillary tube PCF with $R_a/a=0.15$, $\lambda=0.2a$ 74
59. Mode index of the first several modes (y-polarization only) 74
60. V-b curve of a capillary tube PCF 75
61. Dispersion property of the fundamental mode with different air hole sizes 76
62. Waveguide dispersion with different core radius, i.e.different drawing ratio, with the same air-filling fraction 77
63. Air guiding PCFs.Left.PCF with hexagonal rods 78
64. Band structure of a capillary PCF, $R_a=0.39a$, off-plane propagation constant=9.5 79
65. The variation of the first band gap of a capillary PCF vs the propagation constants along z-direction 80
66. Air guiding mode, x-polarization, crossing the band gap 81
67. Intensity pattern of the transverse E field 82
68. Position of the *E* and *H* about a cubic unit cell of the Yee space lattice 86
69. The flowchart of a general FDTD algorithm 88
70. The PML boundary condition for FDTD in a 2D TM problem 89
71. Periodic Boundary Condition for a 2D triangular unit cell 95
72. Band gap of a 2D triangular lattice using FDTD method 96
73. The setup for calculation of the defect modes in a microcavity 98
74. The spectrum of amplitude obtained from the three detectors inside the crystal 99
75. Far field pattern of the four defect modes in the cavity 100
76. The mode evolution of each resonant modes 101
77. The PBG waveguide 102
78. A sharp PBG bending 103
79. Multiple channel drop for WDM applications 105
80. The spectrum of the three drop channels 105

Reproduced with permission of the copyright owner. Further reproduction prohibited without permission.

CHAPTER I

INTRODUCTION

1.1 AN OVERVIEW

In the last decade, photonic band gap (PBG) materials or photonic crystals have been a rapidly developing field in micro-optics and quantum physics. Photonic band gap materials are artificially arranged periodic electromagnetic media in 1D, 2D or 3D (Figure 1) with the periodicity in the operating wavelength scale (~μm). It is an analogous to semiconductors with periodic structures in atomic scale (~nm). In semiconductors, the periodic potential for electrons in semiconductor leads to the formation of electronic band gap. In PBG materials, the periodic refractive index for photons leads to the formation of photonic band gap. No electrons are allowed in the electronic band gap, likewise no photons are allowed to propagate in the photonic band gap. Unlike the natural periodic semiconductors, PBG structures can be of unlimited forms, which provide possibilities of creating many different novel photonic devices. The study of photonic crystal is governed by Bloch theorem and Maxwell's equations, and is inherently accurate. Hence, photons in PBG materials are controllable and their properties are highly predictable, which makes coherent photonic devices feasible. On the contrary, electrons in semiconductor are often diffracted by unwanted defects and the property is governed by Shrodinger equation, which is based on quantum physics. In photonic crystals, intentionally introduced defects lead to localized electromagnetic states or localized propagating states; examples are high Q micro-cavities and linear waveguides in any media. These structures can guide light without radiation loss around sharp bend or in lower-index material, leading to a versatile way to control light.

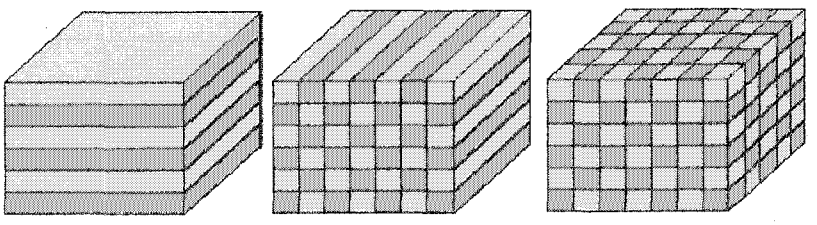

Figure 1. Example of 1D, 2D, 3D PBG structures: 1D multilayer structure, 2D square slab structure, 3D cube structure.

The Format followed: Physical Review B.

Reproduced with permission of the copyright owner. Further reproduction prohibited without permission.

The study of electromagnetic waves in 1D periodic materials (multi-layer media) has a long history. In 1887, Lord Rayleigh first studied the multi-layer media. He identified the existence of a narrow band gap which light cannot propagate through. The gap is dependent on the incident angle due to the different periodicity in different angles, leading to colors varying with angles. Pochi Yeh et al [1] found possible light localization in defects in these 1D periodic structures. The possible existence of photonic band gaps in 2D and 3D periodic structures was found in 1987 by two research groups, marking the beginning of PBG devices. Yablonovitch [2, 3] predicted that a 3D periodic structure had an electromagnetic band gap that overlapped the electronic band edge, and all radiation, including the spontaneous emissions were strictly inhibited. Sajeev John [4] first pointed out the existence of Anderson localization of light in moderately disordered structures. Since then, photonic crystals have been a hot area, leading to many subsequent developments in fabrication, theory and applications. There are books [5], conference proceedings [6], special journal editions [7-9] and hundreds of research published papers each year on photonic crystals.

However, the search for a band gap in 3D structures proved unsuccessful both experimentally and theoretically for several years. A breakthrough came when the vector nature of the photons was recognized to play an important role in forming the band gap. As a result, several papers published in 1990 [10, 11] predicted the band gaps correctly using the vectorial plane wave method. Soon the 3D diamond structure was found to have a complete band gap [10, 12].

In subsequent years, many different geometries in 1D, 2D and 3D had been explored both theoretically and experimentally. A brief review of the research follows that is roughly divided into four categories: calculation, fabrication, device application and quantum effects. Photonic band gap is a complicated interaction of multi-scattering and Mie scattering. Numerical computations are crucial for most theoretical analyses. The numerical methods typically fall into three categories: the time domain method such as the Finite Difference Time Domain method (FDTD), which can model the time-evolution of electromagnetic fields in these structures; the transfer matrix method, where scattering matrices are computed to obtain the transmission and reflection through the structure; and frequency domain method, mainly, the plane wave method (PWM) which is proved very successful in searching band gap in different geometries. However, PWM has some inherent weaknesses, such as its heavy computation and inability to deal with materials with dispersion or loss. Time domain methods and transfer matrix method can provide some measurable information such as reflection and transmission, but information obtained

Reproduced with permission of the copyright owner. Further reproduction prohibited without permission.

depends on many conditions of the numerical experiments, and may not be complete or accurate enough.

Following the development of theory, new designs and devices are proposed theoretically and fabricated experimentally. Due to the fabrication difficulty of 3D PBG structures, most novel devices are based on 2D PBG structures. Some of the important new devices or designs are listed below:

- The low loss sharp bend [13-17] which allows high efficiency transmission through a very sharp bend
- High Q microcavity [18-20], which is generally produced by a point defect in a bulk crystal, the quality factor Q can be up to tens of thousands
- PBG planar antenna [21-25], which can improve radiation efficiency or patterns, and could be useful for reducing radiations of cell phones
- Microcavity defect laser [19, 26-30], which can suppress spontaneous emission effectively, leading to a very low threshold lasing
- High extraction efficiency LED [31, 32], by overcoming the TIR in conventional LEDs, the PBG based LED can extract most light generated in the LED region
- 100% channel add/drop filter[33-35]
- Linear waveguiding [36-41]
- Low cross-talk channel cross [42] and so on.

Photonic crystal fiber (PCF), which is also called holey fiber, seems to develop into its own technology segment. Its fabrication is much easier than those conventional optical fibers since it needs no doping in the core. The index-guiding PCF can be single-mode in all wavelength regions [43]; the PBG effect in PCF can even guide light in a large air hole [44].

Quantum effects in photonic crystals are of interest to many researchers. The main interests include the control of spontaneous emission [3, 26, 45, 46], atom-photon or matter-photon interaction in PBG environment [46-48], nonlinear effects in fiber or planar devices [49, 50], surface plasmons in metallodielectric PBG structures [51, 52].

Fabrication of PBG devices is vital to its development. Though several methods were suggested in literature, few of them are good for mass production. Among them, silicon micro-machining [15, 38, 53], oval self-organizing [54], and macro-porous silicon [55] for 2D slab structure are the more promising methods.

Reproduced with permission of the copyright owner. Further reproduction prohibited without permission.

1.2 Photonic Band Gaps

In PBG materials, the formation of photonic band gap is a result of synergetic interplay between the macroscopic Bragg scattering and the microscopic Mie scattering. Bragg scattering relates to the periodicity, or the geometry of the lattice; Mie scattering relates to the shape of individual scatterers [56]. The refractive index contrast affects mainly the strength of these two scattering mechanisms that are quite complex. Hence, there is no simple relation between the band gap and the PBG structures. Numerical calculation is crucial for predicting the properties of light in these structures.

No electromagnetic waves or optical modes are allowed in the band gap, and PBG is essentially an electromagnetic 'vacuum'. This is used to suppress spontaneous emission in the PBG, and make low threshold lasers and LED devices. Also, it brings some new quantum effects such as extremely low group velocity at the edge of the gap.

When disorder is introduced in the PBG structures, a defect forms. Discrete energy levels may generate in the band gap. This is called defect bands or localized states since these modes are not allowed to propagate through the surrounding PBG structures. The localization of light in PBG is of most interest since this is a totally new way to control the flow of light.

1.3 Scope Of Research

This work mainly focuses on how to model and simulate PBG devices, to explore their properties, and effects of some design parameters. It is a first and important step in the research on PBG material. The objective is to provide theoretical analysis and numerical tools to design and simulate PBG structures and devices, and find possible applications. The dissertation is organized in the following sections. In Chapter II, the plane wave method (PWM) is implemented in MATLAB and the convergence and accuracy are discussed, which determine the accuracy of most calculations in subsequent sections. In Chapter III, the PWM is used to analyze some planar PBG devices. The effect of structural parameters on the band gap is studied first, and then two basic defects, point defects and line defects are studied. Interactions between defects are described in a qualitative way based on the numerical results. In Chapter IV, an important device, the photonic crystal fiber, is treated using a full-vectorial modified PWM, and two types of microstructure fibers including the index-guiding fibers and photonic band gap guiding fibers are studied. In Chapter V, the time domain method FDTD including the order-N method for reducing computations is described and implemented for PBG and other general electromagnetic field applications. Two boundary conditions, the periodic boundary condition (PBC) and Perfectly Matched Layers (PML) boundary condition are discussed. The dynamics in several important

Reproduced with permission of the copyright owner. Further reproduction prohibited without permission.

PBG devices including the high Q microcavity as filters, linear waveguides, and their interactions are studied using the FDTD simulation. A summary and conclusion of the research is given in Chapter VI.

Reproduced with permission of the copyright owner. Further reproduction prohibited without permission.

CHAPTER II

PLANE WAVE METHOD

2.1 Numerical Methods For PBG Calculations

Many approaches have been proposed for the research of photonic band gap materials, for example, the transfer matrix method [57, 58], scattering matrix method [59], plane wave expansion method [11, 60, 61], Finite difference time domain (FDTD) method [62], method of momentum, finite element method [63, 64], etc. Among them, plane wave expansion method and FDTD method are the most popular numerical methods for PBG structures.

Transfer matrix method and scattering matrix method can be used to obtain the transmission spectrum for finite photonic crystals by calculating the respective matrices for each layer; plane wave expansion method is a frequency domain method, and it can obtain the band structure and mode fields. FDTD is a time domain method, which can be used to study the dynamics of PBG devices. It was first introduced in PBG research just a few years ago and has been showing great promise to treat some complicated PBG structures, especially the dynamics of real PBG devices, which plane wave method is incapable of dealing with.

Plane wave expansion method for PBG structure was first implemented in 1990, and was a breakthrough to the PBG research at that time. It is a full-vector method to treat macroscopic electromagnetic problems by applying periodic boundary. This concept may apply to many non-periodic problems using supercell concept if the effect at the boundary can be considered small enough. Vector treatment is very important for obtaining correct results since the PBG effect is led by the multiple scattering waves by the periodic scatterers.

2.2 Theory Of Plane Wave Method

2.2.1 Maxwell equations for certain conditions

First, we consider Maxwell equations in these conditions:

- A source-free space: $\rho = 0, J = 0$;
- Lossless medium: $\varepsilon(r)$ is real and no material dispersion in the region of interest;
- Linear and time-invariant: any mode can be decomposed of a set of plane waves using Fourier theory
- $\mu(r) = const.$

Reproduced with permission of the copyright owner. Further reproduction prohibited without permission.

Using complex forms $\begin{pmatrix} E(r) \\ H(r) \end{pmatrix} \exp\left[i\left(\omega t - \vec{k}\cdot\vec{r}\right)\right]$, the time derivatives in Maxwell equations can be eliminated using $\partial/\partial t \rightarrow j\omega$:

$$\begin{cases} \nabla \bullet \varepsilon(r)\vec{E}(r) = 0 \\ \nabla \bullet \vec{H}(r) = 0 \\ \nabla \times \vec{H}(r) = j\omega\varepsilon_0\varepsilon(r)\vec{E}(r) \\ \nabla \times \vec{E}(r) = -j\omega\mu_0\vec{H}(r) \end{cases} \tag{2.1}$$

From the equation above, one can conclude that H and D (i.e. $\varepsilon(r)E$) are transverse and continuous everywhere, but E is not necessarily so.

Putting the 3rd equation in (2.1) into the 4th equation, the vector wave equation for H can be easily obtained:

$$\nabla \times \frac{1}{\varepsilon(r)} \nabla \times \vec{H}(r) = \frac{\omega^2}{c^2}\vec{H}(r) \tag{2.2}$$

with the transverse condition being: $\nabla \bullet \vec{H}(r) = 0$. (2.3)

This is a standard eigen-value problem, $\Theta\vec{H} = \Lambda\vec{H}$. The operator $\Theta = \nabla \times \frac{1}{\varepsilon} \nabla \times$ has some important properties [5]:

1. It is a linear operator: if H_1 and H_2 are two different modes of the system, then the combination H_1+H_2 is also a mode supported by the system.
2. It is a Hermitian operator: by definition, the inner product $(f, \Theta g) = (\Theta f, g)$. This leads to two important properties as below:
   - It has only real eigen values, based on the fact that it is a Hermitian operator and $\varepsilon(r)$ is real everywhere.
   - Orthogonality: any two different modes are orthogonal to each other. $(H_i, H_j) = \delta_{ij}$ assuming the fields are normalized.
3. Scaling. $\varepsilon(r) \leftrightarrow \omega$: if the same dielectric function scales by a factor a, $\varepsilon'(r) = \varepsilon(r/a)$, the eigen frequency will also be scaled by a, $\omega' = \omega/a$. This is why the principle of PBG can be applied to different frequency region, optical or microwave region.

Once H is solved, E can be obtained by using the following equation:

$$\vec{E}(r) = \frac{1}{j\omega\varepsilon(r)} \nabla \times \vec{H}(r) \tag{2.4}$$

Reproduced with permission of the copyright owner. Further reproduction prohibited without permission.

We use the equation for H instead of D or E since the operators for D and E are not Hermitian and do not possess these properties.

2.2.2 Bloch theorem for periodic structure

For infinite periodic structures, Bloch theorem is often used. Bloch theorem shows that a plane wave in an infinite periodic structure will be modulated by the periodicity. So, the magnetic field H can be expressed as:

$$\begin{aligned} \vec{H}(r) &= e^{i\vec{k}\bullet\vec{r}}u(r)\hat{e}_k \\ u(r) &= u(r+R_l) \end{aligned} \tag{2.5}$$

where R_l is an arbitrary lattice vector, $\hat{e}_k$ is a unit vector perpendicular to the vector $\vec{k}$ and parallel to the H vector to reflect the transversal property of H.

The dielectric function ε(r) is periodic in r-space:

$$\varepsilon(r) = \varepsilon(r+R_l) \tag{2.6}$$

where:

$$R_l = l_1\vec{a}_1 + l_2\vec{a}_2 + l_3\vec{a}_3 \tag{2.7}$$

R_l is an arbitrary lattice vector, l_1, l_2, l_3 are integers, and $\vec{a}_1, \vec{a}_2, \vec{a}_3$ are the basis lattice vectors to describe the periodic lattice.

Using Fourier transform for periodic functions:

$$\varepsilon(r) = \sum_{\vec{G}_i} \varepsilon(\vec{G}_i) e^{i\vec{G}_i\cdot\vec{r}} \ , \ \varepsilon(\vec{G}) = \frac{1}{V}\iiint_{\Omega} \varepsilon(r) e^{-i\vec{G}\cdot\vec{r}}\, d\Omega \tag{2.8}$$

Since u(r) has the same periodic property as ε(r), H can be expanded as:

$$\vec{H}(r) = \sum_{\vec{G}_i,\lambda} h(\vec{G}_i,\lambda)\hat{e}_\lambda e^{i(\vec{k}+\vec{G}_i)\vec{r}} \tag{2.9}$$

Here G_i is an arbitrary spatial frequency which we call it as reciprocal lattice vector, and

$$\vec{G}_i = h_1\vec{b}_1 + h_2\vec{b}_2 + h_3\vec{b}_3 \tag{2.10}$$

where b_1, b_2, b_3 are basis vectors in the reciprocal space; h_1, h_2, h_3 are integers; λ represents 1 and 2; $\hat{e}_\lambda$ represents the two orthogonal unit vectors, which are both perpendicular to $\vec{k}+\vec{G}_i$, i.e.:

$$\begin{aligned} (\vec{k}+\vec{G}_i)\bullet\hat{e}_\lambda &= 0 \\ \hat{e}_1\bullet\hat{e}_2 &= 0 \end{aligned} \tag{2.11}$$

All the lattice vectors R_l form the lattice in the r-space, and all the reciprocal lattice vectors G_i form the reciprocal lattice in the reciprocal space, according to the terms in solid-state physics. The two sets of basis vectors are orthogonal to each other, and they are related by:

Reproduced with permission of the copyright owner. Further reproduction prohibited without permission.

$$\vec{b}_i \bullet \vec{a}_j = 2\pi\delta_{ij} \tag{2.12}$$

$$\vec{b}_1 = 2\pi\frac{\vec{a}_2\times\vec{a}_3}{\vec{a}_1\bullet\vec{a}_2\times\vec{a}_3}, \hat{b}_2 = 2\pi\frac{\vec{a}_3\times\vec{a}_1}{\vec{a}_1\bullet\vec{a}_2\times\vec{a}_3}, \hat{b}_3 = 2\pi\frac{\vec{a}_1\times\vec{a}_2}{\vec{a}_1\bullet\vec{a}_2\times\vec{a}_3} \tag{2.13}$$

Using equations (2.8) and (2.9), and applying the transverse condition, the wave equation can be transformed to an algebraic form [11] (See Appendix I):

$$\sum_{G'}\left|\vec{k}+\vec{G}\right\|\vec{k}+\vec{G}'\left|\varepsilon^{-1}\left(\vec{G}-\vec{G}'\right)\right.\begin{bmatrix}\hat{e}_2\bullet\hat{e}_2' & -\hat{e}_2\bullet\hat{e}_1'\\ -\hat{e}_1\bullet\hat{e}_2' & \hat{e}_1\bullet\hat{e}_1'\end{bmatrix}\begin{bmatrix}h_1'\\ h_2'\end{bmatrix}=\frac{\omega^2}{c^2}\begin{bmatrix}h_1\\ h_2\end{bmatrix}. \tag{2.14}$$

This is a standard eigen-value problem and it can be written as the matrix form:

$$\begin{bmatrix}M_1 & M_2\\ M_3 & M_4\end{bmatrix}\begin{bmatrix}h_1(G')\\ h_2(G')\end{bmatrix}=\frac{\omega^2}{c^2}\begin{bmatrix}h_1(G)\\ h_2(G)\end{bmatrix} \tag{2.15}$$

If N plane waves (G vectors) are used, this will be a $2N$ linear equation group, and the complexity of this problem is $O(8N^3)$ when a standard eigen-solver is used.

Simplifications exist for 2D and 1D PBG's. For 2D photonic crystal, we assume the dielectric constants along z-direction are invariant. For in-plane propagation, k_z=0, wave vector k is always in the xy-plane. In this case, e_2=e_z, e_1 is always in the xy-plane, so $[M_2]$ and $[M_3]$ are zero matrices, and two polarizations h_1 and h_2 become decoupled. Since h_1 is in the xy plane and h_2 is along z-direction, h_1 is TM mode, and h_2 is TE mode(From equation (2.4), E has components only in xy-plane). Equation (2.14) is decomposed into TE and TM modes:

TM:
$$\sum_{G'}\left|\vec{k}+\vec{G}\right\|\vec{k}+\vec{G}'\left|\varepsilon^{-1}\left(\vec{G}-\vec{G}'\right)h_1\left(\vec{G}'\right)=\frac{\omega^2}{c^2}h_1\left(\vec{G}\right)\right. \tag{2.16}$$

TE:
$$\sum_{G'}\left(\vec{k}+\vec{G}\right)\bullet\left(\vec{k}+\vec{G}'\right)\varepsilon^{-1}\left(\vec{G}-\vec{G}'\right)h_2\left(\vec{G}'\right)=\frac{\omega^2}{c^2}h_2\left(\vec{G}\right). \tag{2.17}$$

Each of them is a group of N linear equations if N plane waves are used, so the dimension of the eigen-matrix is reduced by half and the complexity reduces to $O(N^3)$. For 1D normal incidence, TE and TM behave similar and only one equation is needed. Off-plane 1D and 2D problems can be treated as 2D and 3D problems, respectively.

For each specific wave vector k, the eigen-value gives the frequencies ω of the eigen-modes. Using N plane waves, we will get $2N$ (for TE & TM is N) discrete frequencies for each k-point. These frequencies are sorted in ascending order and labeled as 1 to $2N$. One band is formed by all the eigen-frequencies with the same order for all k-vectors in First Irreducible Brillouin zone (IBZ).

Reproduced with permission of the copyright owner. Further reproduction prohibited without permission.

According to Bloch theorem, we can restrict the wave vector k in the 1st Brillouin zone for the periodicity in the reciprocal space. In addition, taking advantage of the symmetry of the 1st Brillouin zone, we can calculate only the eigen-frequencies for those k-vectors along the edge of the IBZ, since those frequencies for the k-vectors falling inside the IBZ will fall inside the band.

The eigenvectors can be used to form $\vec{H}$ and $\vec{D}$ fields according to equation (2.4) and (2.9).

The concepts of band structure and band gap are taken from solid-state electronics. Also, we use other concepts in solid-state physics, such as: lattice vector, reciprocal lattice vector, primitive unit cell, Wegner-Seitz unit cell, 1st Brillouin zone, and irreducible 1st Brillouin zone.

2.3 Implementation Of The Algorithm

Several important points will be discussed below regarding the implementation of the algorithm. The general procedure is to define the structure of study, find the Fourier transform, obtain the matrix $\varepsilon\left(\vec{G}-\vec{G}'\right)$, and form the eigen-value problem. Our implementation uses MATLAB and can solve most PBG problems with different geometry, different 'atom' shape. Since PBG is often composed of localized medium in periodic grid points in a background of another different medium, we call the localized medium as an 'atom'.

Since the eigen-value problem is a standard problem, the difficulty lies in finding the Fourier transforms of different structures. We differentiate different structures by 'atom' shape, lattice geometry and dimensionality. To extend the ability to treat more complex structures, the concept of supercell is introduced. The supercell may contain a finite number of 'atoms' with the same or different shape, in periodic or non-periodic arrangement. The periodic boundary condition applies at the boundary of the supercell. The geometry represents the arrangement of the supercell. For simple cases, the supercell contains only one 'atom'.

2.3.1 Shift property of Fourier transform

Assuming the Fourier transform of a single atom ε(r) is known as ε(G), if ε(r) is shifted by an amount r_0, then its Fourier transform must be multiplied by $e^{i\vec{G}\bullet\vec{r}_0}$ according to [65] which we call it as the shift property:

$$\varepsilon\left(r+r_0\right)\leftrightarrow e^{i\vec{G}\bullet\vec{r}_0}\varepsilon\left(G\right). \tag{2.18}$$

Therefore, for a supercell with several atoms in periodic or random positions, the Fourier transform can be obtained using addition and subtraction:

$$\sum_{r_i}\varepsilon\left(r+r_i\right)\Leftrightarrow\sum_{r_i}e^{i\vec{G}\bullet r_i}\varepsilon\left(G\right) \tag{2.19}$$

where r_i is the location of an 'atom' in the supercell.

Reproduced with permission of the copyright owner. Further reproduction prohibited without permission.

Shift property is especially suitable for supercell method for cases such as the photonic crystal with defects. We can obtain accurate Fourier coefficients of the supercell at the required G grid points by doing simple additions and subtractions, requiring only the Fourier coefficients of each single kind of atom. This is especially advantageous for a large supercell with many periodic or random atoms in it.

2.3.2 'Atoms' with regular shape

Using analytical Fourier transform when available will be advantageous. We illustrate the implementation in the case of 2D photonic crystals with the most commonly used circular cylinder. Other shapes such as the sphere, cubes, and rectangular blocks can follow the same procedure and their Fourier transforms can be found in Ref. [65].

Assuming the radius of the cylinder is R, the dielectric constant for the cylinder ('atom') is ε_a, the background dielectric constant is ε_b, the lattice structure can be represented by the two lattice basis vector $\vec{a}_1$ and $\vec{a}_2$. The cell area is calculated as $A = |\vec{a}_1 \times \vec{a}_2|$, the Fourier transform of the unit cell is:

$$\varepsilon(G) = \varepsilon_b \delta(G) + (\varepsilon_a - \varepsilon_b)\frac{2\pi R^2}{A}\frac{J_1(GR)}{GR} = \varepsilon_b \delta(G) + 2(\varepsilon_a - \varepsilon_b) f \frac{J_1(GR)}{GR} \tag{2.20}$$

$$\varepsilon(G=0) = \varepsilon_b + f(\varepsilon_a - \varepsilon_b) \tag{2.21}$$

where J_1 is the 1st order Bessel function, f is a fraction parameter and

where J_1 is the 1st order Bessel function, f is a fraction parameter and

$$f = Vol_{atom}/Vol_{cell}. \tag{2.22}$$

When the analytical form of the Fourier transform of a structure is known, the 'atom' shape and lattice geometry are already taken into account. Hence, we need not worry about the different geometry of the lattice.

2.3.3 'Atoms' with arbitrary shape

When the atom shape is not regular, no easy Fourier transform can be obtained, only numerical FFT can be used. However, FFT can only deal with orthogonal space, square or cube, it is difficult to apply FFT directly on non-orthogonal unit cell. We found non-orthogonal unit cell can be converted to orthogonal cell using coordinate conversion, so FFT can be easily applied. Once the FFT is done, the other procedures are the same as above.

Assuming the three basis lattice vectors in the Cartesian real space are $\vec{a}_1, \vec{a}_2, \vec{a}_3$ with:

Reproduced with permission of the copyright owner. Further reproduction prohibited without permission.

$$\begin{aligned}\vec{a}_1 &= a_{1x}\hat{x} + a_{1y}\hat{y} + a_{1z}\hat{z} \\ \vec{a}_2 &= a_{2x}\hat{x} + a_{2y}\hat{y} + a_{2z}\hat{z}, \\ \vec{a}_3 &= a_{3x}\hat{x} + a_{3y}\hat{y} + a_{3z}\hat{z}\end{aligned} \tag{2.23}$$

and the dielectric function in the unit cell is $\varepsilon(r)$. Column vector is $\vec{r} = m\vec{a}_1 + n\vec{a}_2 + l\vec{a}_3$, where m, n and l are coordinates along the basis lattice vectors. In Cartesian coordinates:

$$\vec{r} = (ma_{1x} + na_{2x} + la_{3x})\hat{x} + (ma_{1y} + na_{2y} + la_{3y})\hat{y} + (ma_{1z} + na_{2z} + la_{3z})\hat{z} \tag{2.24}$$

So we can easily have:

$$|r^2| = \vec{r}^T[g]\vec{r} \tag{2.25}$$

where

$$[g] = \begin{bmatrix} a_{1x} & a_{1y} & a_{1z} \\ a_{2x} & a_{2y} & a_{2z} \\ a_{3x} & a_{3y} & a_{3z} \end{bmatrix} \begin{bmatrix} a_{1x} & a_{2x} & a_{3x} \\ a_{1y} & a_{2y} & a_{3y} \\ a_{1z} & a_{2z} & a_{3z} \end{bmatrix} \tag{2.26}$$

is called the metric for the oblique coordinates [66, 67].

The dielectric function can be converted to an equivalent function in a square or cube unit cell. Taking the 2D triangular lattice as an example, see Figure 2, the unit cell is oblique, and the atom in the unit cell is a cylinder. After the conversion, the unit cell is square and the atom is changed into an oblique ellipse cylinder. FFT is then applied on this equivalent unit cell.

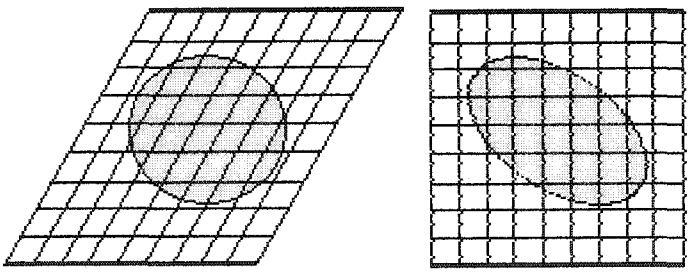

Figure 2. Coodrinate conversion of a triangular lattice with circular cylinders. Note when the radius of the cylinder is larger, part of the cylinder will go out of the unit cell, and neighboring atoms will come into the unit cell.

2.3.4 Implementation procedure

Our procedure for the band structure calculation is given as below:

1. Define the basis lattice vectors $\vec{a}_1, \vec{a}_2, \vec{a}_3$ in Cartesian coordination, dielectric constants for background material ε_b, dielectric constants for the 'atom' ε_a, shape parameter (e.g., radius R) and periodicity a, supercell size (number of periods along each dimension, can be a real

Reproduced with permission of the copyright owner. Further reproduction prohibited without permission.

number); Calculate the reciprocal lattice vectors $\vec{b}_1, \vec{b}_2, \vec{b}_3$, metric tensor [g], fraction parameter *f*. Also the 'atom' number and position in the primitive unit cell, and those high-symmetric points in the irreducible first Brillouin zone (IBZ) should be found.

2. Form the Fourier transform matrix ε(G) according to its analytical form if available. This matrix is calculated only once and should contain all the Fourier coefficients required for ε(G-G') in the iteration. Its dimension is usually small and the computation is small, for example, in a 2D PBG, a 100x100 ε(G) can be enough for 2500 plane waves.
3. If there is no analytical Fourier transform, coordination conversion is used to form the dielectric matrix while dividing the unit cell in real space into a fine mesh and then perform FFT. A submesh is used to average dielectric constants at each grid point. The size of the FFT matrix is usually much larger than the one in step (2) in order to improve accuracy.
4. Use the shift property in equation (2.18-2.19) to get the Fourier transform for the supercell.
5. Specify the grid points in the reciprocal space to be used, in other words, the plane waves to be used. The set of plane waves can be selected somewhat arbitrarily, as shown in Figure 3, however, it will affect the convergence. For example, using the right scheme in Figure 3 for 2D triangular lattice can save about 10% plane waves than using the left scheme. If the left scheme is used: along direction of each reciprocal lattice base vector, choose the n closest grid points. So the total grid points or plane waves used would be $N_{PW}=(2n+1)$, $N_{PW}=(2n+1)^2$, and $N_{PW}=(2n+1)^3$ for 1D, 2D, and 3D PBG's respectively.
6. Select all the coefficients in matrix ε(G) needed to form the matrix ε(G-G'). The dimension of this matrix should be N_{PW} x N_{PW}.
7. Calculate the inverse matrix of ε(G-G').
8. Form the *k*-vector array to be used, interpolating between those high-symmetric points in IBZ.
9. Form the eigen-matrix [M] according to the problem to be solved and the dimension of [M] will be N_{PW} x N_{PW} or $2N_{PW}$ x $2N_{PW}$, depending on the equation (2.15) (2.16) and (2.17).
10. Find all the eigenvalues and/or the eigenvectors of interest. A new iteration goes to (5), see Figure 3.
11. Output the final results by graph or file.

Reproduced with permission of the copyright owner. Further reproduction prohibited without permission.

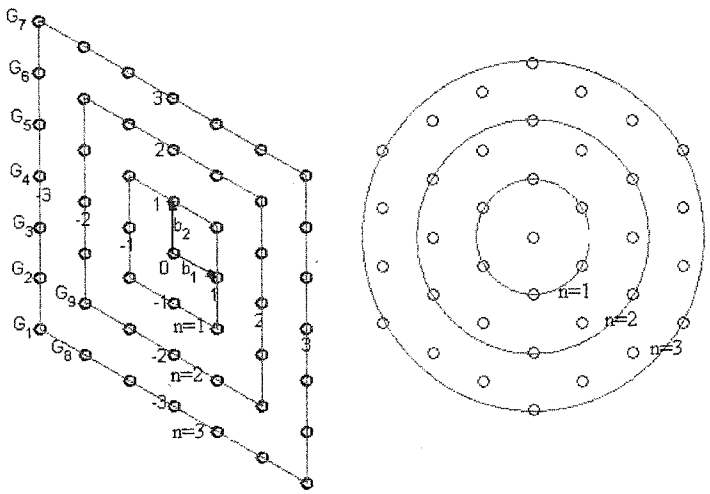

Figure 3. Selection and iteration process of plane waves in a 2D triangular lattice. Left: Grid points are selected and iterated along the basis vectors. Right: Grid points are selected and iterated according to distance of grid to origin.

Table 1. Dimensions of main matrices in the computation of plane wave method, assuming grid number along each direction is n, and maximum allowed grid number is n_{max}.

	1D	2D TE/TM	**3D**
N_{PW}	$(2n+1)$	$(2n+1)^2$	$(2n+1)^3$
ε(G) Analytical	$(4n_{max}+1)x1$	$(4n_{max}+1)x(4n_{max}+1)$	$(4n_{max}+1)x(4n_{max}+1)x(4n_{max}+1)$
ε(G) FFT	$>>(4n_{max}+1)$	$>>(4n_{max}+1)x(4n_{max}+1)$	$>>(4n_{max}+1)x(4n_{max}+1)x(4n_{max}+1)$
ε(G-G')	$N_{PW}xN_{PW}$	$N_{PW}xN_{PW}$	$N_{PW}xN_{PW}$
[M]	$N_{PW}xN_{PW}$	$N_{PW}xN_{PW}$	$2N_{PW}x2N_{PW}$

The main quantities and dimensions of the main matrices are listed in Table 1. The computation lies mainly in the eigen-value calculations. The complexity of eignvalue calculation is $O(N^3)$, where N is the dimension of the eigen matrix. This is very time consuming and needs a large amount of memory when the matrix size is over 1000, so a stable and fast eigen-solver will be able to greatly improve the performance when the problem size is large. Subspace and Lanzcos algorithms may be good for these calculations and this is left to future work. Our implementation uses the standard function *eig*, which MATLAB provides, it solves all the eigenvalues and/or eigenvectors and the time is acceptable for matrix smaller than 2000x2000 (This may take ~15 minutes for one solution on a 400MHz Sun processor).

Reproduced with permission of the copyright owner. Further reproduction prohibited without permission.

We provide source files for calculating 1D, 2D, 3D PBG with different 'atom' shapes, lattice geometries, and they are freely downloadable from our website www.ece.odu.edu/~sguox002. These codes are vectorized so that they are simple and efficient, since MATLAB is designed to work best with matrices. These programs are so tiny, more or less than 100 lines, that they are very good for understanding and further development.

As an example, we show below how the 3D diamond lattice is worked out:

The diamond lattice is a complex FCC lattice with two spherical atoms in the unit cell. Assuming the length of the simple cubic side is a, the primitive basis lattice vectors are defined as $\vec{a}_1 = [0,1,1]a/2, \vec{a}_2 = [1,0,1]a/2, \vec{a}_3 = [1,1,0]a/2$. The locations of the two atoms in the primitive cell are: $\vec{r}_0 = [-1,-1,-1]a/8$ and $\vec{r}_1 = [1,1,1]a/8$. The reciprocal basis vectors are calculated according to (2.11): $\vec{b}_1 = \frac{2\pi}{a}[-1,1,1], \vec{b}_2 = \frac{2\pi}{a}[1,-1,1], \vec{b}_3 = \frac{2\pi}{a}[1,1,-1]$. Assuming the radius of the sphere is R, the Fourier transform for a single sphere 'atom' at the reciprocal lattice grid is expressed as:

$$\varepsilon(\vec{G}) = 3f(\varepsilon_a - \varepsilon_b)\left(\frac{\sin GR - GR\cos GR}{(GR)^3}\right) \tag{2.27}$$

The Fourier transform of the supercell with 2 'atoms' can be obtained using (2.19):

$$\varepsilon(\vec{G}) = 3f(\varepsilon_a - \varepsilon_b)\left(\frac{\sin GR - GR\cos GR}{(GR)^3}\right)\cos(\vec{G}\bullet\vec{r}_0) \tag{2.28}$$

using shift property and Fourier transform for a sphere, where $f = 2\frac{4\pi R^3/3}{V}$ and $V = |\vec{a}_1 \bullet \vec{a}_2 \times \vec{a}_3|$. The DC component needs to be taken care of separately.

The matrix $\varepsilon(G\text{-}G')$ is obtained by picking the items from the matrix $\varepsilon(G)$. The relation is set by: $G = (m,n,l)$, $G' = (m',n',l')$ and $G - G' = (m-m', n-n', l-l')$, m, n and l are integers, they are coordinates along the reciprocal basis vectors. Since G and G' are arbitrary grid vectors in the selection, the range of $G\text{-}G'$ will double in each direction. This ensures that if the matrix $\varepsilon(G)$ is two-times as large as the G selection, all the required Fourier coefficients in $\varepsilon(G\text{-}G')$ are already calculated in $\varepsilon(G)$.

We show the band structure for $R = \sqrt{3}/8\,a$ in Figure 4 using our simple program with $(2\times 3+1)^3 = 343$ plane waves. The graph shows excellent agreement with the result in Ref. [10] even though we used a very small number of plane waves.

Reproduced with permission of the copyright owner. Further reproduction prohibited without permission.

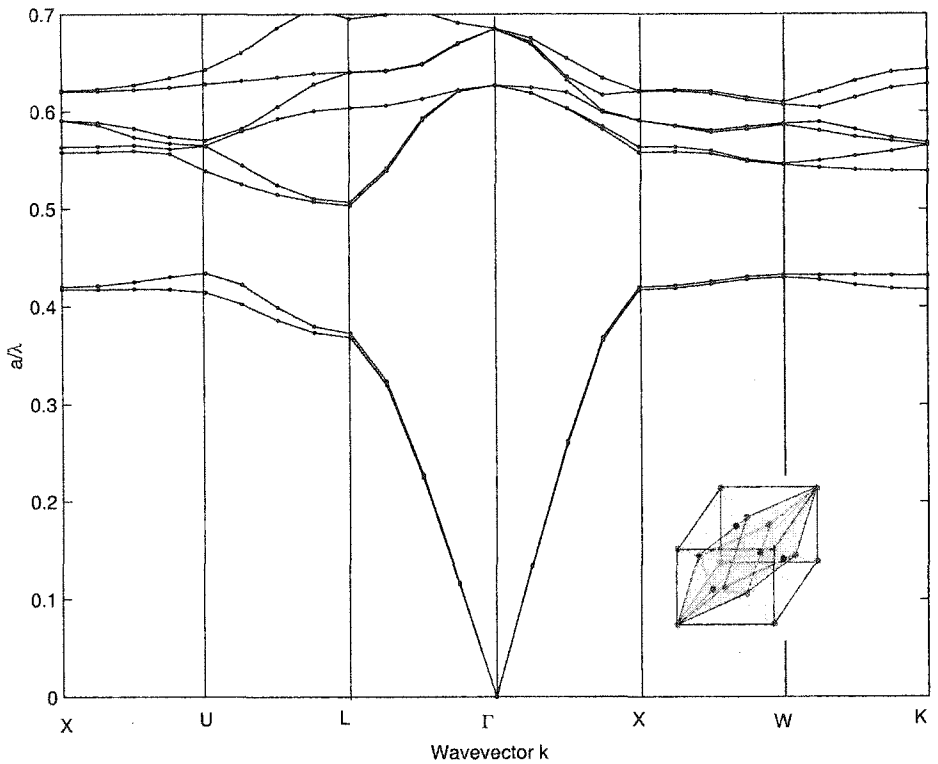

Figure 4. Band structure of a 3D diamond lattice. $(2\times3+1)^3 = 343$ plane waves are used for this calculation, the inset shows the unit cell of the diamond lattice. X, U, L, Γ, W, K are those high symmetric points in the 1st IBZ of the diamond lattice.

2.4 Algorithm Convergence, Accuracy And Stability

2.4.1 Ideal photonic crystal

We performed the TM/TE band calculation for an ideal 2D triangular lattice [68] with air holes in GaAs. The radius of the air hole is $0.28a$, where a is the lattice constant, dielectric constants for GaAs is 13.0 in the optical region. All the eigen-frequencies with k-point located at M are calculated.

Reproduced with permission of the copyright owner. Further reproduction prohibited without permission.

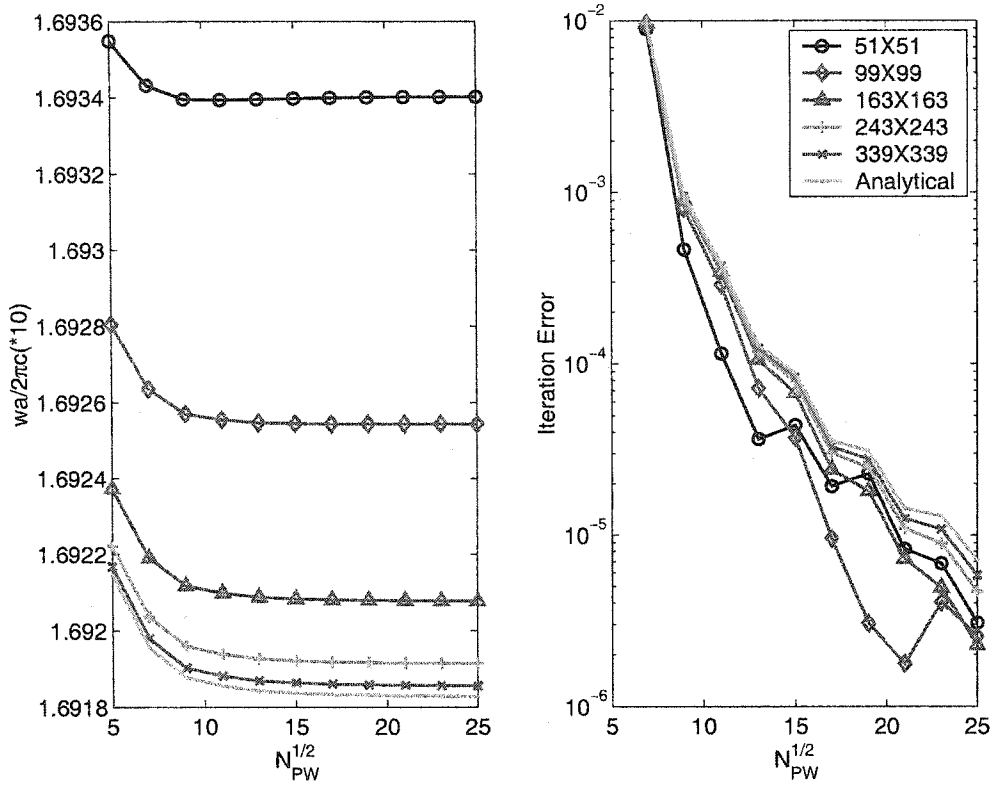

Figure 5. Eigen-frequency convergences of TM mode vs number of plane waves. Left: Convergence of the first band. Right: The iteration error for the first 10 bands. A uniform mesh with different resolution is used to represent the unit cell, each grid is averaged by a 10x10 submesh.

Figure 5 and Figure 6 show the convergence for TM and TE mode as a function of number of plane waves with different mesh resolutions. Three methods are compared: the analytical Fourier transform and FFT with each grid point averaged by a 10x10 submesh, FFT with no submesh averaging. The iteration error is calculated as $norm[X(n)-X(n-1)]$, where X(n) is the eigen-frequency vector of the first 10 bands for the nth iteration, or when the number of plane wave used is $(2n+1)^2$.

Reproduced with permission of the copyright owner. Further reproduction prohibited without permission.

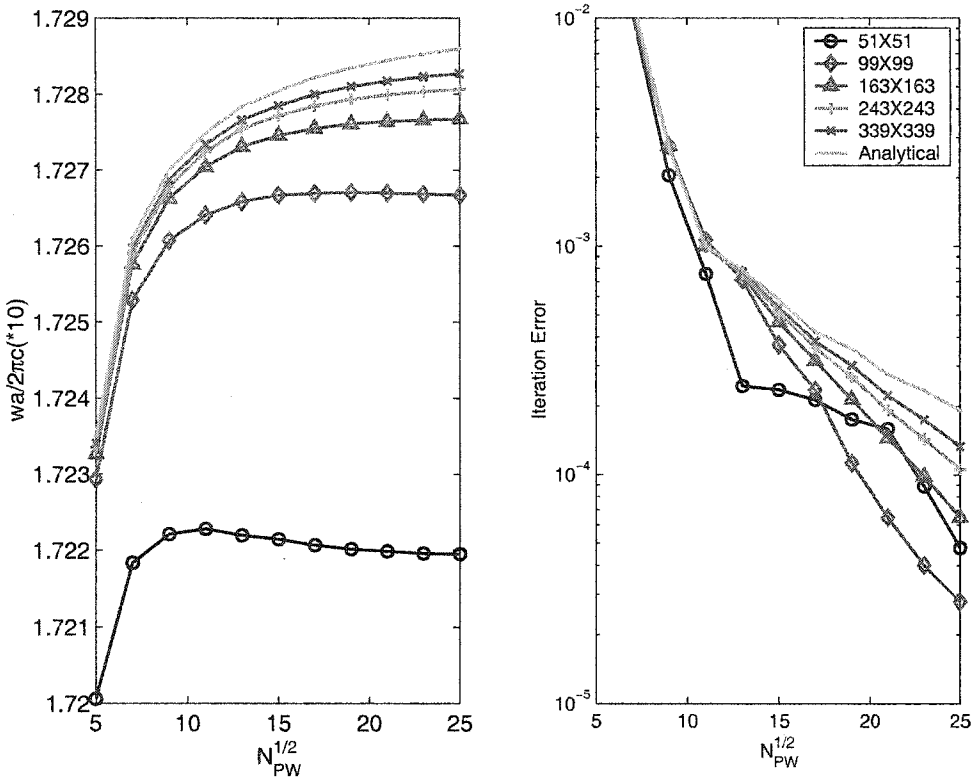

Figure 6. Eigen-frequency convergences of TE mode vs number of plane waves. Left: Convergence of the first band. Right: The iteration error for the first 10 bands. A uniform mesh with different resolution is used to represent the unit cell, each grid is averaged by a 10x10 submesh.

In Figure 5 and Figure 6, there actually exist two converging processes: number of plane waves and mesh resolutions. These two processes are almost independent on each other. To achieve accurate results, both convergences must be reached. The iteration error shown in these two figures are not enough to determine whether the accurate values are achieved, since they represent only one process. When a fine enough mesh and enough number of plane waves are used, the frequencies converge to the accurate values. The mesh grid number does not need to be the same as number of plane waves as in Ref. [69], since that makes the computation unfeasible without supercomputer in this approach. In our case, the number of plane waves is always much smaller than the grid number. For example, the grid is 339x339, the number of plane wave is only 25x25, compared to over ten thousands in Ref. [69].

Analytical method has only one converging process, also it needs no procedure to form the mesh and to perform numerical FFT. Therefore, analytical method has higher accuracy for a same number of plane waves than FFT. It can be also faster and save a lot of memory and computation

Reproduced with permission of the copyright owner. Further reproduction prohibited without permission.

time. This may be advantageous when the problem size is large and computation is long, especially for 3D cases. The reason why analytical method converges a bit slower than FFT with a certain mesh resolution (see the iteration error) is due to the Gibbs' phenomenon in Fourier series.

Convergence with mesh resolution only exists for FFT approach, shown in Figure 7 and Figure 8 for TM and TE separately and the effect of the averaging at each grid point using a finite mesh are also shown. The convergence is improved by some degree using averaging.

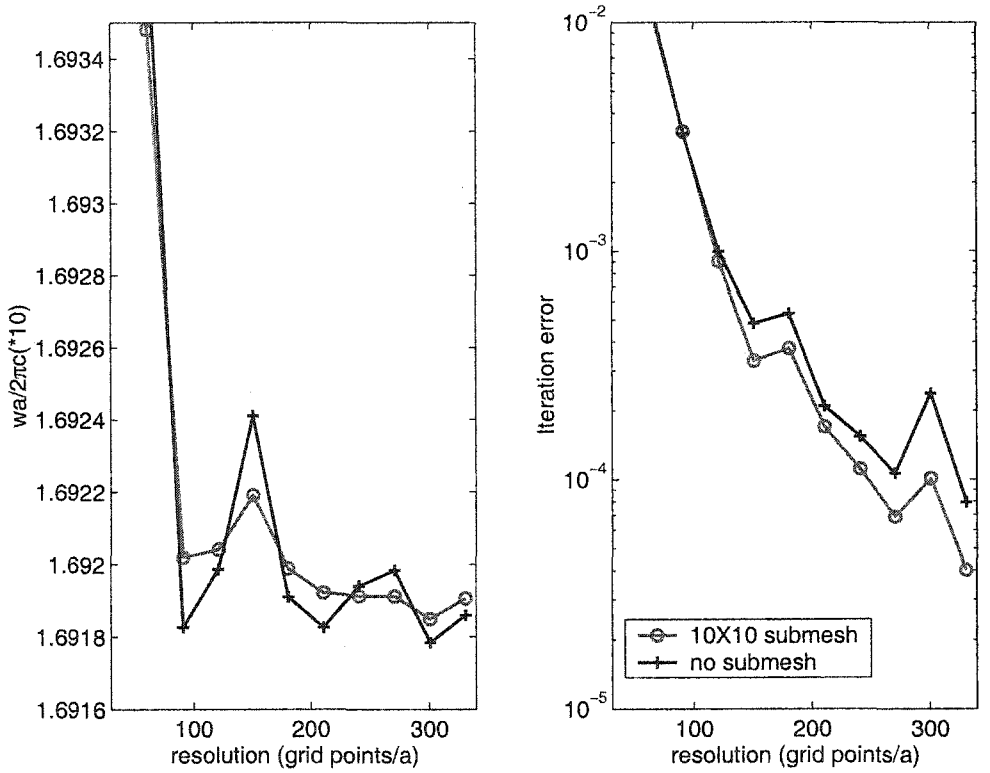

Figure 7. Eigen frequency convergence vs grid resolution for TM mode in a 2D triangular lattice. 225 plane waves are used for this calculation. Line with 'o' indicates the interface of two different materials is averaged by a 10x10 submesh, line with '+' is not averaged.

Reproduced with permission of the copyright owner. Further reproduction prohibited without permission.

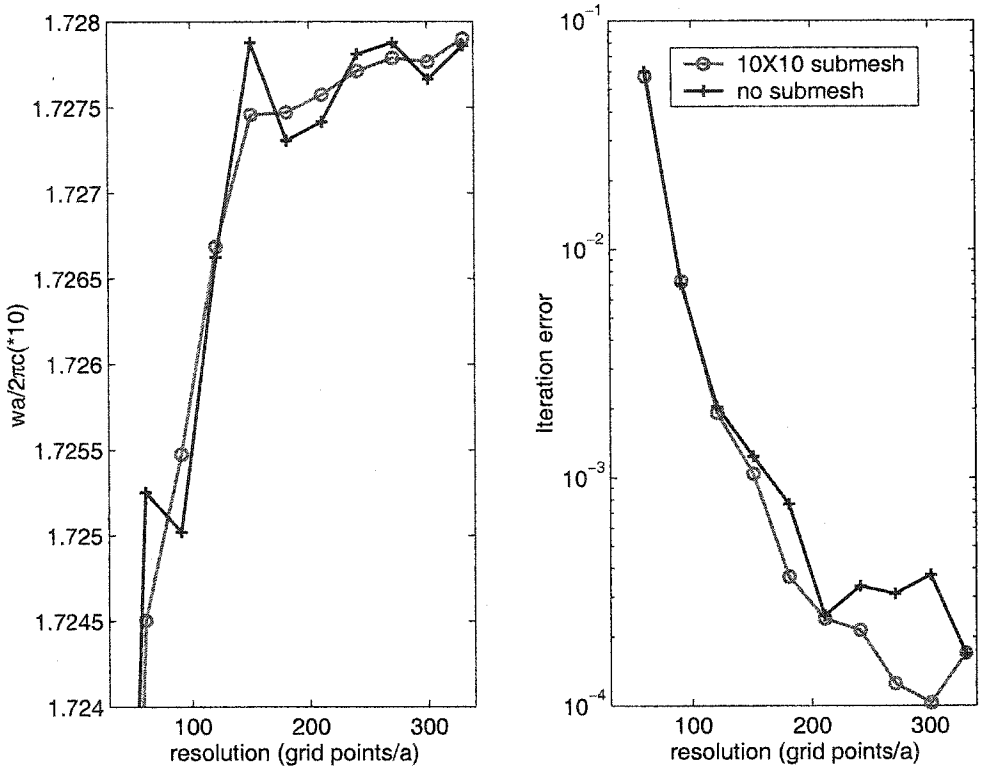

Figure 8. Eigen frequency convergence vs grid resolution for TE mode in a 2D triangular lattice. 225 plane waves are used for this calculation. Line with 'o' indicates the interface of two different materials is averaged by a 10x10 submesh, line with '+' is not averaged.

Ref. [69, 70] pointed out that for TE and TM, normal average and inverse average should be used respectively to improve convergence. However, in our calculations, the normal averaging approach is better for both TE and TM mode, which is shown in Figure 9. For TE, using inverse average approach will change the converging direction, so if these two average approaches are combined, the TE convergence will be accelerated, which we will not show here.

Reproduced with permission of the copyright owner. Further reproduction prohibited without permission.

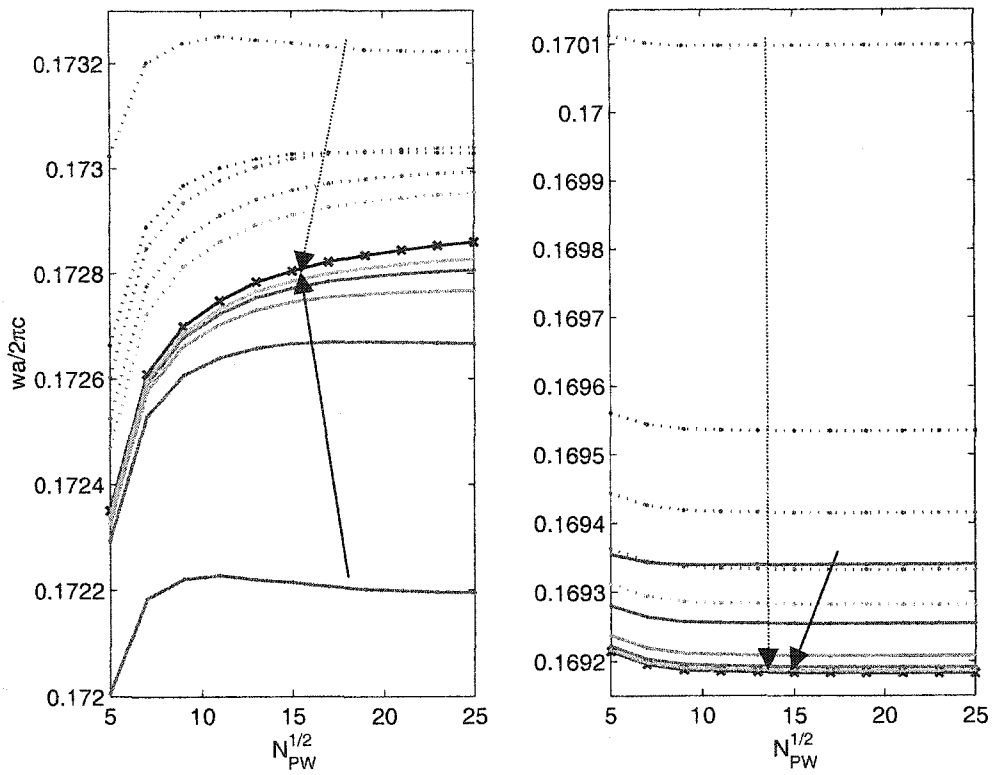

Figure 9. Convergence of eigen-frequency at M in band 1 for TE and TM with different average approach. Left: TE mode. Right: TM mode. The solid line with circles indicates the analytical results, the dotted line represents inverse average approach, the solid line represents normal average approach. Along the arrow direction, the mesh resolution along each dimension for each line is 51, 99, 163, 243, 339, respectively.

In addition, we compare our results using analytical Fourier coefficients with those recently published by Hermann et al. [71, 72], as shown in Table 2. When analytical method is used, the equivalent grid is $(4n+1)$ x $(4n+1)$, and the number of plane waves is $(2n+1)^2$, as stated above. It should be pointed out that the number of plane waves in those references is not known. Also the time for their methods is measured on other computer and is only listed as it is.

The advantage of using analytical Fourier Transform is evident from Table 2. It requires a small number of plane waves, but produces accurate results and converges quickly. This is even better when there exist some very small features in the lattice, where FFT needs very large mesh to reflect all the details.

Reproduced with permission of the copyright owner. Further reproduction prohibited without permission.

Table 2. Comparison of several methods: Accuracy, convergence and cpu time.

Method	Grid	# ofBand 1 at X	Band 2 at X	Band 3 at X	Band 4 at X	CPU-time(s)*
		PWs				
Analytical FT	-	169	0.15071	0.18778	0.31852	0.36231	2.60
Analytical FT	-	225	0.15071	0.18778	0.31851	0.36229	5.06
Our FFT	243x243	169	0.15073	0.18781	0.31855	0.36240	33.10
PWM[72]	40x40	-	0.15163	0.19066	0.31962	0.36678	99.80
Multigrid[72]	256x256	-	0.15071	0.18778	0.31851	0.36219	47.60

* Measured on a Sun Sparc 400MHz UNIX machine as a telnet user, which may vary with load on that computer.

2.4.2 Defective crystals: Supercell approximation

Crystals with defects inside can be approximated using the supercell method. In this case, a supercell includes the defect and several periods of its surrounding bulk material, and the supercell is periodically extended in the 2D plane. There might be many ways to construct the supercell, and its geometry and size can be arbitrarily chosen. The periodic defects can couple energy each other through tunneling, and form defect bands in the gap. If the distance of neighboring defects is large enough, coupling will be small and the supercell approximation is considered to be accurate enough to describe the defective crystals. As an example, two different choices of supercell in a 2D triangular lattice are shown in Figure 10. The choice of the supercell will affect the macroscopic symmetry of the crystal, but there is little effect on the defect frequency and mode field.

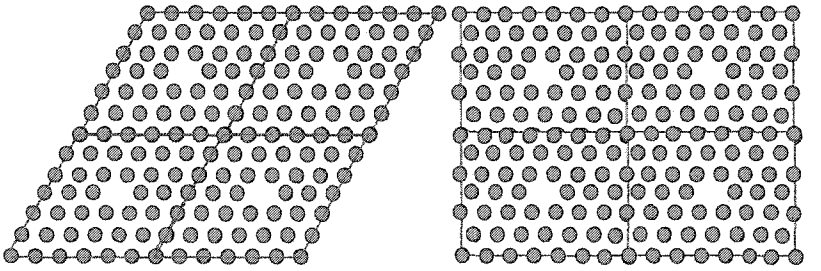

Figure 10. Supercell approximation of defective crystals in a 2D lattice. Left: triangular supercell lattice; Right: rectangular supercell lattice.

In calculation, a supercell will fold the band. If the periodicity of the supercell is n and m times of the unit cell in each basis vector direction respectively (note n and m are not necessarily integers), then each band will be folded in $n \times m$ bands since the area of the 1st BZ is reduced by $n \times m$. Figure 11 shows the folding using a 2x2 supercell for a 2D square lattice with alumina rods in air (R=0.20a).

Reproduced with permission of the copyright owner. Further reproduction prohibited without permission.

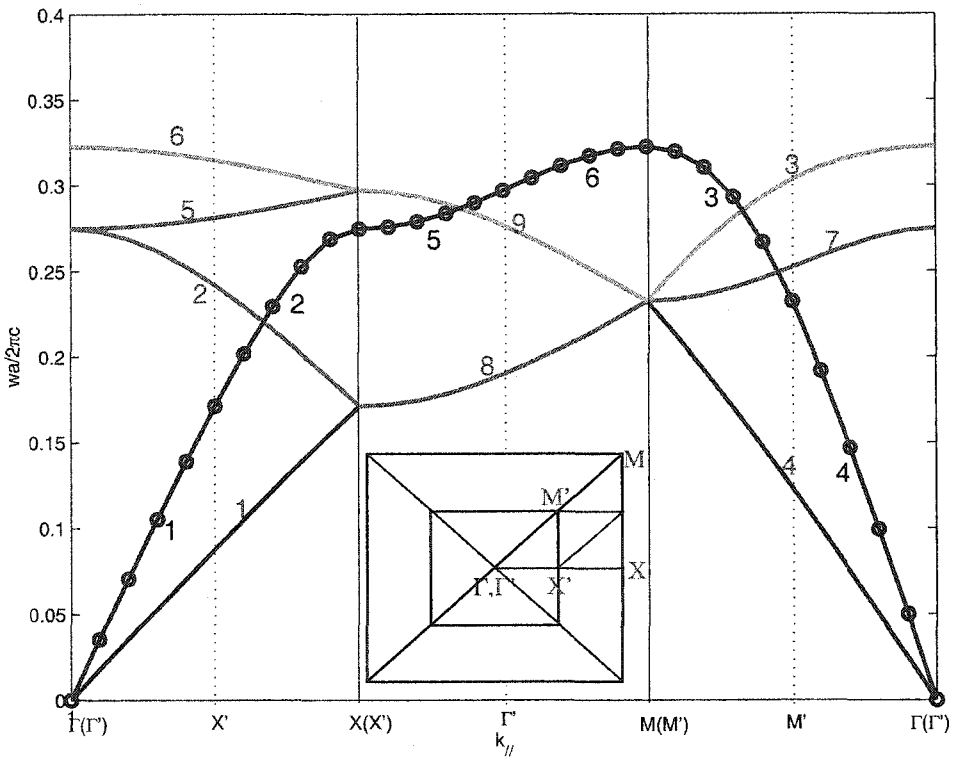

Figure 11. Band folding using supercell method. The line with 'o' is calculated using 1x1 unit cell. Solid lines are calculated using 2x2 supercell. The inset shows the BZ for two different cells.

Considering a square lattice with alumina (Al_2O_3) rods in air, a 7x7 supercell is used with the center rod being removed. The dielectric constant for alumina is 8.9 in optical region, and the radius of the rod is $0.2a$, where a is the lattice constant. The surrounding structure has a band gap for TM mode between the first band and the second band. Since the effective index for the defective structure drops compared to the ideal structure, the whole band tends to shift upwards, one band from the gap bottom will rise into the gap and form the defect band. The defect frequency in the band gap at k=(0,0,0) was calculated using different number of plane waves. We used the analytical Fourier transform and shift property to calculate these defect frequencies and the results are listed in Table 3. The iteration error is calculated as $norm[X(n)-X(n-1)]$, where X(n) is the eigen-frequency vector of the first 50 bands for the nth iteration, or when the number of plane wave used is $(2n+1)^2$. Note the band structure using a 7x7 supercell is folded 7^2 times and the defect band is band 49 in this case. We need to use more number of plane waves than that for the 1x1 supercell for the same accuracy because of the folding.

Reproduced with permission of the copyright owner. Further reproduction prohibited without permission.

Table 3. Defect frequency of TM mode in a 2D square lattice using a 7X7 supercell.

N	# of PWs	Defect freq.	Iteration Error	CPU Time(s)*
4	81=9x9	0.421996	3.6769e-02	0.49
5	121=11x11	0.415577	6.8329e-02	1.10
6	169=13x13	0.410824	3.1510e-02	2.18
7	225=15x15	0.407251	2.7674e-02	4.39
8	289=17x17	0.405432	1.6684e-02	7.45
9	361=19x19	0.404108	2.1813e-02	12.98
10	441=21x21	0.399563	2.8045e-02	20.38
11	529=23x23	0.398201	1.7524e-02	32.63
12	625=25x25	0.397168	5.4067e-03	51.49
13	729=27x27	0.396306	2.4535e-03	78.79
14	841=29x29	0.395868	2.7855e-03	112.89
15	961=31x31	0.395736	1.3450e-03	165.65
16	1089=33x33	0.395492	1.6496e-03	238.34
17	1225=35x35	0.395005	2.2181e-03	331.06

* Measured on a Sun Sparc 400MHz UNIX machine as a telnet user, which may vary with load

The defect frequency also converges with the supercell size as illustrated in Table 4, all these values have the accuracy of 0.1%. We only used odd numbers here for convenience since such supercells are inversion-symmetric and the Fourier coefficients are pure real, but even number can also be dealt with or shift it by a half period to make it inversion symmetric. For systems without inversion symmetry, the Fourier transform matrix and eigen vectors will be complex, however, the eigenvalue will be purely real [5].

Table 4. Defect frequency vs. supercell size of a 2D square lattice.

Supercell size	Defect frequency	Supercell size	Defect frequency
3x3	0.381242	13x13	0.396406
5x5	0.394169	15x15	0.396438
7x7	0.395736	17x17	0.397023
9x9	0.396130	19x19	0.398405
11x11	0.396191	21x21	0.398512

The convergence curve of the defect frequency using different supercell size is shown in the Figure 12. The convergence shows that a finite photonic crystal with a large enough size can resemble an infinite photonic crystal; in this case, a 7x7 supercell is large enough. The defect frequency for a point defect should be independent of k-vectors for an infinitely large supercell. However, for small supercells, coupling between neighboring defects will lead to a finite width of

Reproduced with permission of the copyright owner. Further reproduction prohibited without permission.

the defect frequency, hence the defect band is not a straight line. For large supercells, the interaction between neighboring defects becomes smaller.

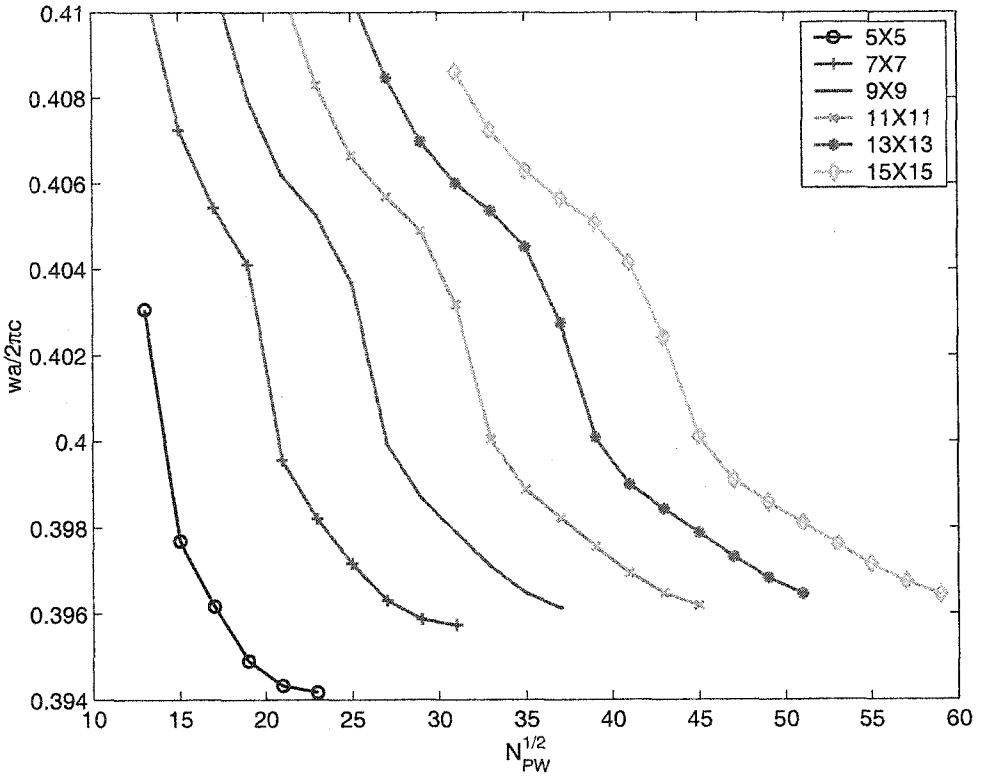

Figure 12. Convergence of defect frequency for TM mode vs the supercell size in a square lattice with the center rod being removed.

2.4.3 Mode field in photonic crystal

Eigenvectors resulting from calculation can be used to get the mode field patterns. As an example, we show in Figure 13 the field pattern for the defect mode created by increasing the radius of the center rod from 0.20a to 0.55a, using a 5x5 supercell. In the calculation, we have two kinds of 'atoms', the regular rod and the enlarged rod. The Fourier transform of the supercell is calculated using shift property. This structure supports three defect modes in the band gap, which is band 28, 29 and 30. These defect modes are drawn from the gap top since the effective index increases and the whole band tends to shift downwards. The field patterns are quadrupoles for band 28 and 29, and second order monopole for band 30. These results are comparable to those obtained by Villeneuve et al. [73]. The field obtained contains both real and imaginary

Reproduced with permission of the copyright owner. Further reproduction prohibited without permission.

parts, and each of them is the solution but with a random phase with it. We need to fix this phase to get the eigenmode field so that the modes in a PBG can satisfy the orthogonality condition [5].

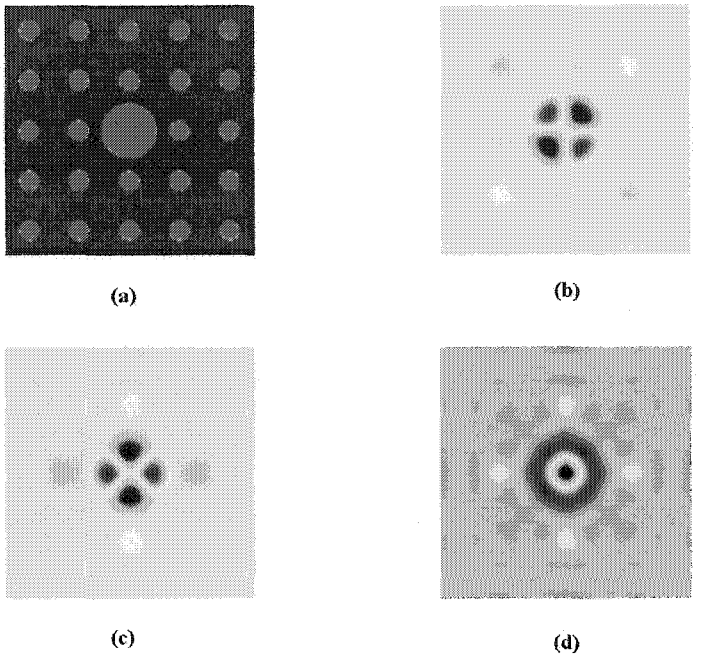

Figure 13. Mode field of defect modes in a 2D square lattice using a 5x5 supercell. (a). the dielectric function. (b). mode field for band 28, a quadrupole mode. (c). Mode field for band 29, a quadrupole mode. (d). Mode field for band 30, a second order monopole mode.

2.5 DISCUSSION

Plane wave method has been used successfully in PBG research. It is very convenient to explore the band structure and mode pattern. However, as first pointed out, it deals only with transparent, non-dispersive, lossless medium in a time-independent system. PWM has several weaknesses.

First, it cannot deal with material dispersion, since the frequency is unknown at the beginning. If the dielectric constant is a function of frequency, the problem (2.2) is no longer an eigen-value problem and no convenient tool is able to solve it on computer. Hence, it cannot deal with dispersive materials though there are several approaches trying to resolve this. For example, the metal in optical wavelength is strongly dispersive, and its dielectric constant is negative, $\varepsilon(\omega) = 1 - \frac{\omega_p^2}{\omega^2}$ where ω_p is the plasma frequency of its conduction electrons. In this case, a

Reproduced with permission of the copyright owner. Further reproduction prohibited without permission.

standard eigen-value problem can be formed using E and H for a 2D circular cylinders as in [74, 75].

Second, the computation grows fast when problem size increases. It is a formidable task to deal with complex 3D structures or a supercell with a size over 30x30 and number of plane waves over 2000, without a fast computer and large memory. In this case, a high efficiency eigen-solver is crucial to reduce computation. In [70], a block iterative eigen-solver is used to calculate one or several specific eigen values and the complexity of this eigen solver can be $O(N\log N)$.

Third, it cannot predict the dynamics of PBG devices, such as coupling, oscillation and etc. Also, it cannot predict accurately the transmission and reflection of a finite PBG device. Transfer matrix method and FDTD are better for this purpose.

Special attention should be paid to the accuracy of the calculated eigen frequency. Otherwise, an incorrect conclusion may be deduced based on the calculation. When one omits the iteration process to save time, he needs to make sure that the calculation is controlled with acceptable errors. Fortunately, if the symmetry of the system is maintained in the calculation, degeneracy, mode fields will be little affected; relative position of defect modes in the gap will also be little affected.

In this chapter, we implemented the PWM using MATLAB in our unique way. The accuracy, convergence and efficiency are analyzed in detail. They are used to explore the property of different PBG structures in different dimensions, geometry, 'atom' shape in the next chapter.

Reproduced with permission of the copyright owner. Further reproduction prohibited without permission.

CHAPTER III

TWO-DIMENSIONAL PHOTONIC CRYSTALS

In this chapter, we use the plane wave method developed in Chapter II to study the optical properties of various photonic band gap structures, mainly focused on the in-plane propagation of 2D PBG's. Since 2D PBG's are much easier to fabricate than 3D ones, they are more popular in micro-fabrication and optical integration. In the next chapter, we will consider a very important quasi-3D PBG case, the photonic crystal fiber. Photonic crystal based planar device designs and simulations are of importance. These devices can provide many novel and useful properties, such as lossless confinement of light mode, high-Q microcavity, linear waveguiding in low index material, low-loss bending, high efficiency resonant tunneling process to transfer energy between defects, and etc. In this chapter, the parameter interplay on the band gap formation is discussed first, then light modes in ideal bulk photonic crystals are investigated. Finally, interaction between defects are discussed in detail, which is crucial to planar device designs.

3.1 Band Gaps: The Parameter Interplay

3.1.1 Parameters affecting band gap

The formation of a band gap is a result of coherent multiple scattering. Two scattering mechanisms exist [54]: the microscopic scattering, governed by Mie scattering, macroscopic scattering, governed by Bragg scattering. The synergetic interplay between these two mechanisms produces a band gap where no modes can exist.

In a PBG structure, the parameters below may affect the two scattering mechaisms:

- Lattice geometry: the existence of a band gap depends on the lattice to a great degree;
- The material of the 'atom' and the background: the refractive index contrast should be high enough, to affect the scattering strength;
- The shape of the 'atom': affects the microscopic scattering pattern;
- The size of the 'atom': affects the Mie scattering pattern and strength;

Also, the finite size of real PBG structure affects the band gap and these effects will be discussed in other chapters using FDTD scheme.

3.1.2 Basic lattice structure

There are essentially only two kinds of 2D lattice structures: the orthogonal lattice and the oblique lattice for 2D structures. In orthogonal lattice, the two basis vectors are orthogonal, shown in Figure 14, which is called '2D square lattice'[76]; in oblique lattice, the two basis vectors are not orthogonal, and generally the angle between these two vectors is 60°. In these

Reproduced with permission of the copyright owner. Further reproduction prohibited without permission.

oblique systems, there are three basic lattices: the triangular lattice (also called as hexagonal lattice)[68, 77, 78], shown in Figure 15, has one 'atom' in the unit cell; the honeycomb lattice, (also called as 2D graphite structure) [79], shown in Figure 16, has two 'atoms' in the unit cell; the Kagome lattice[39], shown in Figure 17, has three 'atoms' in the unit cell. As shown in these graphs, the reciprocal lattice for these oblique lattices are the same as the triangular lattice, and so are the 1st Brillouin zone and the irreducible Brillouin zone.

The mathematical expressions for the basis lattice vectors and 'atom' positions are listed in Table 5. There may exist other ways of selection of the basis lattice vectors and 'atom' positions, this kind of selection ensures inversion symmetry of the unit cell, so the plane wave method can work most efficiently.

Lattice geometry, especially the symmetry of the lattice, is a very important factor to determine the band gap. Detailed study needs group theory [80]. These simple structures can also be combined to form some more complicated structure called as quasi-crystalline lattice [37, 81-83]. The choice of lattice geometry is determined by other factors: the band gap requirement (polarization, band gap width), available material, the difficulty of fabrication, etc. As a general rule, if the IBZ is close to a circle, then the structure is easier to produce a complete band gap.

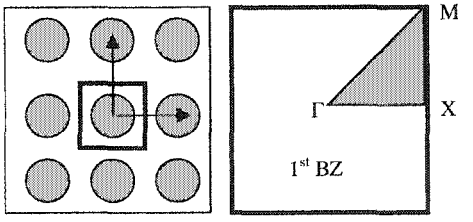

Figure 14. 2D square lattice, unit cell and Brillouin zone. Left: Unit cell and basis lattice vectors; Right: the 1st Brillouin zone and the irreducible Brillouin zone.

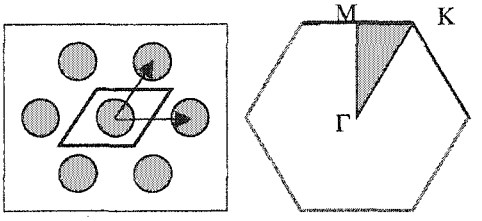

Figure 15. 2D triangular lattice, , unit cell and Brillouin zone. Left: Unit cell and basis lattice vectors; Right: the 1st Brillouin zone and the irreducible Brillouin zone.

Reproduced with permission of the copyright owner. Further reproduction prohibited without permission.

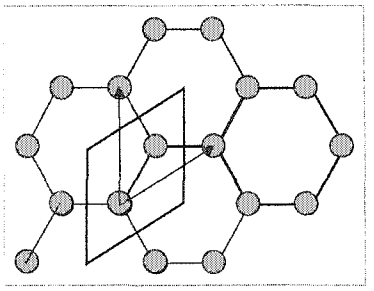

Figure 16. 2D honeycomb lattice. Unit cell and basis lattice vectors are shown. The Brillouin zone is the same as the triangular lattice.

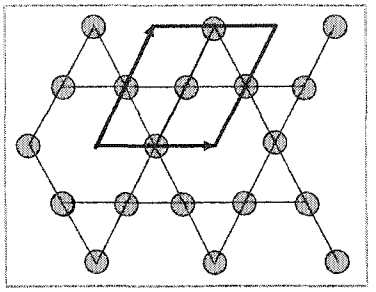

Figure 17. 2D Kagome lattice. The unit cell and the basis lattice vectors are shown. The Brillouin zone is the same as the triangular lattice.

Reproduced with permission of the copyright owner. Further reproduction prohibited without permission.

Table 5. Geometry of various 2D lattice, lattice constant a is defined as the distance between the two closest 'atoms'.

Lattice	Base lattice vector	Base reciprocal lattice vector	Atom positions
Square lattice	$\begin{cases}\vec{a}_1 =< 1,0,0 > a \\ \vec{a}_2 =< 0,1,0 > a\end{cases}$	$\begin{cases}\vec{b}_1 =< 1,0,0 > 2\pi/a \\ \vec{b}_2 =< 0,1,0 > 2\pi/a\end{cases}$	<0,0,0>a
Triangular lattice	$\begin{cases}\vec{a}_1 =< 1,0,0 > a \\ \vec{a}_2 =< \frac{1}{2},\frac{\sqrt{3}}{2},0 > a\end{cases}$	$\begin{cases}\vec{b}_1 =< 1,-\frac{\sqrt{3}}{3},0 > 2\pi/a \\ \vec{b}_1 =< 0,\frac{2\sqrt{3}}{3},0 > 2\pi/a\end{cases}$	<0,0,0>a
Honeycomb lattice	$\begin{cases}\vec{a}_1 =< 1,0,0 > \sqrt{3}a \\ \vec{a}_2 =< \frac{1}{2},\frac{\sqrt{3}}{2},0 > \sqrt{3}a\end{cases}$	$\begin{cases}\vec{b}_1 =< 1,-\frac{\sqrt{3}}{3},0 > 2\pi/\sqrt{3}a \\ \vec{b}_2 =< 0,\frac{2\sqrt{3}}{3},0 > 2\pi/\sqrt{3}a\end{cases}$	$\begin{cases} < \frac{1}{2},\frac{\sqrt{3}}{2},0 > a \\ < -\frac{1}{2},-\frac{\sqrt{3}}{2},0 > a\end{cases}$
Kagome lattice	$\begin{cases}\vec{a}_1 =< 1,0,0 > 2a \\ \vec{a}_2 =< \frac{1}{2},\frac{\sqrt{3}}{2},0 > 2a\end{cases}$	$\begin{cases}\vec{b}_1 =< 1,-\frac{\sqrt{3}}{3},0 > 2\pi/2a \\ \vec{b}_2 =< 0,\frac{2\sqrt{3}}{3},0 > 2\pi/2a\end{cases}$	$\begin{cases} < 0,\frac{\sqrt{3}}{3},0 > a \\ < \frac{1}{2},-\frac{\sqrt{3}}{6},0 > a \\ < -\frac{1}{2},-\frac{\sqrt{3}}{6},0 > a\end{cases}$

Reproduced with permission of the copyright owner. Further reproduction prohibited without permission.

3.1.3 'Atom' filling fraction

'Atom' filling fraction is to measure how dense the 'atom' is arranged in the lattice and it is defined as the ratio of the volume of all the 'atoms' to the whole space volume. The filling fractions of the 'atoms' in different lattices are (assuming the 'atoms' are circular cylinders):

Square lattice: $f = \frac{\pi R^2}{a^2}$, maximum is 78.54%.

Triangular lattice: $f = \frac{2\pi R^2}{\sqrt{3}a^2}$, maximum is 90.69%.

Honeycomb lattice: $f = \frac{4\pi R^2}{3\sqrt{3}a^2}$, maximum is 60.46%.

Kagome lattice: $f = \frac{\sqrt{3}\pi R^2}{2a^2}$, maximum is 68.02%.

The triangular lattice has the highest possible 'atom' filling fraction, and the honeycomb lattice has the lowest maximum 'atom' filling ratio. In micro-fabrication, since mostly air holes act as the 'atoms', fabrication of high air filling ratio air holes is much harder than low air filling geometry such as the honeycomb is preferred [5].

The effect of the filling ratio on band gap is not linear. The optimal value can only be determined by numerical analysis; at the same time, it is dependent on the geometry, 'atom' shape and material. In Figure 18 andFigure 19, the maps of gaps for a 2D square lattices are shown, assuming the 'atom' shape is circular cylinder, two materials are air (ε=1.0) and Alumina(ε=8.9). A total of 169 plane waves are used for calculation.

As seen, there is no TE band gap for 2D rods in air. The gap map for the inverted structure, air holes in GaAs materials, has band gaps for both TM and TE mode. Also, a complete band gap opens up when the air hole is very large.

Reproduced with permission of the copyright owner. Further reproduction prohibited without permission.

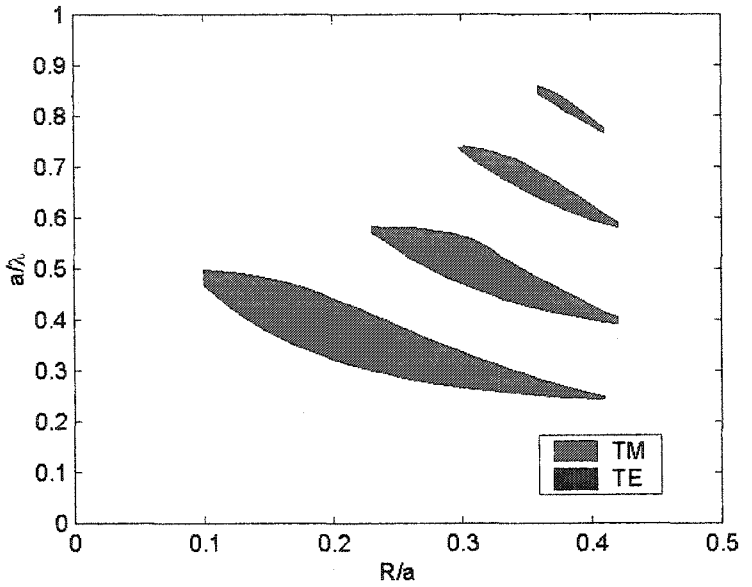

Figure 18. Gap map of a 2D square lattice with alumina (Al_3O_2) rods in air.

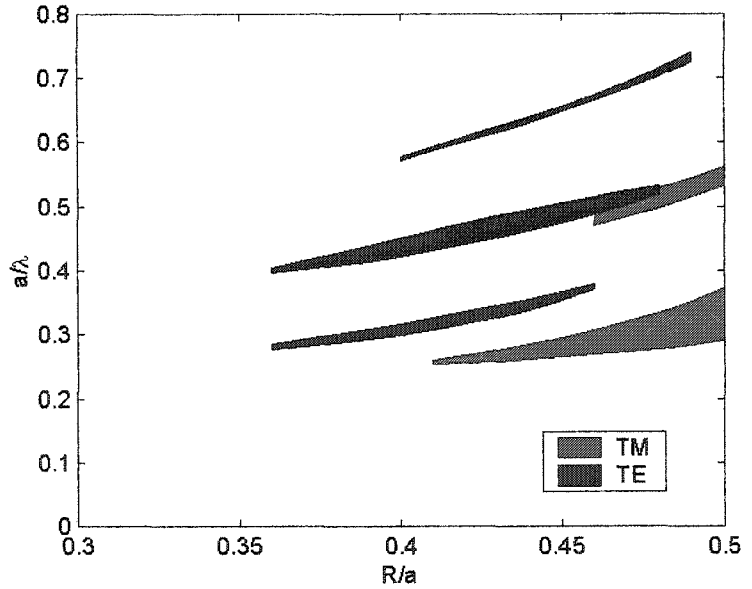

Figure 19. Gap map of inverted 2D square lattice with air holes in alumina (Al_3O_2) material.

Reproduced with permission of the copyright owner. Further reproduction prohibited without permission.

3.1.4 'Atom' shape

The 'atom' shape affects the microscopic scattering, Mie scattering, and so will affect the band gap formation. For 2D PBGs, the commonly used 'atom' shapes are: circular cylinder, square bar, elliptical cylinder, rotated bar, capillary tubes, cross, etc. For 3D PBGs, they are spheres, cubes, inverted spheres, and etc.

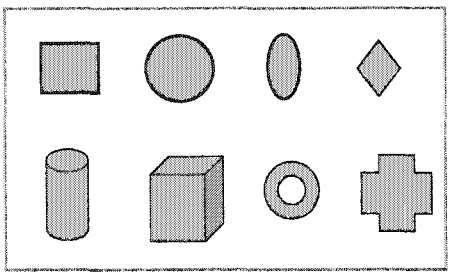

Figure 20. Basic 'atom' shape: cube, sphere, elliptical sphere, rotated bar, circular cylinder, stack, capillary tube, cross.

So far, the most commonly used 'atom' shapes are: circular cylinders for 2D PBGs, 3D spheres and inverted spheres, rectangular bar as an element to form other complex 'atom' in 3D woodpile structure, and etc. Due to the limitation of fabrication technique, other shapes are seldom used. Evaluating the effect of 'atom' shape on the PBG is hard; even the scattering of a simplest sphere object is very hard. Numerical analysis can show the difference brought by the different shaped 'atoms'.

3.1.5 Dielectric constant ratio

Generally, there are only two media in a PBG structure, the 'atom' and the background material, and very often one material is air, so actually only one material is used. Assuming the dielectric constant of the 'atom' is ε_a, and the background material is ε_b, the dielectric constant ratio of these two media can be defined as:

$$\rho = \max(\varepsilon_a, \varepsilon_b)/\min(\varepsilon_a, \varepsilon_b)$$

Once this ratio is determined, and if the dielectric constants for the 'atom' and the background material are scaled by a factor s^2 (i.e., $\varepsilon' = s^2\varepsilon$), then the band gap position will change as $\omega' = \omega/s$ and the structure of the band will remain unchanged.

There is a lower limit for the dielectric contrast ratio of each kind of lattice to reveal a band gap. This will limit the selection of materials and it depends also on the 'atom' shape and size. Increasing the dielectric constant ratio will facilitate the formation of the band gap. However,

Reproduced with permission of the copyright owner. Further reproduction prohibited without permission.

increasing the ratio infinitely will not produce an infinitely larger band gap. This can be shown using an example of a 2D triangular lattice, with air holes in high index material, assuming the radius of air hole is 0.48*a*. This structure has a band gap between the 2nd and 3rd band for TM modes. Figure 21 shows the band gap evolution as the dielectric constant ratio changes. This ratio has a lower limit at about 6.0 and the band gap size saturates when the contrast is very large.

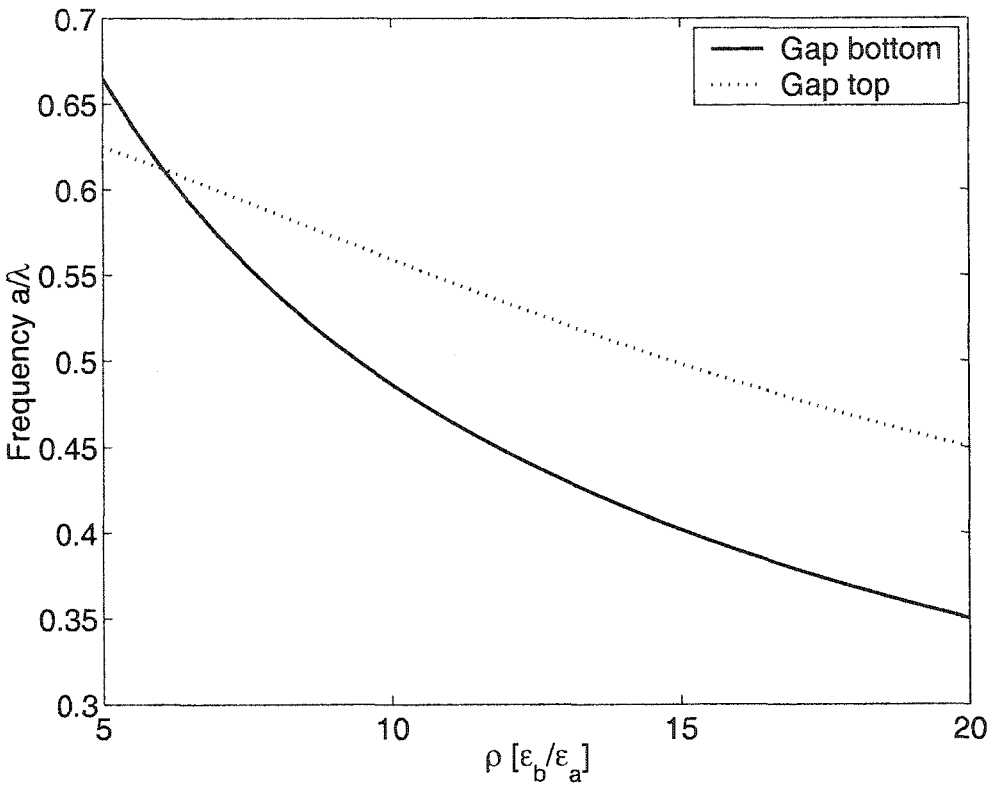

Figure 21. Band gap vs dielectric constant contrast for a 2D triangular lattice.

The requirement of high dielectric constant ratio (>3~4 when using these basic lattices) is sometimes disadvantageous, such as the efficiency reduction in coupling between the optical fiber and the PBG devices; a large fraction of power will be reflected back. Quasi-PBG material can reduce this requirement, making it possible to have a complete band gap even using glass or polymer [83].

3.2 Property Of Ideal PBG With A 2D Square Lattice

Below, we will discuss the optical properties of these lattices, taking the square lattice as an example to discuss in detail. Thus, we know the general properties of ideal PBG materials. The parameters are: Alumina rods in air, ε_a=8.9, ε_b=1.0, R=0.2*a*. The lattice and IBZ are shown in

Reproduced with permission of the copyright owner. Further reproduction prohibited without permission.

Figure 14. Using the plane wave method, its dispersion property can be obtained. A total of 169 plane waves is used in calculation.

3.2.1 Band structure

The band structure is shown in Figure 22. Note that the frequency is normalized as $\omega a/2\pi c$, or a/λ. The *k*-vectors are sampled uniformly along the edge of the irreducible Brillouin zone. A band is formed by all the states between the band top and band bottom. There is a complete band gap for TM mode between band 1 and band 2 as shown in the graph, from 0.3224 to 0.4426.

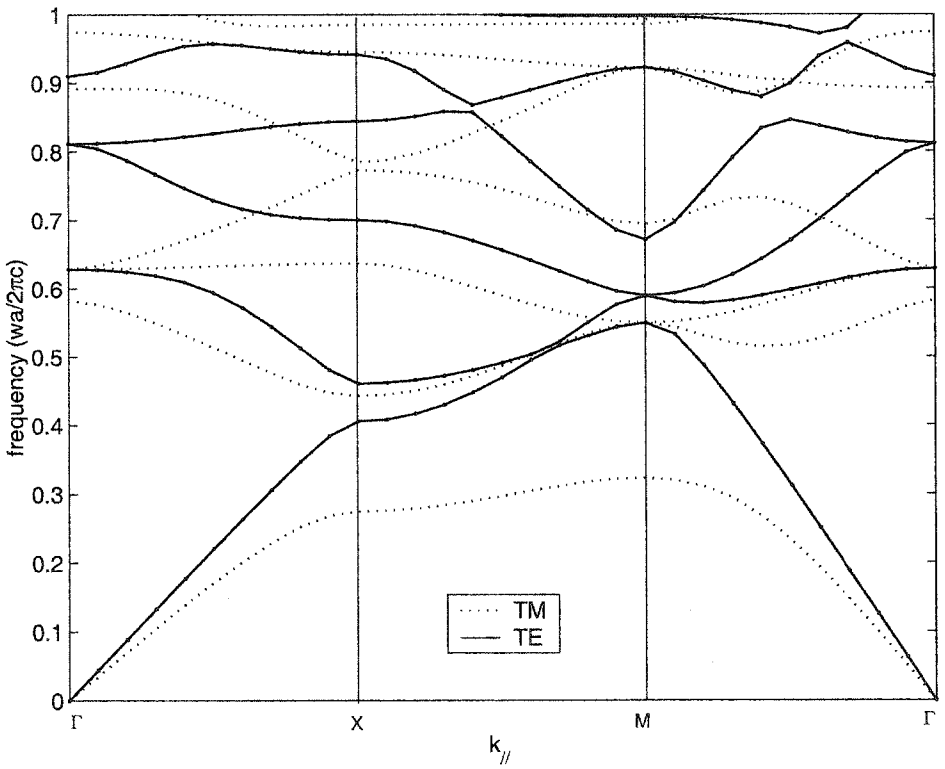

Figure 22. Band structure of 2D square lattice, with alumina rods in air, R=0.2a. A complete band gap for TM mode is between band 1 and band 2.

The band gap is generally measured using the ratio of the gap width to the mid-frequency of the gap, which in this case is 15.7%. If we need the mid-gap to work at 1.55μm, then the periodicity can be determined easily by using $a/\lambda = (0.3224 + 0.4426)/2$ and yielding a lattice constant of 0.5929μm. There is no complete TE band gap in a 2D square lattice, however, there are band gaps for some specific directions; for example, there is a local band gap in the 1st and 2nd

Reproduced with permission of the copyright owner. Further reproduction prohibited without permission.

band along the Γ-X direction. The local band gap along this direction is: 0.2747-0.4426 for TM modes, and 0.4079-0.4609 for TE modes.

3.2.2 Density of states (DOS)

The band structure provides only the information of the gap and it does not provide the information on how many states can be on the frequency. A photon state is described by its energy $\hbar\omega$ and momentum $\hbar\vec{k}$. The density of states is defined as the number of states (*k*-vectors) corresponding to a frequency. This requires that the whole 1st Brillouin zone sampled uniformly and densely. Note that those high symmetry points should be considered carefully. In Figure 23, we calculate the eigen-frequency of the TM mode for each k-vectors in the 1st BZ, by uniformly sampling the 1st BZ into 10201 (101x101) k-vectors, and then we calculate the number of states for each frequency and obtain the DOS.

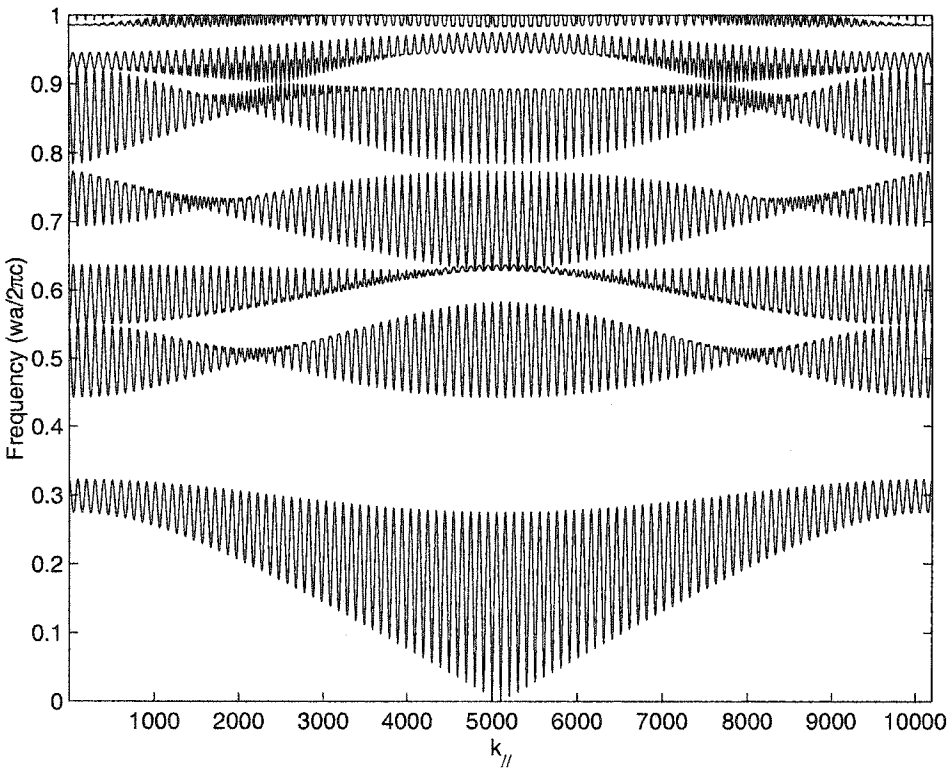

Figure 23. TM modes in a 2D square lattice with 10201 k-vectors uniformly sampled in the 1st BZ. The same lattice structure as in Figure 22 is used.

The density of states is shown in Figure 24. It is normalized using the maximum state number in the region considered. The density of states gives no information of transmission for an angle of incidence. However, if we have the projected DOS in that incidence direction, the DOS can be

Reproduced with permission of the copyright owner. Further reproduction prohibited without permission.

considered to resemble the transmittance. As shown in the band gap, the states are zero. Also, at the edge of the band gap, the DOS changes dramatically, which may find application in nonlinear and quantum effects of PBG devices[46, 84]. Compared to electromagnetic states density in vacuum, where it is proportional to ω^3, the DOS of PBG is greatly modified by the periodic structure.

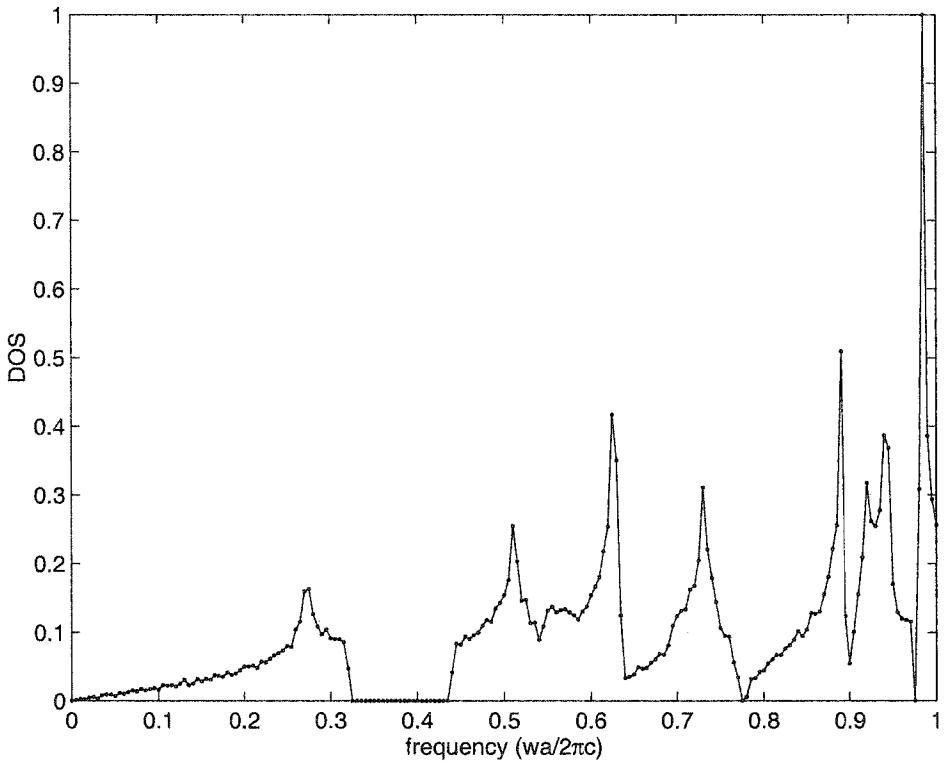

Figure 24. Density of states of TM modes in a square lattice with alumina rods in air, R=0.2a.

3.2.3 Transmission spectrum

Transmission of PBG devices can be obtained using transfer matrix methods. The method works for finite sized PBG structure. In Figure 25, the calculated transmission and reflection spectra of a 5 periods of square rods by an incidence along Γ-X direction are presented for both TE and TM modes. Along this direction, the local band gap is larger than the complete gap, which is identical to the data from the band structure in Figure 22.

However, the spectrum will not be the same as the DOS. It strongly depends on the incident conditions: if the incident wave cannot effectively couple energy to those eigen-modes in the PBG, no transmission will be observed. Also, the transmission spectrum depends on the coupling

Reproduced with permission of the copyright owner. Further reproduction prohibited without permission.

strength of the incident wave to the eigen-modes in the PBG structures. Mode pattern and symmetry are very important to understand the coupling.

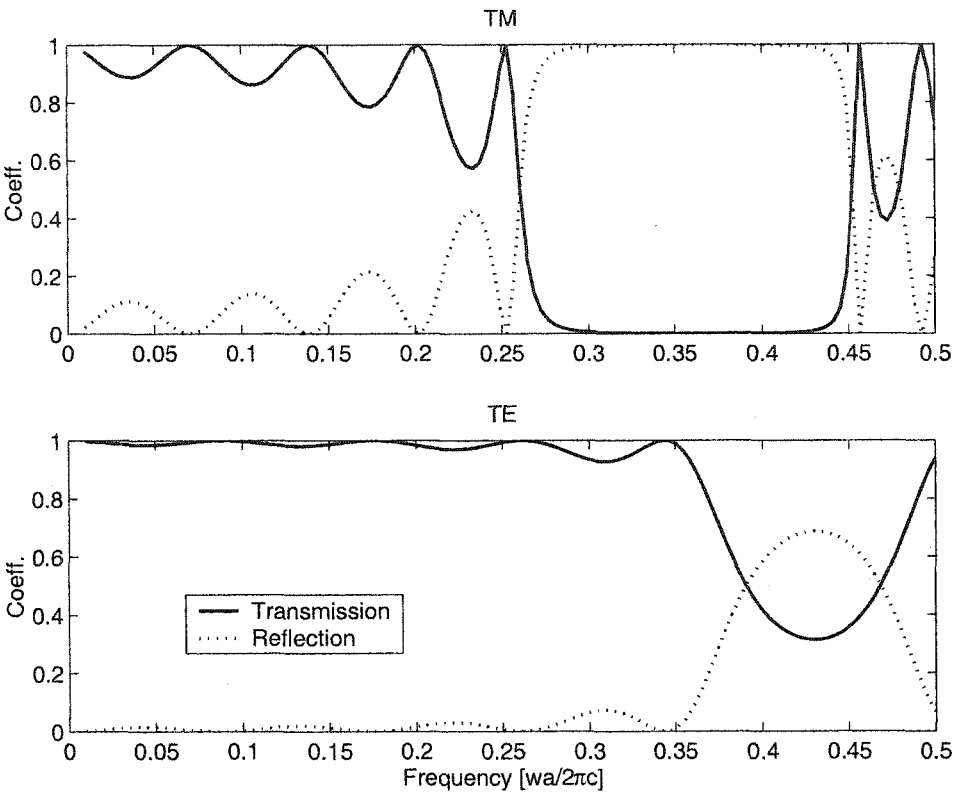

Figure 25. Reflection and transmission of a 5x5 PBG along the direction of Γ-X using Transfer Matrix Method[57].

3.2.4 Mode pattern and symmetry

To show the property of mode pattern more clearly, we calculate the modes for two PBG structures with square lattices R=0.20a and R=0.38a, the latter has two band gaps for TM modes, the first between band 1 and 2, the second between band 3 and 4. The D fields of the first 4 bands for the TM mode with k at X point and M point are shown in Figure 26.

Reproduced with permission of the copyright owner. Further reproduction prohibited without permission.

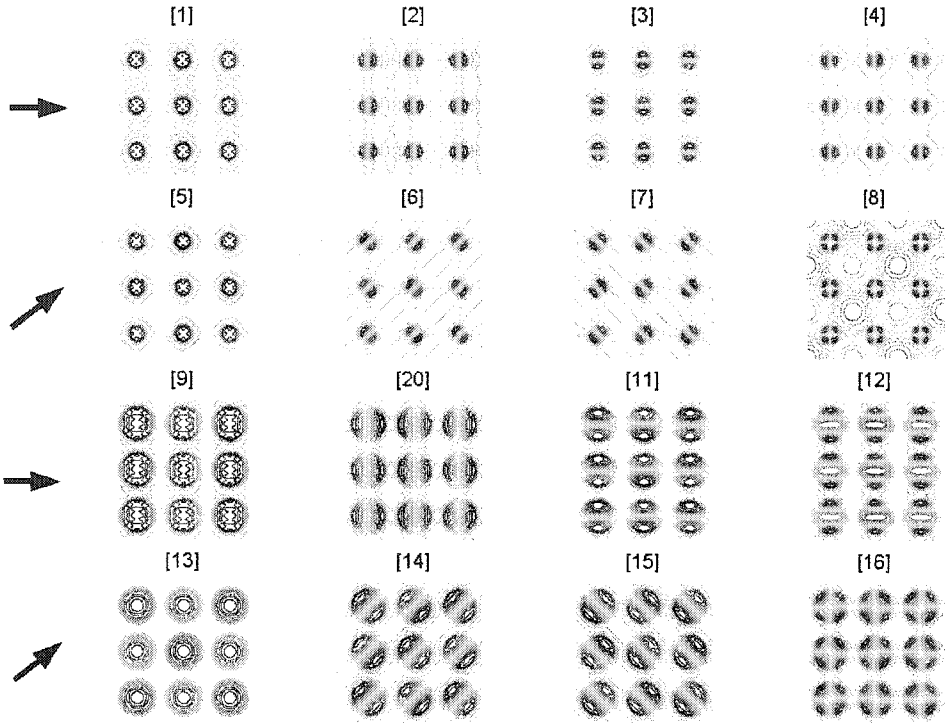

Figure 26. Displacement field (D) for TM mode in a 2D square lattice with alumina rods in air. [1-4]: the first 4 bands at X point with R=0.20a, [5-8]: the first 4 bands at M point with R=0.20a; [9-12]: the first 4 bands at X point with R=0.38a; [13-16]: the first 4 bands at M point with R=0.38a. The arrows indicate the k-vector of the plane wave.

For R=0.2a at X point (Plane wave propagates along x direction, $\vec{k} = \frac{\pi}{a}\hat{x}$), the first mode is a monopole, the 2nd to 4th mode are all dipoles; at M point (Plane wave propagates along 45 degrees direction, $\vec{k} = \frac{\pi}{a}\hat{x} + \frac{\pi}{a}\hat{y}$), the first mode is a monopole, the 2nd and 3rd mode are dipoles, the 4th mode is a quadrupole.

For R=0.38a at X point (Plane wave propagates along x direction), the first mode is a monopole, the 2nd and 3rd modes are dipoles, the 4th mode is a quadrupole; at M point (Plane wave propagates along 45 degrees direction), the first mode is a monopole, the 2nd and 3rd mode are dipoles, the 4th mode is a quadrupole.

From the graph, the mode pattern in PBG structure has the following properties:

1. The mode field is a plane wave along k-direction modulated by a periodic function, just as indicated by Bloch theorem.

Reproduced with permission of the copyright owner. Further reproduction prohibited without permission.

2. Modes inside the same band will not always have the same mode field pattern, which relates to the k-vector.
3. Mode fields in neighboring bands are orthogonal except those degenerate bands; the lower bands have more energy concentrated in the high index area, and higher bands have less energy. For example, the lowest continuous band (i.e. including those neighboring bands without band gap among them) is likely a monopole, the second continuous band will be likely a dipole, and the 3rd continuous band will be likely a quadrupole.
4. If there is a band gap between the neighboring bands, the mode fields show a large difference. At the same time, the different mode pattern may also indicate the possibility of the opening of a band gap there.
5. All modes are symmetric or anti-symmetric regarding to the k-vector of the plane wave.

Confusion may occur between these eigen-modes and modes excited by an incident plane wave. The eigen-modes are true states allowed by Maxwell's equations and Bloch's theorem in an infinite periodic structure. They are modulated 'plane waves', but they cannot always be excited by a plane wave incidence due to the mode coupling. The excitation plane wave should have a component of the eigen-mode to be able to excite it. This is important for transfer matrix method and FDTD method to ensure all eigen-modes are excited. If the incident plane wave is a TM wave with Ez parallel to the rods, those anti-symmetric modes along the k-vector will not be excited since the coupling of the incident field and eigen-mode field is zero. In this case, dipole or other multi-pole sources should be used to excite these modes, which will be discussed further in Chapter V.

3.2.5 Other lattices

There is no fundamental difference between the square lattice and other oblique lattices, Programs for these lattices are available, and they are not discussed here in detail. These three lattices can all provide complete band gap for both polarizations. To facilitate a complete band gap, the 1st BZ (or the unit cell in the reciprocal space) of the lattice should be close to a circle. In some complex 2D systems, such as some quasi-periodic systems, their BZs can be very circular and they are able to produce a large band gap for both polarizations.

3.2.6 PBG structures in reality

So far, we have dealt with only the infinite ideal PBG structures. In reality, the structure is always of finite size. When the size is large enough, these finite structures behave very close to what is predicted by theory.

Reproduced with permission of the copyright owner. Further reproduction prohibited without permission.

In optical integrated circuits, 2D PBG films are used. These films are very thin, only several wavelength long in z-direction. There will be no complete band gap for these PBG films. Index guiding in z-direction is used to confine the light. Band gap for those guided modes may exist to confine light in transverse direction. These devices should be treated as a 3D PBG structure and are not discussed here.

3.3 DEFECTIVE PBG

When disorder is introduced into an ideal PBG, localized states are formed in the band gap, since these states cannot propagate through the surrounding PBG material. Many useful devices can be designed using defects in PBG materials. These defects can be introduced by changing the size of 'atoms', removal or addition of 'atoms', changing the refractive index of 'atoms', and etc. Among them, point defects and line defects are the two fundamental forms.

3.3.1 Point defects: High Q Microcavities

A defect can be created by changing the size of a single 'atom' in the lattice. The whole effect will be a change of the average index of the medium. As a general rule, if the defect causes the average index to increase, the eigen-frequency will drop and one or more bands from the upper band edge may drop into the band gap, creating so-called 'donor' defect bands. If the defect causes the average index to decrease, the eigen-frequency will shift to higher direction, and one or more bands from the band bottom may emerge into the band gap, creating the so-called 'acceptor' defect bands. The concept of 'donor' and 'acceptor' are from semiconductor.

As an example, we change the radius of a single Alumina rod in a 2D square lattice, and the defect will form a micro-cavity, which can form localized state inside the cavity. The defective crystal is modeled using a 9x9 supercell with the defect in the center, and 841 plane waves are used for calculation. The radius of the rod is 0.20a, and the band gap for TM modes is in the range of 0.32 to 0.44 as calculated in previous section.

The band gap for a defective crystal with the center rod removed is calculated and shown in Figure 27. The band structure is folded 9^2 times and a defect state forms in the band gap. The defect bands are independent of the wave vector k and are generally discrete bands. Finite widths of bands are partly introduced by the coupling between neighboring defects, as a result of the supercell approximation of the defective photonic band gap structures. The lineshape of the defect mode is Lorentzian, which is similar to the one-dimensional Fabry-Perot cavity.

Reproduced with permission of the copyright owner. Further reproduction prohibited without permission.

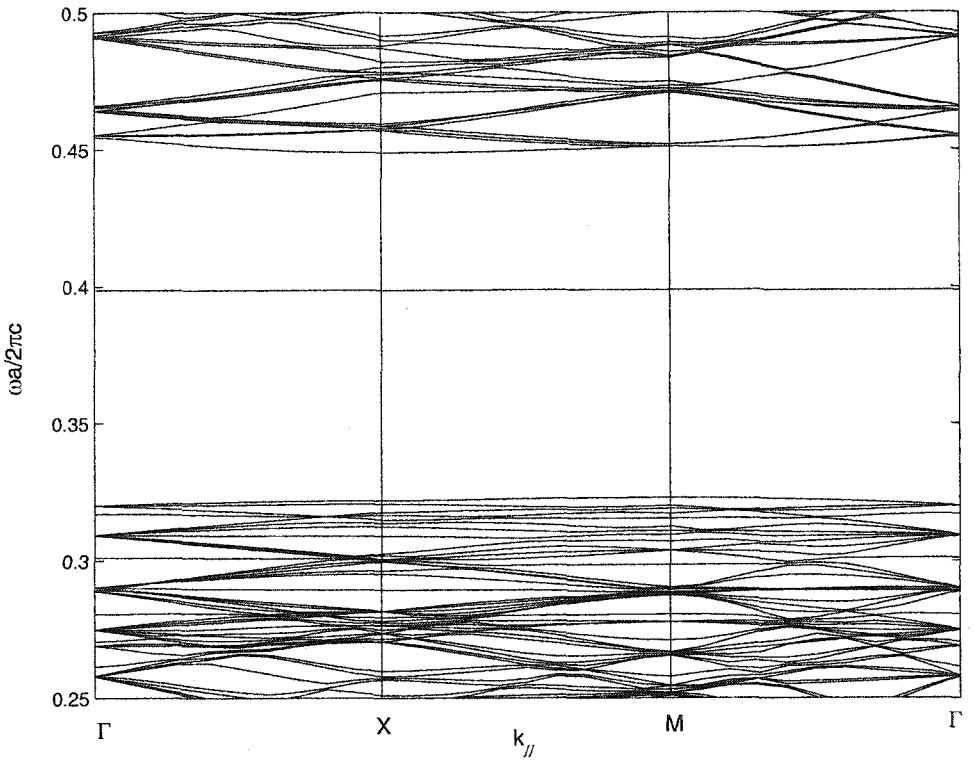

Figure 27. Band structure of a 2D defective square lattice with Alumina rods in air. A defect is formed by removing the center rod. R=0.20a, 9x9 supercell; 841 plane waves are used.

The defect frequency can be tuned by changing the size of the rod or its dielectric constants. The tuning by changing radius is shown in Figure 28 and the tuning by changing dielectric constants is shown in Figure 29. A 9x9 supercell is used in the calculation and the number of plane waves is 841.

The graph shows clearly the evolution of the 'donor' and 'acceptor' bands. When the radius of the defect is decreasing from the regular one, band 81 will rise into the band gap and an acceptor level forms. When the radius of the defect is increasing from the regular size, band 82 and even higher bands will drop to the band gap and form several donor defects. There are several two-fold degenerate states, which are curve 2 for band 82 and 83, curve 6 for band 87 and 88, curve 7 for band 89 and 90.

Reproduced with permission of the copyright owner. Further reproduction prohibited without permission.

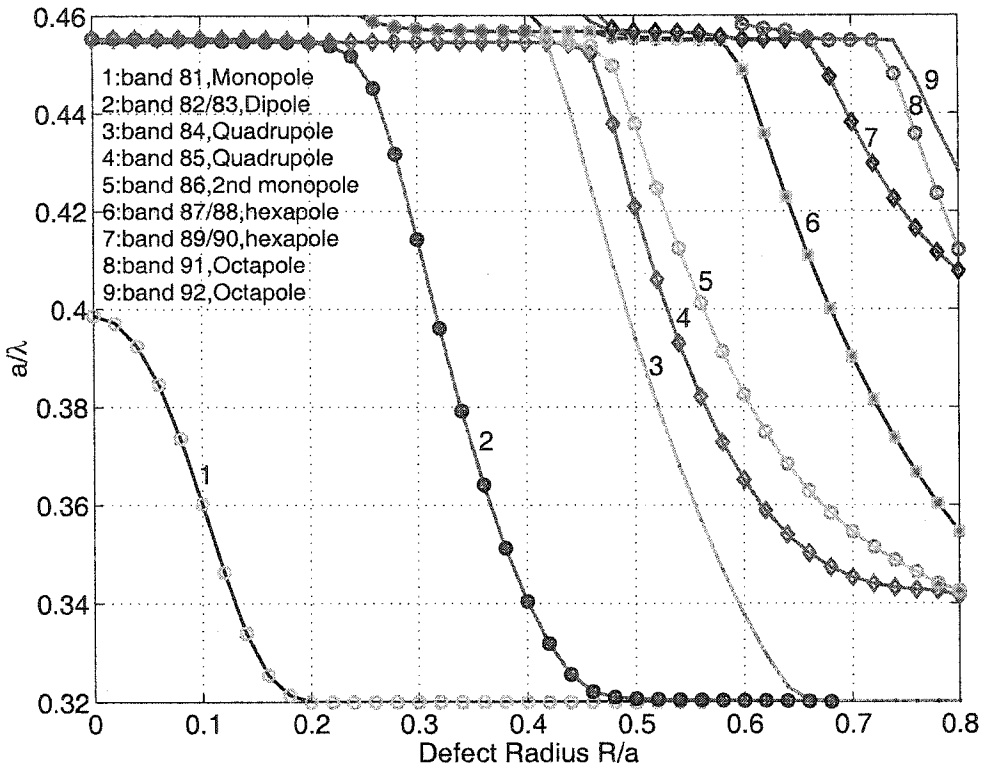

Figure 28. Defect frequency tuning (TM mode) by changing the size of a single 'atom' in a 2D square lattice with alumina rods in air. ε_a=8.9, ε_b=1.0, R=0.20a. A 9x9 supercell and 841 plane waves are used in the calculation.

Tuning by refractive index is less effective, as shown in Figure 29, when the dielectric constants of a single rod is increaseed almost one time higher than the regular rods, no defect mode is sufficient to localize and exist in the cavity. Compared to the cavity created by changing radius of a single rod, this cavity works as a single mode in a broad tuning range, which is beneficial for single mode operation. The difficulty might be the incorporation of the high refractive index materials.

Reproduced with permission of the copyright owner. Further reproduction prohibited without permission.

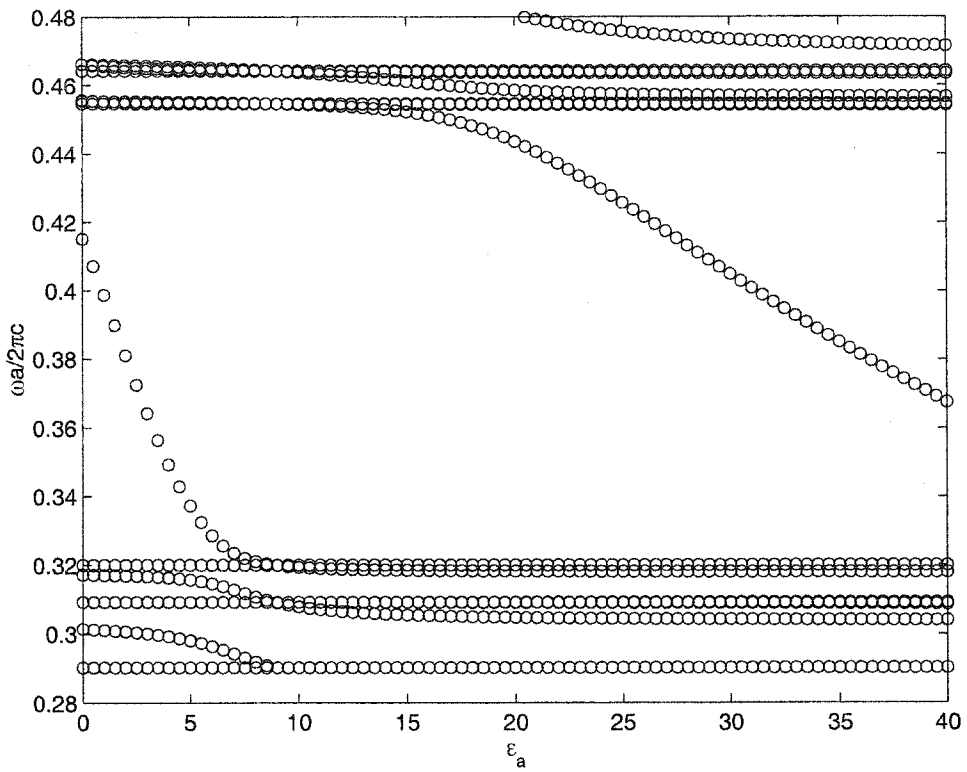

Figure 29. Defect mode frequency tuning by changing the dielectric constants of a single rod in a 2D square lattice of alumina rods. R=0.20a.

Since no light in the gap can pass through the surrounding bulk materials, defect mode will be evanescent in the bulk material, thus a two-dimensional resonant micro-cavity is formed. The size of the cavity is very small, comparable to the light wavelength. This can be numerically measured by the degree of field confinement in the cavity or the field decay constant.

The quality factor, or the Q value of the cavity could be very high. The Q value is defined as the number of oscillations of light in the cavity before its energy decays by a factor of $e^{-2\pi}$ (or approximately 0.2%). It can also be measured by $\frac{\omega_0}{\Delta\omega}$ where $\Delta\omega$ is the FWHP (Full width at half power). The Q value increases while the size of the surrounding bulk material increases, and could be up to 10,000's. Plane wave method cannot yield Q information and time domain simulation is often used by exciting the defect mode in the cavity and then monitoring the field oscillations.

Since the bulk material is a lossless material, the power loss in the microcavity is not through absorption but through a so-called tunneling process. Tunneling process is a quantum effect,

Reproduced with permission of the copyright owner. Further reproduction prohibited without permission.

where there is a possibility of photons that transmit through potential barrier. When the potential barrier is changed, the possibility of tunneling process will also change. In classical electromagnetic theory, the coupling strength is directly determined by the field overlap.

The defect mode patterns in the 2D square lattice will be investigated in detail below. Special attention should be paid to the symmetries and degenerate modes in band gap. The degenerate states are due to the symmetry of the structure. They have different mode patterns with the same frequency.

Bands inside the gap bottom may raise themselves into the gap and form the defect band(s): band 81. The defect mode field is a monopole with most energy concentrated in the defect including the first ring of nearest four rods, as shown in Figure 30(a), and the field is evanescent in the bulk region (but still modulated by the periodic function as indicated by Bloch's theorem). The degree of light confinement in the micro-cavity (the imaginary part of the wave vector k) is directly related to the position of defect band in the gap. When R is getting a bit larger, the defect frequency is closer to the gap bottom (a shallow acceptor) and the field is less confined. Comparing the eigen modes in the bulk material (the monopole mode at M in Figure 26) with the defect modes, one can see that they are similar in mode patterns except that the defect modes are multiplied by an exponential-decay function. Other defect modes show similar features as discussed above.

The dipole modes, defect band 82 and 83, are degenerate because of the two-fold symmetry of the crystal structure. The mode pattern is a dipole (shown in Figure 31) and the linear combinations of the two modes are also shown in the figure. According to the property of eigen modes discussed in Chapter II, the combinations are also eigen modes. In fact, the combined modes are more convenient to use since they show the same symmetries as the bulk crystal. The two modes are dipoles with symmetric and anti-symmetric property, the first one is even to the mirror plane parallel to x and odd to the mirror plane parallel to y (assuming the origin is the center); the second mode is odd to x and even to y.

When R=0.55a, three non-degenerate modes can be excited, and these modes are shown in Figure 30(b-d). The mode patterns are quadrupole and second order monopoles (a ring in the monopole). The quadrupole for band 84 is odd to both x and y, and a nodal plane passes through x and y. Band 85 is even to both x and y, and the maximums are in the axis.

Reproduced with permission of the copyright owner. Further reproduction prohibited without permission.

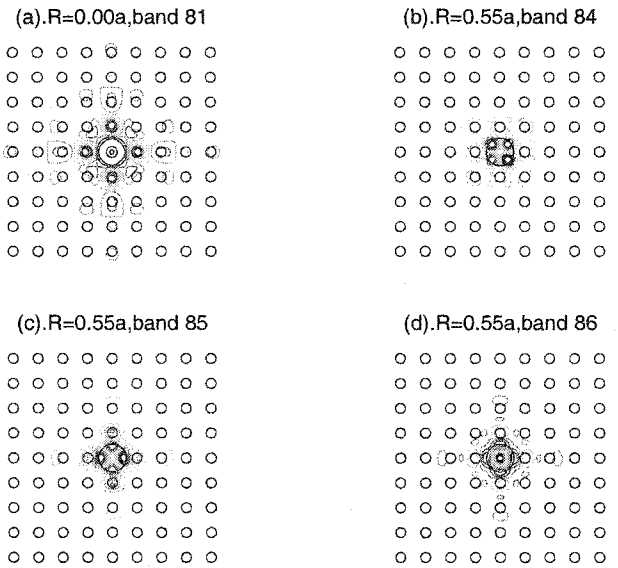

Figure 30. Monopoles and quadrupoles in the micro-cavity. (a). Monopole pattern, R=0.0a, band 81. (b). R=0.55a, band 84. (c). R=0.55a, band 85. (d). R=0.55a, band 86.

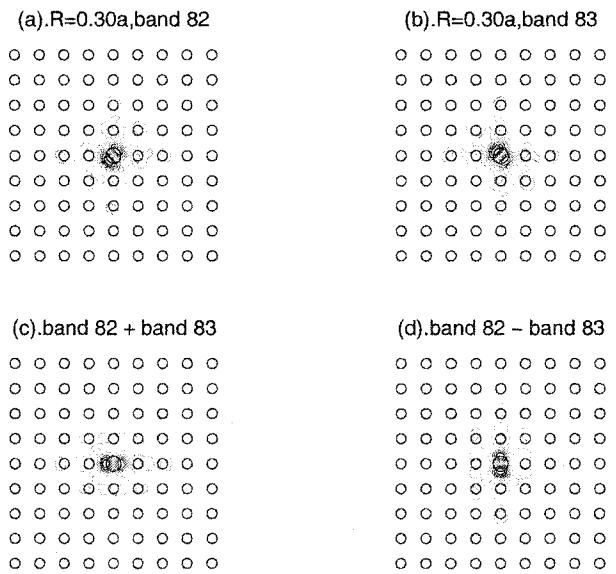

Figure 31. Doubly-degenerate dipole mode pattern formed by a donor defect with R=0.30a. (a). Mode field of band 82. (b). Mode field of band 83. (c). The addition of two degenerate modes. (d). The subtraction of two degenerate modes.

Reproduced with permission of the copyright owner. Further reproduction prohibited without permission.

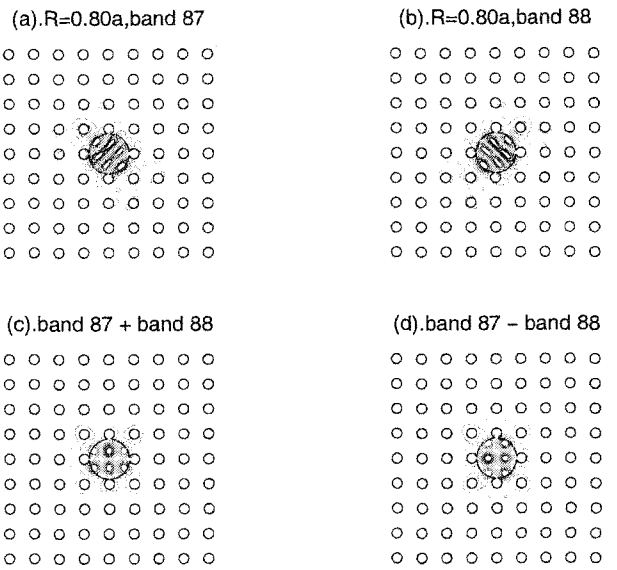

Figure 32. 1st doubly-degenerate hexapole modes formed by a donor defect with R=0.80a. (a). Mode field of band 87. (b). Mode field of band 88. (c). The addition of two degenerate modes. (d). The subtraction of two degenerate modes.

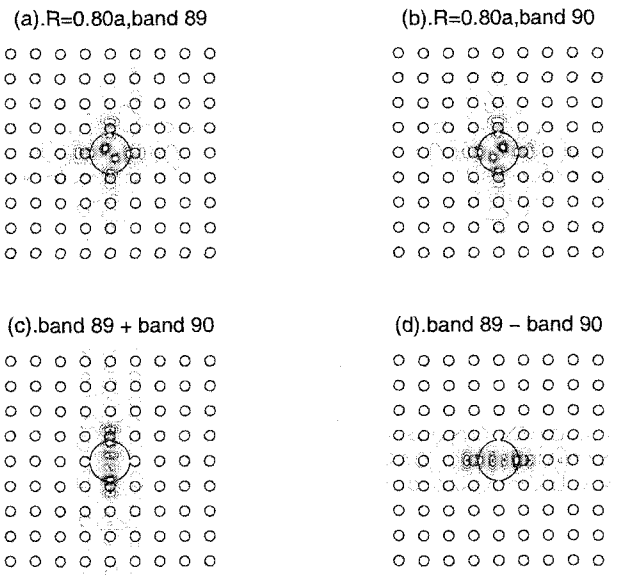

Figure 33. 2nd doubly-degenerate hexapole modes formed by a donor defect with R=0.80a. (a). Mode field of band 89. (b). Mode field of band 90. (c). The addition of two degenerate modes. (d). The subtraction of two degenerate modes.

Reproduced with permission of the copyright owner. Further reproduction prohibited without permission.

For larger R (060a~0.80a), two degenerate hexapole modes (band 87, 88, and band 89, 90) will be excited (shown in Figure 32 and Figure 33). Similar to the degenerate modes previously discussed, the degeneracy is produced by the crystal symmetry and one mode can be obtained by rotating the other mode 90 degrees. For band 87 and 88, the combined modes are odd to one axis and even to the other axis, and maximums and minimums are aligned in two rows (columns) with a nodal plane between them; for band 89 and 90 there is only one row (column).

The calculated localized modes are also solution of the Maxwell's equation and Bloch's theorem, and they can also be expressed as $e^{-i\vec{K}\bullet\vec{r}}u(r)$ according to Eq. (2.5), where K is the 'plane wave' vector and u(r) is the periodic function representing the modulation across the periodic supercells and the field distributions. Inside the supercell, u(r) is evanescent in any direction and modulated by the microstructure of the supercell. So, u(r) inside the supercell has the form of $e^{-\kappa_x x-\kappa_y y}e^{-i\left(k_x x+k_y y\right)}$ where k_x and k_y are the wave vectors along x and y direction indicating an oscillating feature in the field pattern induced by the inner microstructure, κ_x and κ_y represent the field decay constants in space. If the inner structure is symmetric, the decay constants and wave vectors are equal along x and y direction, and that is the case for square lattice. The size of the microcavity can be quantified using the field decay constant in space.

Excitation of defect modes is through resonant tunneling. The excitation source should have some components of the defect modes; otherwise, the defect modes will not be excited. As previously discussed, the plane wave incidence will not be able to produce those defect modes with anti-symmetric property in regard to the k-vectors, but they could be excited using dipole or multi-pole sources.

Point defect based microcavity is very small sized, has an extreme narrow spectral width and high Q values. It can act as a high-Q filter or a center of energy transfer. The coupling is strongly dependent on the field pattern, more important the far-field (the far field pattern can show along which direction the field diffraction is strongest), mode symmetry and its decay constants or Q-values. Those dipole or multi-poles have larger angular momentum and generally are more stable and possess higher Q values. This can be seen from the mode pattern, the field is mostly confined in the defect rod and neighboring rods are not part of the microcavity. The principle of the interaction is very important to designing such kind of devices, and the dynamic process will be simulated using FDTD in Chapter V.

3.3.2 Line defect

Line defects can act as linear waveguides in optical integrated circuits. It can be created by removal or addition of a column/row of 'atoms' from the ideal PBG structure. Figure 34 shows a

Reproduced with permission of the copyright owner. Further reproduction prohibited without permission.

waveguide formed in a 2D square lattice with alumina rods in air, R/a=0.20. One column of rods along y-direction is removed. The guide mode is confined in the air region by photonic band gap effects, so these waveguides can have minimum material loss and nonlinear effect. Also, they are different from the conventional waveguide based on total internal reflection that only supports a small portion of incident light; the PBG waveguide is an omni-directional guide that guides light incidence in every direction.

The calculated band structure is shown in Figure 34 using a supercell 7x1 as indicated in the inset. The choice of the supercell is important to reflect its periodicity along the waveguide direction. As seen, the waveguide has a period of lattice constant *a* along y-axis, experiencing a similar effect as the distributed Bragg reflector.

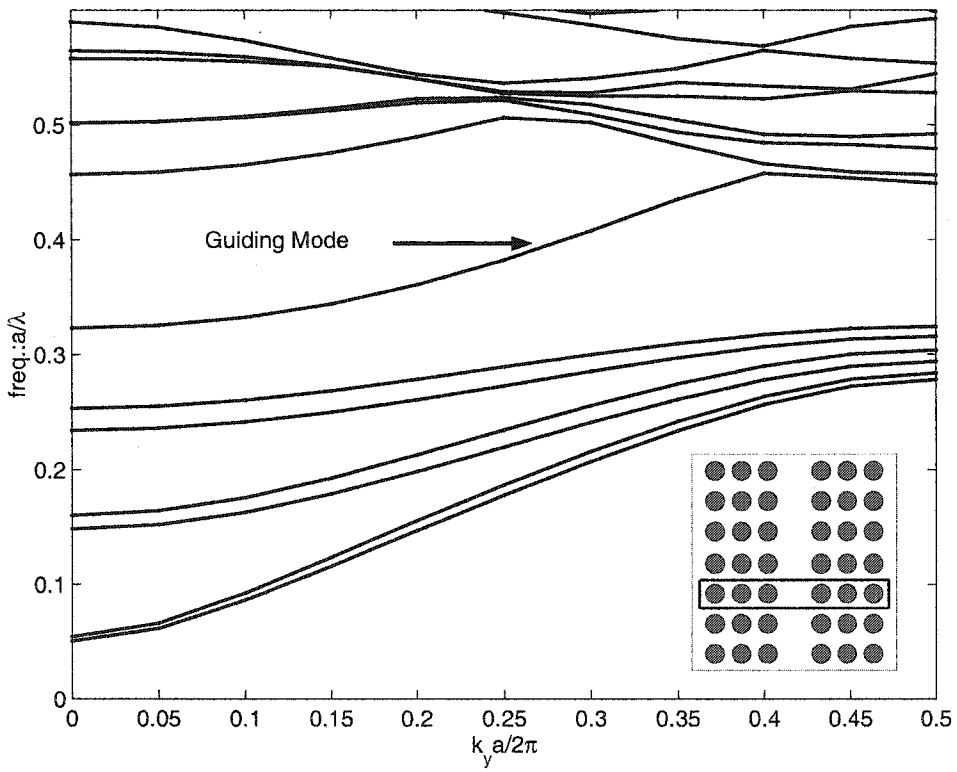

Figure 34. Guiding mode in waveguide formed by removal of a column of rods in a 2D square lattice. The inset shows the crystal structure and the supercell used.

A single guided mode is supported in the waveguide. Its frequency covers the whole band gap (0.32-0.45). The dispersion curve shows some nonlinear effects in the lower frequency range. In the lower and higher end, guided mode is lossy since it can couple energy into other non-guiding modes.

Reproduced with permission of the copyright owner. Further reproduction prohibited without permission.

The guided mode pattern at the upper end of the dispersion curve is shown in Figure 35. The guiding mode is confined by the neighboring dielectric rods and part of the energy propagates in the neighboring rods. They are even symmetric to the mid-line along the waveguide since the crystal is symmetric to the plane along the center of the waveguide. Modes with odd symmetry and other patterns can be shown using a row of increased rods. In the lower and upper end of the dispersion curve, the mode has a large part in the cladding region, making it a lossy mode.

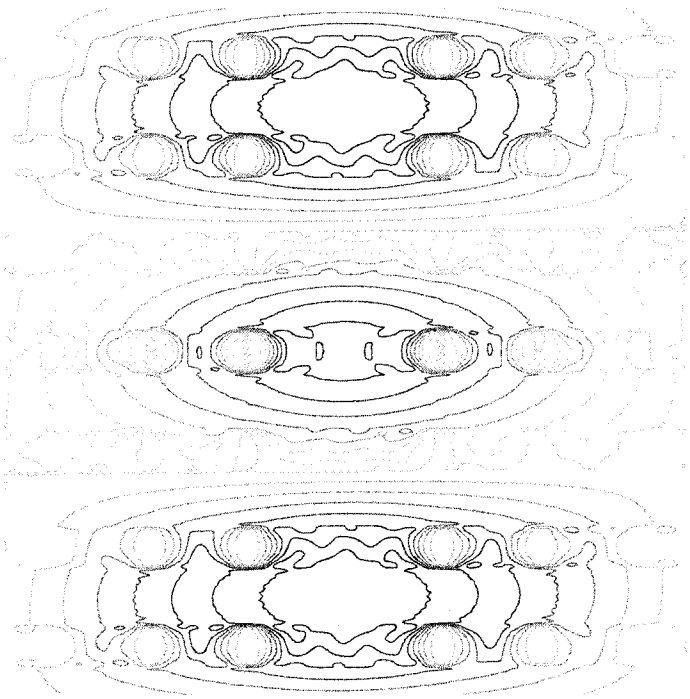

Figure 35. Mode field pattern of guided modes in an air waveguide. Modes are even symmetric along the waveguide center line, energy of the guided modes are concentrated in the waveguide and the neighboring two column rods. K_y=0.40π/a, indicating a spatial period 2.5a.

3.3.3 Interaction between defects

Point defects and linear defects are the two fundamental forms of defects and act as key components in planar devices. However, the applications will be seriously limited if they can only be used in an isolated way. The interactions between these defects are important to new device design. A linear waveguide supports modes within a continuous, width-limited band, and a point defect supports one or more separate light states. The tunneling process can transfer energy between point defects, and between point defects and linear defect. Though modes are well

Reproduced with permission of the copyright owner. Further reproduction prohibited without permission.

confined in point defects and line defects, interaction between defects affects the frequency and mode pattern of the defect mode.

(1) Two-defect microcavity

As an example, we consider a system with two point defects separated by several lattice constants and the defects are created by removing one rod. The structure or the supercell is shown in Figure 36.

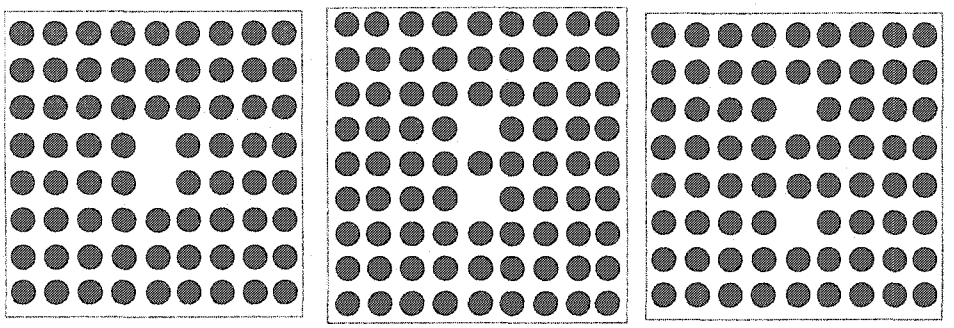

Figure 36. Microcavity with two point defects. Two defects are separated by 1a, 2a and 3a. Each structure is represented by a 9x8, 9x9 and 9x8 supercell, respectively.

The new system forms a bigger micro-cavity which supports two modes, and these two modes can be considered to be composed by the linear combination of the monopoles in one single point defect in phase or out of phase: (positive, negative), (positive, positive). They are shown in Figure 37. When the distance of the two defects is 2.0a (even), the first mode obtains destructive interference at the connection rod and the second mode obtains constructive interference at the connection. In this case, the in-phase mode (even mode) has two nodes, having a higher eigen-frequency; the out-of-phase mode (odd mode) has only one node, having lower eigen-frequency. The degeneracy is not maintained since the symmetry is destroyed in the structure. For the distance to be odd number the even mode has lower frequency and odd mode has a higher frequency.

In general, the defect mode pattern are very stable, they keep the mode pattern well even when the distance of defects is only one or two lattice constants. The defect frequency change will get smaller if the distance of defects is longer.

Reproduced with permission of the copyright owner. Further reproduction prohibited without permission.

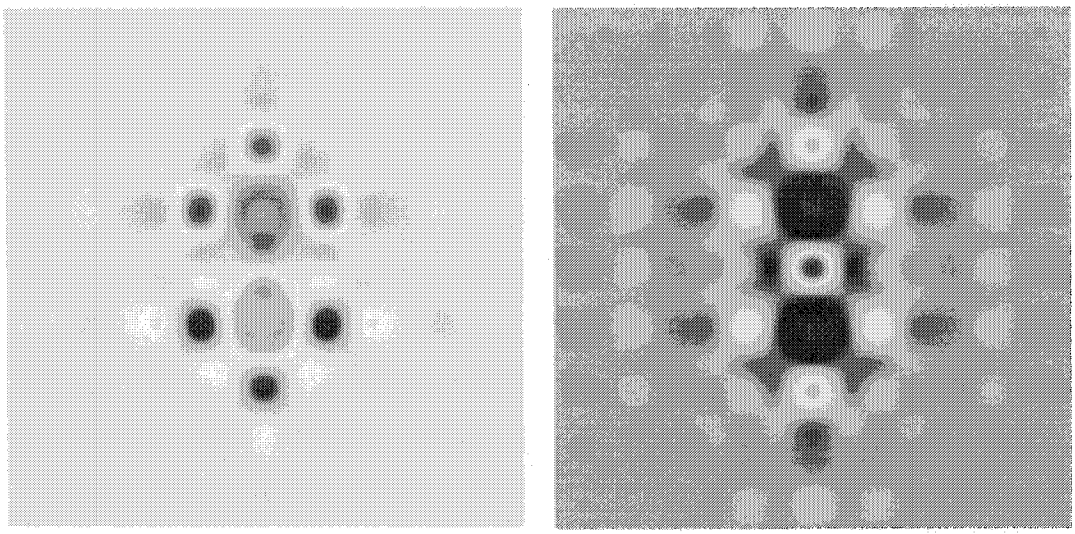

(a)

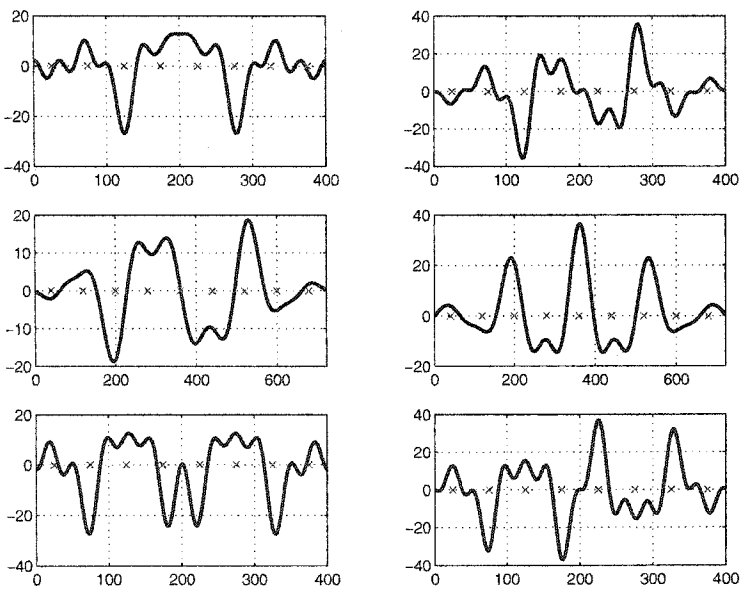

(b)

Figure 37. Interaction between two point defects. Two modes are supported and the eigen frequency for the modes split up. (a). distance=2.0a. Left: modes are out-of-phase, with lower frequency, odd symmetry; Right: modes are in-phase, with higher frequency, even symmetry. (b). The mode fields along y in the center for a distance of 1.0a, 2.0a and 3.0a. 'x' indicates the rod position.

The direct coupling between defects decreases exponentially with the distance. The frequency split is illustrated in Table 6. Also shown is the frequency shift in opposite direction and in an equal way.

Reproduced with permission of the copyright owner. Further reproduction prohibited without permission.

Table 6. Frequency split due to interaction between two point defects.

Distance between 2 point defects	Odd mode (band 81)	Offset	Even mode (band 82)	Offset
1a	0.438655	(+10.03%)	0.360643	(-9.54%)
2a	0.388139	(-2.64%)	0.408752	(+2.53%)
3a	0.405603	(+1.74%)	0.397560	(-0.28%)
4a	0.397926	(-0.19%)	0.399453	(+0.19%)
9a	0.398680	(0.00%)	0.398680	(0.00%)

In most applications, the break of the degeneracy is not good and measures should be taken to retain near degeneracy. As seen from the graph, the linear combinations show different symmetry. The out-of-phase one is odd to x and even to y, with a nodal plane along x. The in-phase one is even to both x and y, with a maximum on the plane of x. Apparently, changing on y plane will affect the frequencies of two modes in the same way. One way to raise the eigen frequency of the odd mode is to reduce the refractive index of 4 rods on the two planes (parallel to x) with maximums (minimums) on them. The effect of raising frequency for the even mode will be less since more energy is on the plane of x. The exact value of index reduction has to be found by numerical experiments.

For systems with multiple identical point defects, similar results can be obtained.

(2) CCWs: Resonant tunneling between periodic point defects

Periodic point defects can enable propagation modes through resonant tunneling energy transfer. The waveguide in Figure 34 can be considered a waveguide by periodic point defects with period=a. In Figure 38 and Figure 39, waveguides are formed with periodic point defects separated by 1 and 2 rods, which can be called as Coupled Cavity Waveguides (CCWs). These two waveguides show group velocity with opposite signs. The waveguide of negative group velocity could be of interest for some potential applications.

Compared to the waveguide in Figure 34, the defect mode only supports a narrow frequency band in the gap. One can expect the bandwidth to be even narrower provided the periodicity of the defects becomes larger. This could be a beneficial feature used for dense WDM applications by making the channel with a very narrow spectrum.

The bandwidth tuning is very flexible and efficient by the period of the defects, as shown in Figure 40. The bandwidth of the waveguide decreases exponentially while the period increases.

Reproduced with permission of the copyright owner. Further reproduction prohibited without permission.

The guided mode is shown in Figure 41, it supports a monopole guiding mode. The monopole waveguide is sensitive to the width of the waveguide. Deviation from the regular waveguide width will cause more energy in the cladding. A wider waveguide can support the dipole mode or even higher modes. And the fundamental monopole mode is lossy as shown in Figure 41.

Increasing the radius or dielectric constants of the defect rod can introduce higher mode, these modes are more confined and have higher Q values, and a more stable waveguide could be achieved. In this case, since the core area has a higher average refractive index than the cladding area, the conventional total internal reflection can happen, making it a multimode hybrid waveguide. This is shown in Figure 42, where the defective rod radius is 0.60a, and 5 modes are supported, including 2 quadrupole, one 2^{nd} monopole and two hexapoles. These modes are quite stable to the waveguide width and confine the mode energy in the defective rod.

Reproduced with permission of the copyright owner. Further reproduction prohibited without permission.

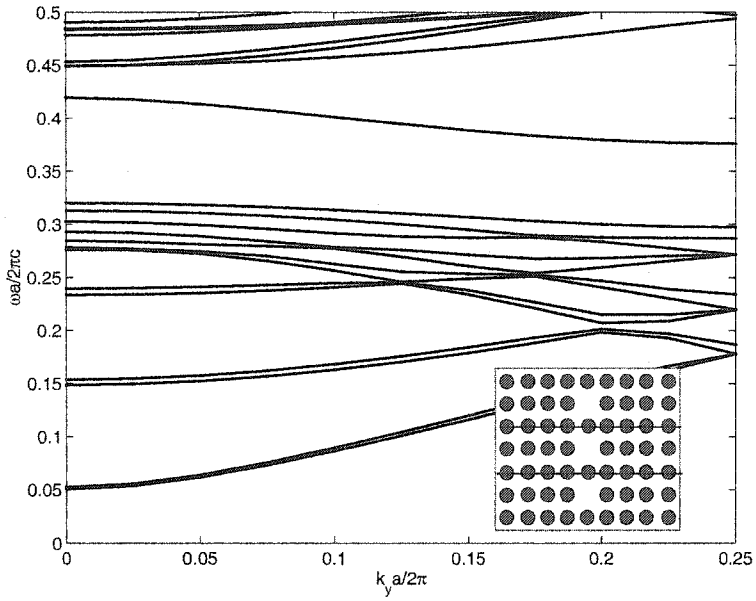

Figure 38. Waveguide formed by periodic point defects, period=2a. The inset shows the 7x2 supercell.

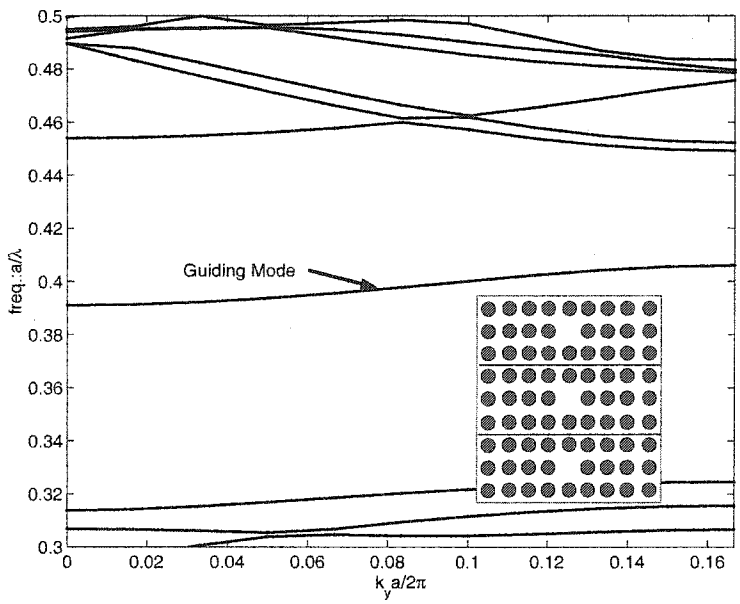

Figure 39: The band structure of a linear waveguide formed by periodic point defects, period=3a. The inset shows the 7x3 supercell.

Reproduced with permission of the copyright owner. Further reproduction prohibited without permission.

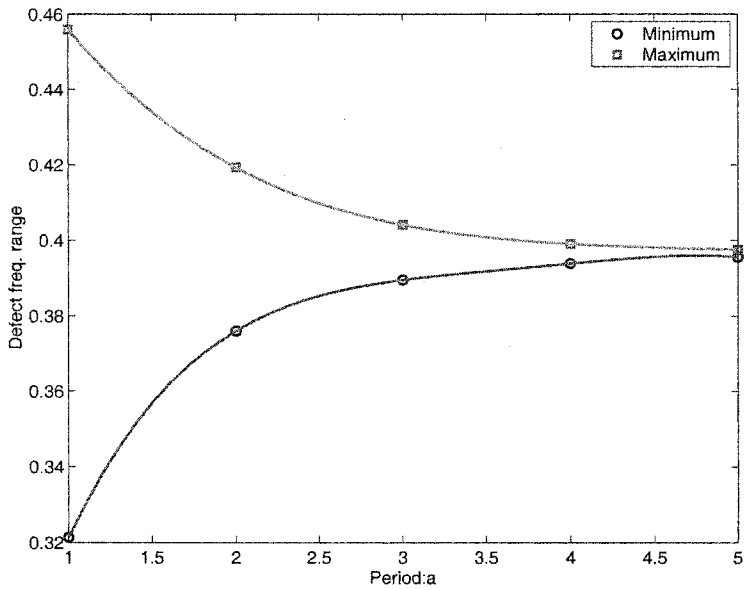

Figure 40. Bandwidth tuning using periodic point defects. The bandwidth decreases exponentially while the period increases.

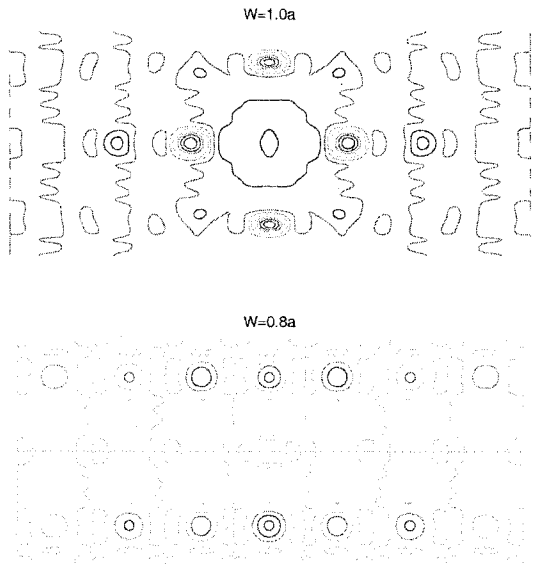

Figure 41. Monopole is sensitive to the waveguide width and becomes lossy while it deviates from the regular place.

Reproduced with permission of the copyright owner. Further reproduction prohibited without permission.

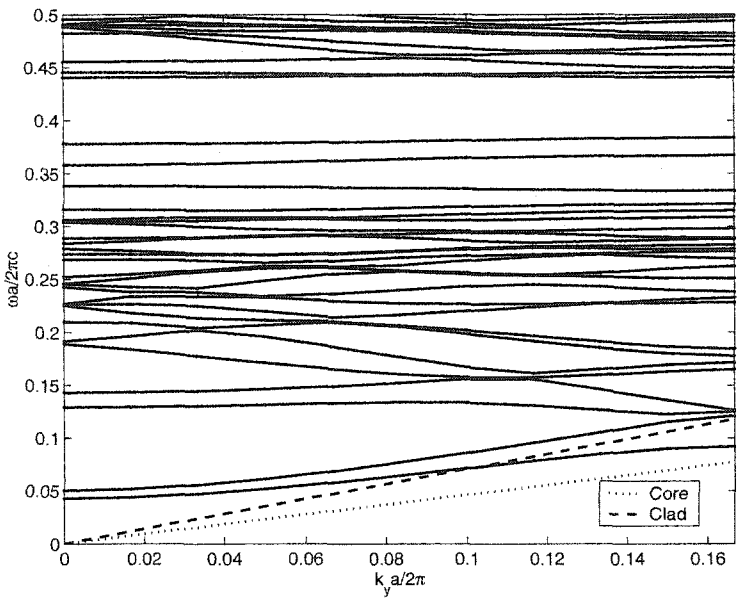

Figure 42. Waveguide by periodic increased size rods, period=3a, R=0.60a. 5 modes are supported, including two quadrupoles, one 2nd monopole and two hexpoles. One index guided mode appear in some k range.

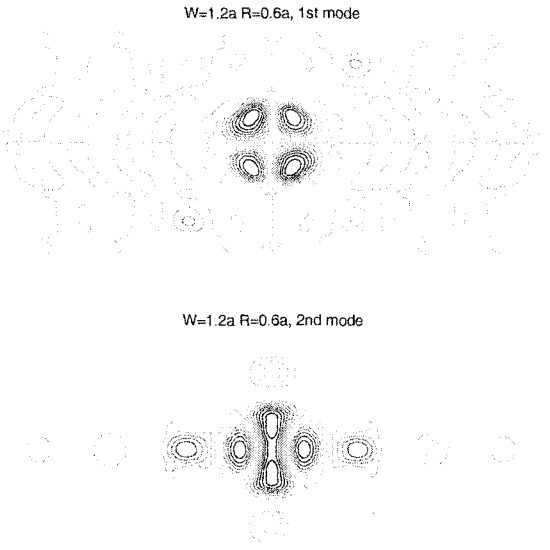

Figure 43. Higher modes supported by a hybrid waveguide are quite stable. Defect rod radius is 0.60a, the waveguide is widen by 0.20a.

Reproduced with permission of the copyright owner. Further reproduction prohibited without permission.

(3) Waveguide-microcavity interactions

Coupling between propagating modes and localized modes are of interest and crucial to many photonic crystal based devices, such as the coupler, add/drop filter. Generally, a guided mode excites localized modes and localized modes couple the energy to another guiding mode. The process is highly selective since the resonant frequency of a localized mode is very narrow. However, to make a complete transfer, careful consideration is needed for the design of these micro-cavities. The schematic graph is shown in Figure 44. Assuming guiding modes in one waveguide with multiple frequencies, those signals which have no frequency overlap with the resonant frequency will not be affected by the presence of the resonator since the coupling between them is very weak or cancelled. When their spectrum overlaps, coupling will occur. In this case, energy will transfer to the resonator, and then transfer back as reflection and transmission, also transfer to forward and backward guiding mode in the other channel.

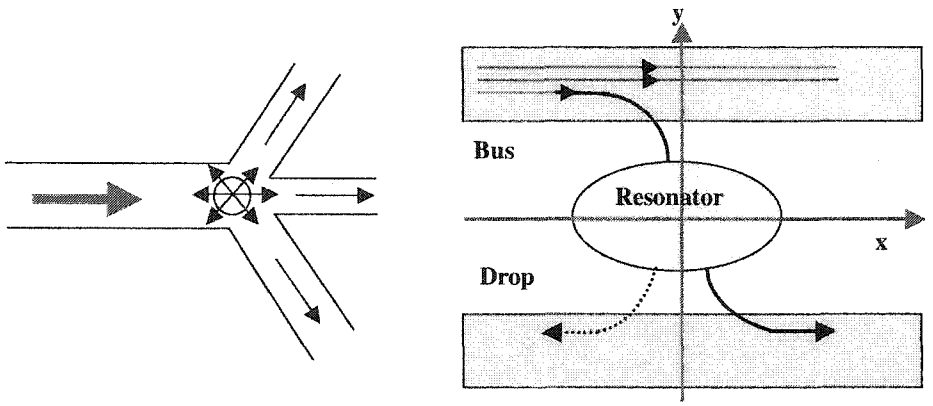

Figure 44. Schematic of a guiding mode-localized mode coupling. Left: inline point defect filters the input and split the output. Right: off-line point defect transfer energy from one channel to another channel.

As an example, a 100% backward add/drop device is to be designed using a 2D square lattice with alumina rods in air, R=0.20a. A complete band gap for TM mode in the bulk crystal exists from 0.32 to 0.45. The two waveguides are formed by removing two rows of rods and a point defect is formed by increasing the center rod to a radius of 0.70a, and the distance between the center of the cavity and the mid-line of the waveguide is 3a. This microcavity alone supports a doubly degenerate mode with hexapole mode pattern. The symmetries of these two modes are shown in Figure 45. From the figure, it is possible to achieve complete backward coupling since the reflection and transmission to the bus and forward coupling to the drop channel have different signs and may cancel.

Reproduced with permission of the copyright owner. Further reproduction prohibited without permission.

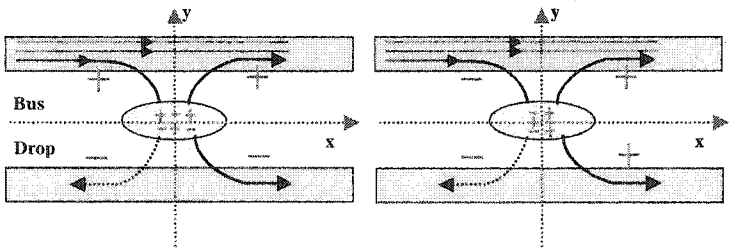

Figure 45. Different signs to the coupling of different directions due to the symmetry of the localized states. Left: even mode (to y-plane), Right: odd mode (to y-plane).

The standalone degenerate hexapole mode has a frequency of 0.39 when R=0.70a. At the same time, the cavity also supports two other modes (quadrupole and 2nd order monopole, see Figure 28), so it would be better not to make the incident signal's spectrum to overlap with theirs.

Since the two waveguides break the periodicity in y-axis, the frequencies of the two modes will split. When the distance is far, the coupling effect is small and degeneracy can maintain. If the distance is in 2-3 lattice constants, the coupling is not negligible and frequency split cannot be ignored; the spectra of the two modes will not overlap any more if the split is larger than the cavity bandwidth. The calculated band structure for the standalone cavity and cavity plus the two waveguides are shown in Figure 46. The shift is small, but still large compared to the bandwidth of the micro-cavity (For Q=10000, $\Delta\omega/\omega_0$=0.01%). The calculated value is listed in Table 7. Note that the calculated frequencies are shifted as a whole about 0.2 since the number of plane waves is not large enough (refer to Figure 12).

Since the even mode has maximum in the symmetry plane y and it has more power in the higher index region, its frequency tends to shift less than the odd one in the effect of the neighboring waveguide, which is verified in the inset in Figure 48. The degeneracy of these two hexapole modes can be forced by making their frequency difference to zero. The odd mode reaches maximum in the plane x (Figure 45), and the even mode has a nodal plane along it, so along this plane, if we increase the dielectric constants of the two sided rods as in Figure 47, both frequencies tend to shift downward, but the odd mode will be affected more than the even mode. The frequency evolution of these two modes by changing the two sided rods along x plane is shown in Figure 48.

Reproduced with permission of the copyright owner. Further reproduction prohibited without permission.

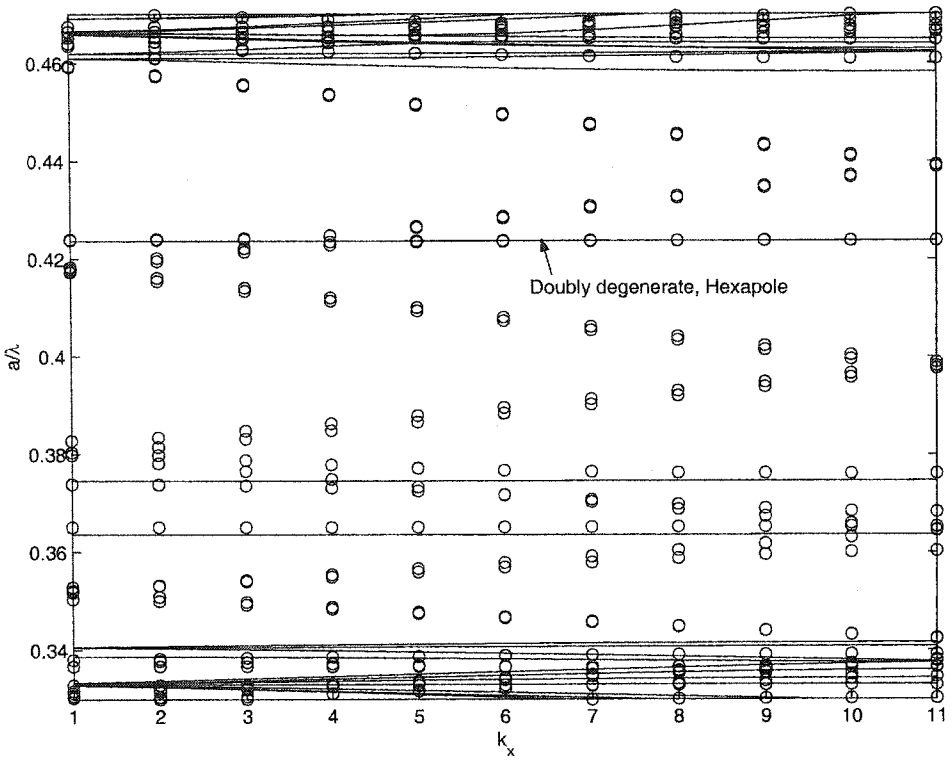

Figure 46. The frequency changes of point defect due to neighboring waveguides. The solid lines are for point defect only, the circles are for point defect + waveguides.

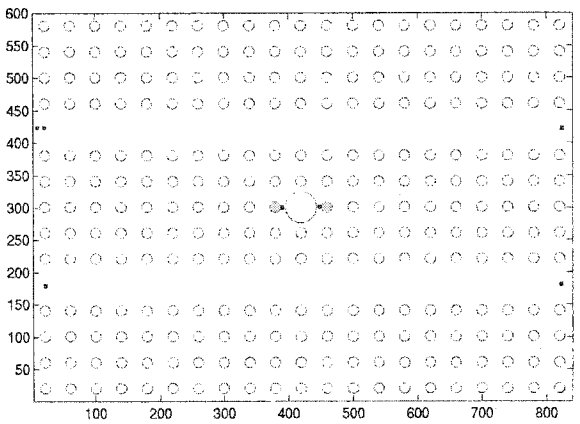

Figure 47. 100% add/drop filter: backward coupling through a doubly degenerate point defect (R=0.70a) with hexapole modes. The degeneracy is forced by increasing the neighboring two rods (gray) to 9.49.

Reproduced with permission of the copyright owner. Further reproduction prohibited without permission.

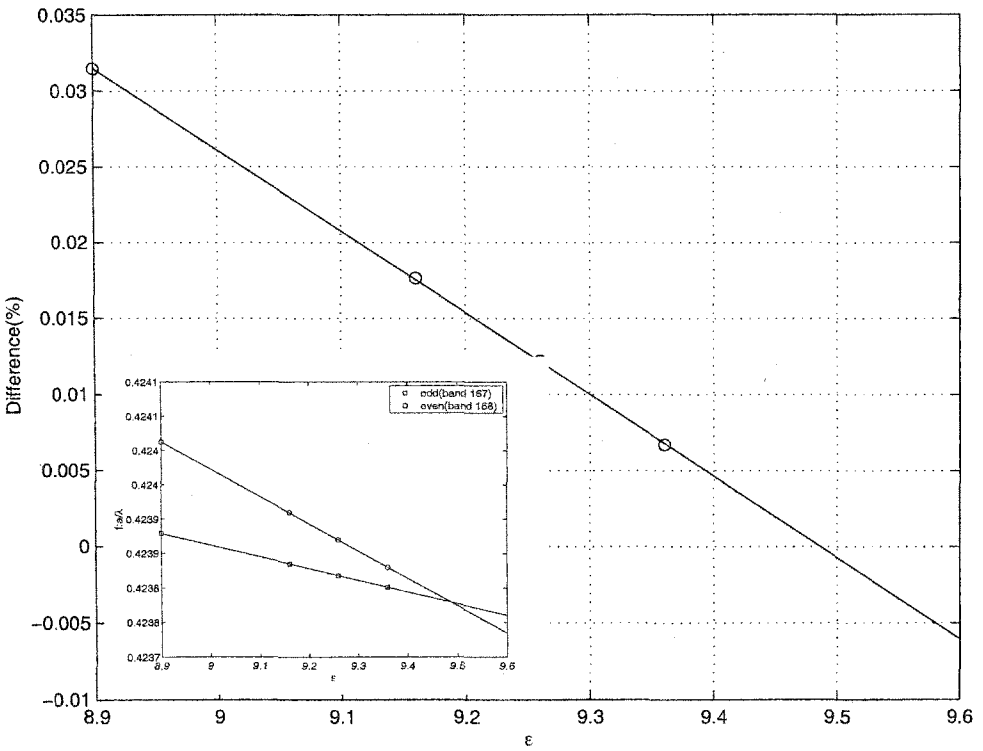

Figure 48. Finding the dielectric constants of the two sided rods to force degeneracy. The difference is calculated as the ratio of frequency difference to the mid-frequency. From the curve, when dielectric constants of the two sided rods are 9.4868, degeneracy is forced. The inset shows the frequency tuning of the two modes.

Table 7. Frequency shift of point defect mode due to the neighboring waveguides. 13x13 supercell used and 841 plane waves used in calculation.

Point defect alone	Point defect + two waveguides	Freq. shift ($\Delta\omega/\omega_0$)
0.42366337216051(band 175)	0.42387900865288(band 167)	0.05%
0.42366337216051(band 176)	0.42401230780984(band 168)	0.08%

3.4 Discussion

Much effort is placed on the understanding of these two dimensional photonic crystal structures. The band gap formation depends on many parameters and their interplay is very complex. A general understanding of the interplay can help the design of structures for different applications. The band gap changes the DOS dramatically and could be of interest to quantum

Reproduced with permission of the copyright owner. Further reproduction prohibited without permission.

effect. Eigen modes are investigated and these modes are not always the field distribution in the crystal by an incident of plane wave with a specific k-vector, although plane wave incidence does excite some of them. Coupling by excitation source is always important for practical purpose and the symmetry of the mode and source should be carefully reviewed to ensure nonzero energy coupling.

Defective crystals are the way by which people use to control light. Microcavities formed by point defects can localize light in their neighboring regions and could be high Q filters with very narrow bandwidths. Interactions between defects are complicated due to the two dimensional property of the field, so there is no analytical form for these wave couplings and phase matching condition are hard to find. Resonant tunneling process plays an important role to reach highly efficient energy transfer between different states. When resonant condition is satisfied, transitions can occur from one localized state to another, or from localized states to propagation states.

Many new planar devices, based on photonic crystals, can be designed with high performance, such as waveguide bendings, beam-splitters, couplers, and waveguide crossings.

Rigid theoretical analysis of the coupling between localized state and propagation state is present in reference [60] and not repeated here. Numerical calculations can disclose their interaction, but cannot answer why. A clear understanding of the coupling mechanism requires advanced theory and is to be conducted in future work.

Reproduced with permission of the copyright owner. Further reproduction prohibited without permission.

CHAPTER IV

PHOTONIC CRYSTAL FIBER

Photonic crystal fiber (PCF) is attracting much attention due to its special guiding properties, such as the endless-single mode in a broad wavelength region [43] and possible guidance in air due to photonic band gap effects [44]. There are two different guiding mechanisms: the air-guiding PCF requires a defect level in the bandgap, which is a result of the coherent multi-scattering from the periodic cladding; however, the index-guiding PCF's require no band gap effect, the guiding is a result of the conventional total internal reflection. In general, the PBG guiding fiber needs the existence of a band gap, thus proper periodicity is required; index guiding PCF can have periodic or quasi-periodic claddings.

The plane wave method suitable for finding the band structure of a PBG material is not good for analysis of index-guiding PCFs, since it solves the eigen-frequencies at a given wave vector k. However, in fiber analysis, we need to know the propagation constant β at a given wavelength. In addition, the material dispersion is hard to be included in the plane wave method as discussed in Chapter II.

Several methods have been proposed to model PCF. The effective index model [43] [44, 85] approximates the PCF to a step index fiber with a wavelength-dependent cladding using scalar wave equations. This method is known to be unable to predict the accurate mode pattern, propagation constants and dispersion properties. One other method uses Hermite-Gaussian series to approximate the localized fiber mode [86]. This method needs to evaluate several integrations, which are only easily implemented when analytical integration forms exist. The biorthonormal-basis modal method [87] is full-vectorial, and this can be simplified using the plane-wave-like method [88]. The plane-wave-like method is much easier to implement based on the plane wave method. In this chapter, we use the similar full-vector approach for the analysis of PCFs with different structures.

4.1 Analysis Method

Since the z-direction is index-invariant, the separation of the H and E field into transverse and longitudinal components is most convenient. The transverse field component obeys the following vector wave equation:

$$\left(\nabla_t^2 + k_0^2\varepsilon\right)E_t + \nabla_t\left(E_t \cdot \nabla_t \ln\varepsilon\right) = \beta^2 E_t \tag{4.1}$$

$$\left(\nabla_t^2 + k_0^2\varepsilon\right)H_t + \nabla_t \ln\varepsilon \times \left(\nabla_t \times H_t\right) = \beta^2 H_t \tag{4.2}$$

Since the results for H are shown in Ref. [88], so they are not repeated here.

Reproduced with permission of the copyright owner. Further reproduction prohibited without permission.

As in plane wave method, we apply the periodic boundary conditions to it, assuming the dielectric constant is a periodic function of the space and so it can be expanded using Fourier series [88]:

$$\varepsilon(r)=\sum_G \varepsilon_G e^{i\vec{G}\cdot\vec{r}},\ \ln\varepsilon(r)=\sum_G \kappa_G e^{i\vec{G}\cdot\vec{r}} \tag{4.3}$$

where $\vec{G}$ is the grid vectors in the reciprocal space.

The transverse E field can also be expanded using Fourier series:

$$E_t=\sum_G\left\{E(G,x)e^{i\vec{G}\cdot\vec{r}}\hat{x}+E(G,y)e^{i\vec{G}\cdot\vec{r}}\hat{y}\right\} \tag{4.4}$$

Plug them into the wave equation (4.1) will produce a standard eigen-value problem:

$$\begin{aligned}&-|G|^2\left(E_{Gx}\hat{x}+E_{Gy}\hat{y}\right)+k_0^2\sum_{G'}\varepsilon_{G-G'}\left(E_{G'x}\hat{x}+E_{G'y}\hat{y}\right)-\\&\sum_{G'}\kappa_{\vec{G}-\vec{G}'}\left[(G_x-G'_x)E_{G'x}+(G_y-G'_y)E_{G'y}\right](G_x\hat{x}+G_y\hat{y})\\&=\beta^2\left(E_{Gx}\hat{x}+E_{Gy}\hat{y}\right)\end{aligned} \tag{4.5}$$

In matrix form, it can be written as:

$$\begin{bmatrix}M_1 & M_2\\ M_3 & M_4\end{bmatrix}\begin{bmatrix}E(G',x)\\ E(G',y)\end{bmatrix}=\beta^2\begin{bmatrix}E(G,x)\\ E(G,y)\end{bmatrix}$$

and the matrices are (see Appendex II):

$$M_1=-|G^2|I+k_0^2\varepsilon(\vec{G}-\vec{G}')-\kappa(\vec{G}-\vec{G}')(G_x-G'_x)G'_x \tag{4.6a}$$

$$M_2=-\kappa(G-G')(G_y-G'_y)G_x \tag{4.6b}$$

$$M_3=-\kappa(G-G')(G_x-G'_x)G_y \tag{4.6c}$$

$$M_4=-|G^2|I+k_0^2\varepsilon(\vec{G}-\vec{G}')-\kappa(\vec{G}-\vec{G}')(G_y-G'_y)G'_y \tag{4.6d}$$

where the subscripts x, y mean the x- and y-component.

For H we also show the matrices here (see Appendex III):

$$M_1=-|G|^2I+k_0^2\varepsilon(G-G')+\kappa(G-G')(G_y-G'_y)G'_y \tag{4.7a}$$

$$M_2=-\kappa(G-G')(G_y-G'_y)G'_x \tag{4.7b}$$

$$M_3=-\kappa(G-G')(G_x-G'_x)G'_y \tag{4.7c}$$

$$M_4=-|G|^2I+k_0^2\varepsilon(G-G')+\kappa(G-G')(G_x-G'_x)G'_x \tag{4.7d}$$

Reproduced with permission of the copyright owner. Further reproduction prohibited without permission.

Our calculation shows that in many cases the eigen equation for H can be simplified to reduce the heavy computation involved. The coupled terms in (4.7b-c) can be neglected and the computation is half reduced, however, there is no strict mathematical proof.

4.2 INDEX-GUIDING PCFS

4.2.1 PCF with air holes arranged in triangular lattice

Small air holes are periodically arranged in silica glass in a triangular lattice, the center air hole is removed and the solid acts as the fiber core. This PCF has been studied in detail by many authors. The main results are re-calculated here using our method. The 5X5 supercell is illustrated in Figure 49.

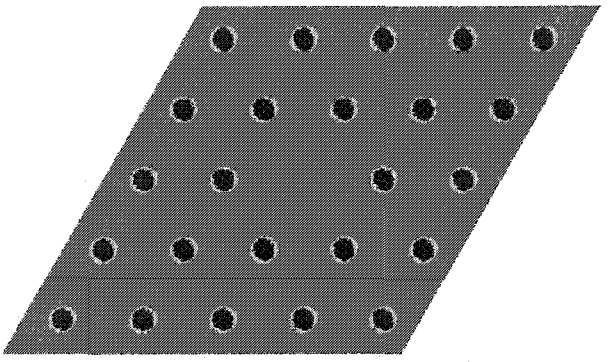

Figure 49. PCF with air holes in a triangular lattice. A 5x5 supercell is used to simulate the fiber.

(1) The effective index of the periodic cladding

The effective index of the cladding is defined as the maximum mode index of the guided mode in the cladding. When the material dispersion is not included, the effective index of the cladding can be calculated either using plane wave method or the method above. Since $\omega^2 = c^2\left(k_x^2 + k_y^2 + k_z^2\right)$, for k_z to be maximum and eigen-frequency minimum, k_x=k_y=0. This hints the eigen frequency with k=(0,0,k_z) has the largest β. Given a β, we can easily find the eigen-frequency using plane wave method. This can also be easily obtained using the above method. The result is shown in Figure 50.

As seen in the graph, the effective cladding index approaches the core index in the short wavelength region, and approaches the average index in long wavelength region (see Table 8). The effective V of this fiber is almost constant in short wavelength region (when λ/a>3). When the wavelength is comparable to the periodicity, the cladding can be considered as a strongly

Reproduced with permission of the copyright owner. Further reproduction prohibited without permission.

wavelength dependent medium. This kind of periodic structure brings at least two features: possible guidance of a single mode in all wavelength regions; the periodic structure can bring extra control to the dispersion of the fiber.

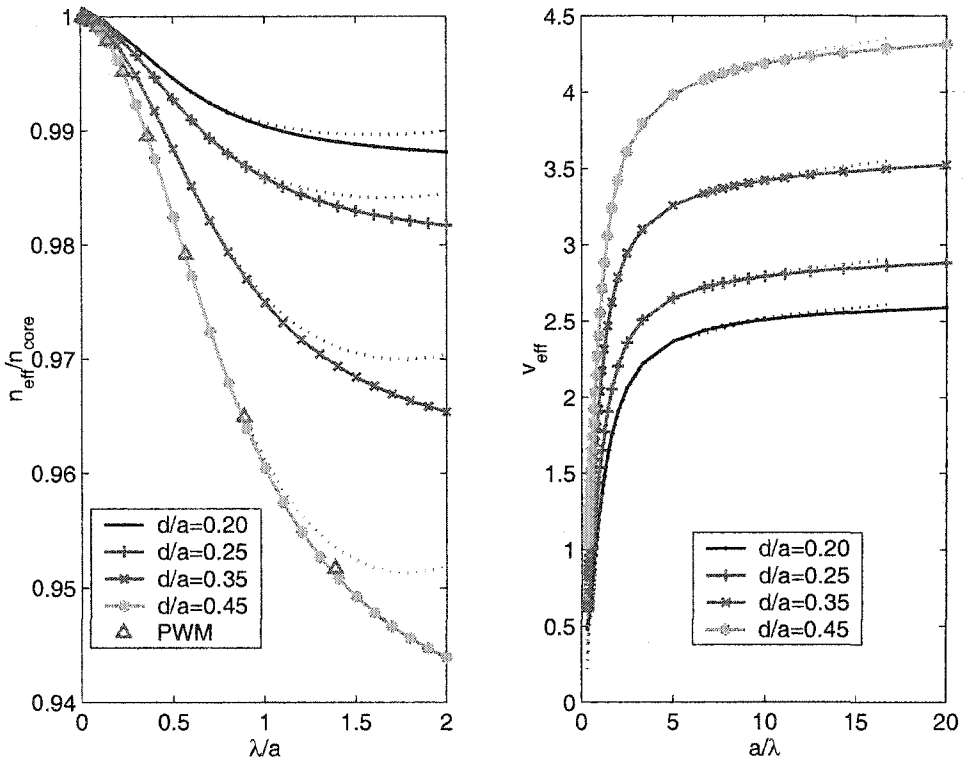

Figure 50. Effective index of the periodic cladding and V in a triangular 2D PBG PCF with air holes. The dotted line represents the case with material dispersion included.

Table 8. Effective index of cladding at long wavelength region. $n_{av1} = n_b + f(n_a - n_b)$ and $n_{av2} = \sqrt{\varepsilon_b + f(\varepsilon_a - \varepsilon_b)}$.

Air hole radius		Triangular PCF			Tube PCF			
	f	n_{av1}	n_{av2}	n_{eff} (λ=22a)	f	n_{av1}	n_{av2}	n_{eff} (λ=22a)
R=0	0	1.4600	1.4600	1.4600	9.31%	1.4235	1.4172	1.4143
R=0.05a	0.91%	1.4565	1.4558	1.4566	10.22%	1.4199	1.4130	1.4112
R=0.10a	3.63%	1.4459	1.4433	1.4433	12.94%	1.4090	1.4005	1.3956
R=0.15a	8.16%	1.4280	1.4225	1.4175	17.47%	1.3906	1.3796	1.3744
R=0.20a	14.51%	1.4026	1.3933	1.3864	23.82%	1.3646	1.3504	1.3424

Reproduced with permission of the copyright owner. Further reproduction prohibited without permission.

(2) Modes in triangular PCFs

The effective index of the fundamental mode and first several higher order modes are illustrated in Figure 51. The parameter for the fiber is a=2.3μm, air hole radius R=0.3μm. This fiber is single mode in all wavelength regions.

The mode pattern of the fundamental mode at 0.6328μm is shown in Figure 52. Mode 1 and 2, mode 3 and 4, are degenerate. The mode is well confined by the air holes, and the size of the mode field is roughly determined by the first ring of air holes.

When the air hole size increases, higher modes begin to propagate. Figure 53 shows the mode index for R=0.6μm and the lattice constant a=2.3μm. The two higher modes are almost degenerated except at the long wavelength region. Thus, this kind of fiber will be single mode for a broad range, or multimode for a broad range, depending on the air filling ratio.

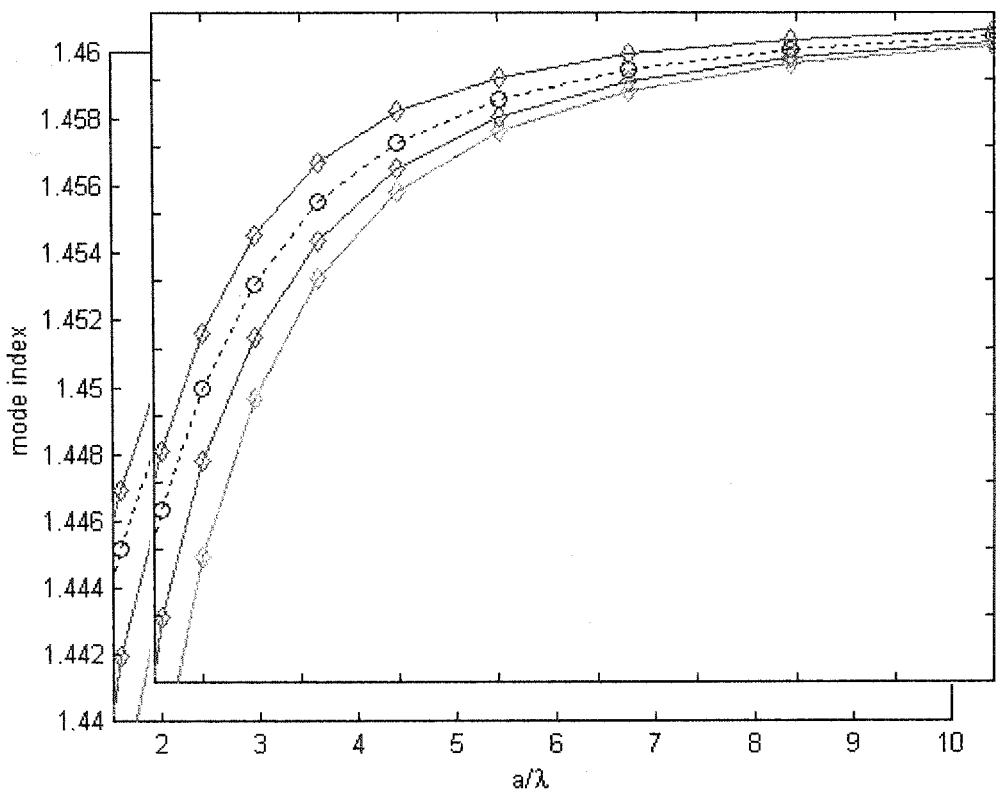

Figure 51. Endless single mode PCF: a=2.3μm, air hole radius R=0.3μm, the dashed line represents the effective index of cladding. It is all single-mode throughout this wavelength region. This result is published in Ref. [87] and is re-calculated here.

Reproduced with permission of the copyright owner. Further reproduction prohibited without permission.

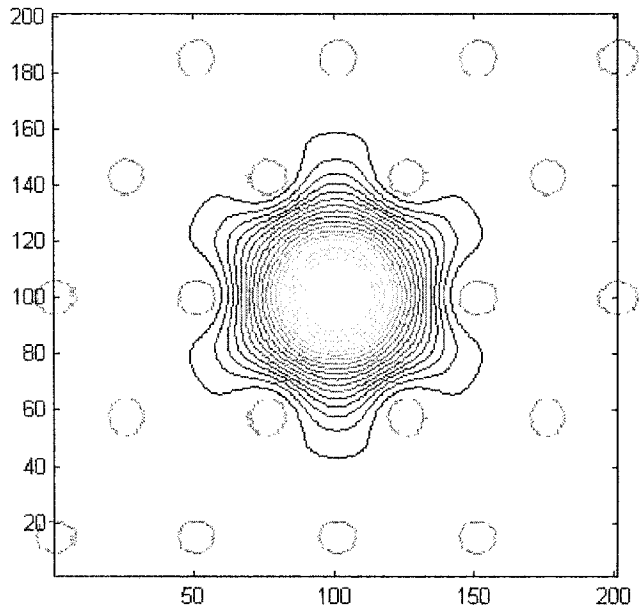

Figure 52. Fundamental mode at λ=0.6328μm, the lattice constant is a=2.3μm, air hole radius R=0.3μm. This result is published in Ref. [87] and is re-calculated here.

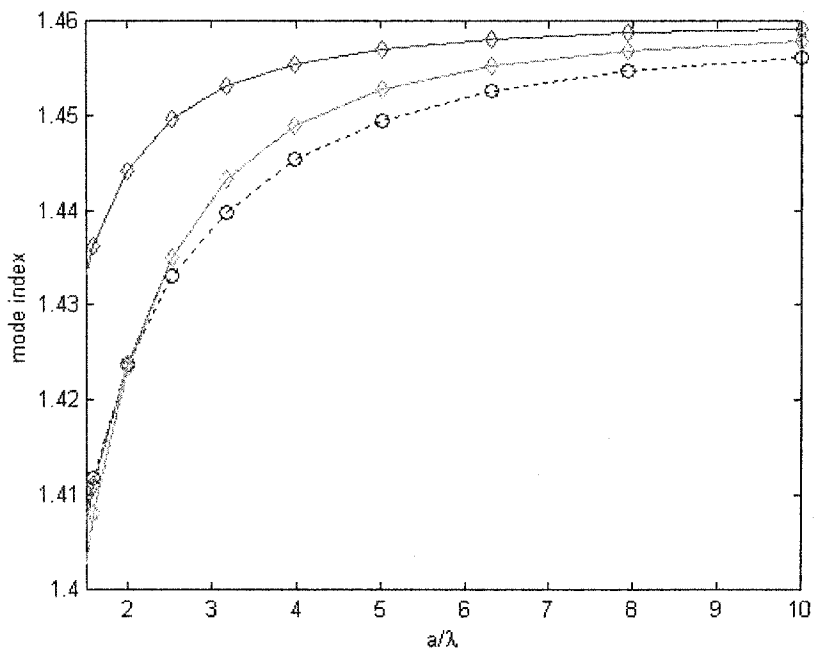

Figure 53. Effective mode index of the fundamental mode and higher order modes, R=0.6μm, a=2.3μm. Note the second and the third mode are almost degenerate. This result is published in Ref. [87] and is re-calculated here.

Reproduced with permission of the copyright owner. Further reproduction prohibited without permission.

(3) Group velocity dispersion property

Group velocity dispersion is an important guiding property. It can be approximated using the sum of the material dispersion and waveguide dispersion, though there exists some interplay between the material dispersion and waveguide dispersion. In Figure 54, we showed the material dispersion and the waveguide dispersion for PCF's with different air hole radius. The waveguide dispersion has one minimum and one maximum. When the air hole or filling ratio is larger, waveguide dispersion expands along both the D and λ axis. It is possible to get PCF's with special dispersion by tailoring the waveguide dispersion. As is seen it is possible to get a flat dispersion in a broad range when d/a=0.3.

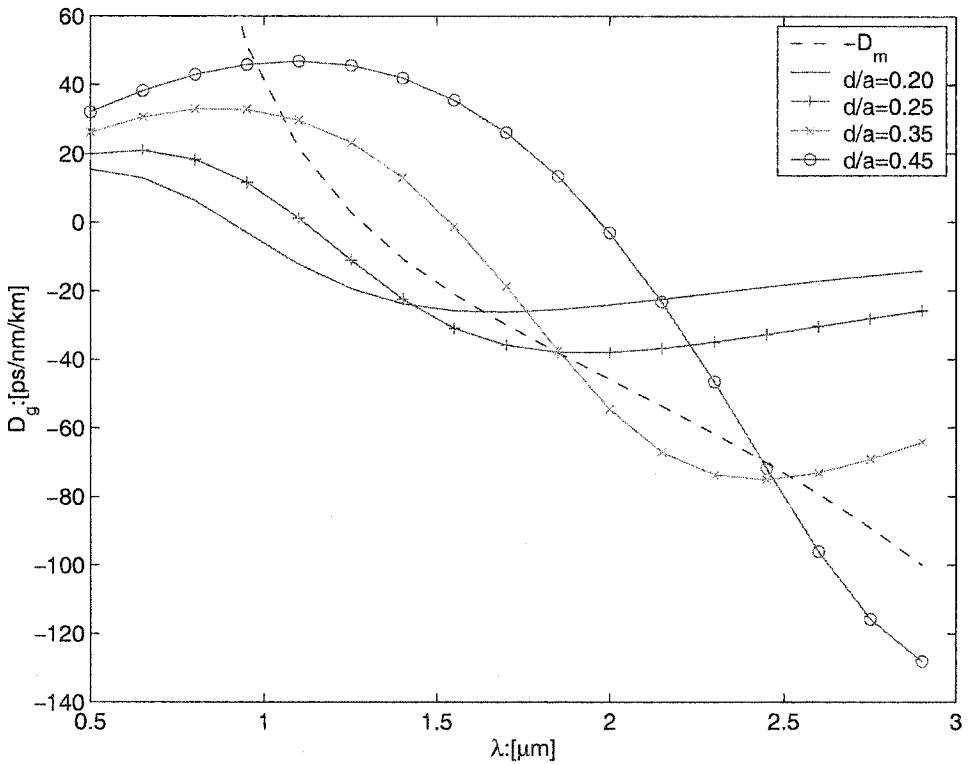

Figure 54: Group velocity dispersion of a triangular photonic crystal fiber. The lattice constant is a=2.3μm.

4.2.2 PCF with capillary tube

Though PCF with air holes arranged in a triangular lattice in glass is analyzed by many researchers, PCF with capillary tube is much less studied so far. This structure has fixed interstitial air holes (~9.3%), which affects the guiding property largely. The air-guiding property of this PCF was analyzed by Cregan et al [89], and its index-guiding property was analyzed by

Reproduced with permission of the copyright owner. Further reproduction prohibited without permission.

Ghosh et al[90]. Ghosh obtained the effective index and mode cutoff of this kind of PCF using integrated finite-difference method without considering material dispersion.

A 5x5 supercell and 823 closest grid vectors in the reciprocal space are used throughout the calculation, as is shown in Figure 55. To ensure the same accuracy, a same sized supercell without the center defect is used when calculating the cladding property.

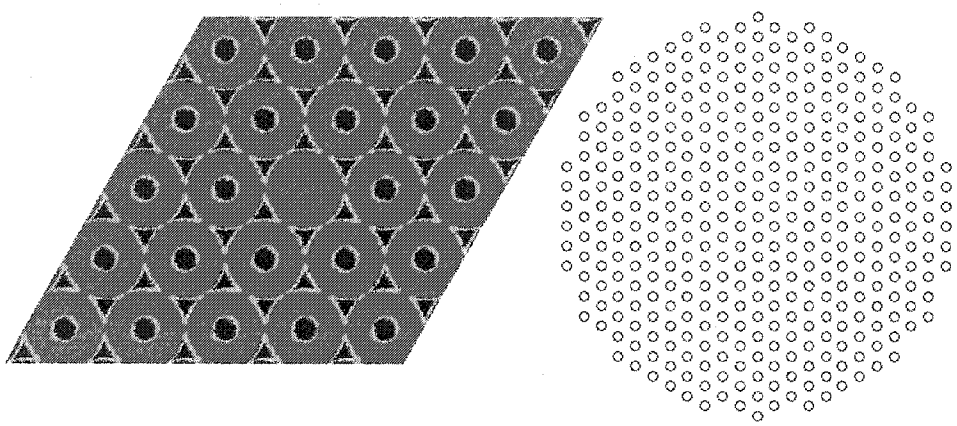

Figure 55. The PCF with capillary tubes. Left: a 5x5 supercell used in our calculation. The center air hole is removed. Right: the first 367 grid points used in the calculations.

For a single unit cell, the analytical Fourier transform is expressed in Bessel function:

$$\varepsilon(G) = 2(\varepsilon_a - \varepsilon_b)\left[f_b \frac{J_1(GR_b)}{GR_b} - f_a \frac{J_1(GR_a)}{GR_a} \right] \tag{4.8}$$

and

$$\kappa(G) = 2(\ln \varepsilon_a - \ln \varepsilon_b)\left[f_b \frac{J_1(GR_b)}{GR_b} - f_a \frac{J_1(GR_a)}{GR_a} \right] \tag{4.9}$$

with $f_b = \pi R_b^2 / A_c$, $f_a = \pi R_a^2 / A_c$, where R_a is the inner radius of the air hole, R_b=0.5a, a is the lattice constant, A_c is the area of the unit cell. The supercell's Fourier transform can be formed using shift property [65] and the supercell in Figure 55 is produced by inverse FFT.

(1) Material dispersion

Material dispersion should be taken into account when a real fiber is considered. Sellmier's formula can accurately describe the refractive index of fused silica glass from about 200nm-3μm, and we are only interested in this region. Three items are used in the Sellmier's formula [11]:

$$n^2 = 1 + \sum_i \frac{A_i \lambda^2}{\lambda^2 - \lambda_i^2} \tag{4.10}$$

with A_i=[0.691116 0.399166,0.890423], λ_i=[0.068227,0.116460,9.993707].

Reproduced with permission of the copyright owner. Further reproduction prohibited without permission.

(2) Effective index of the PCF cladding and V

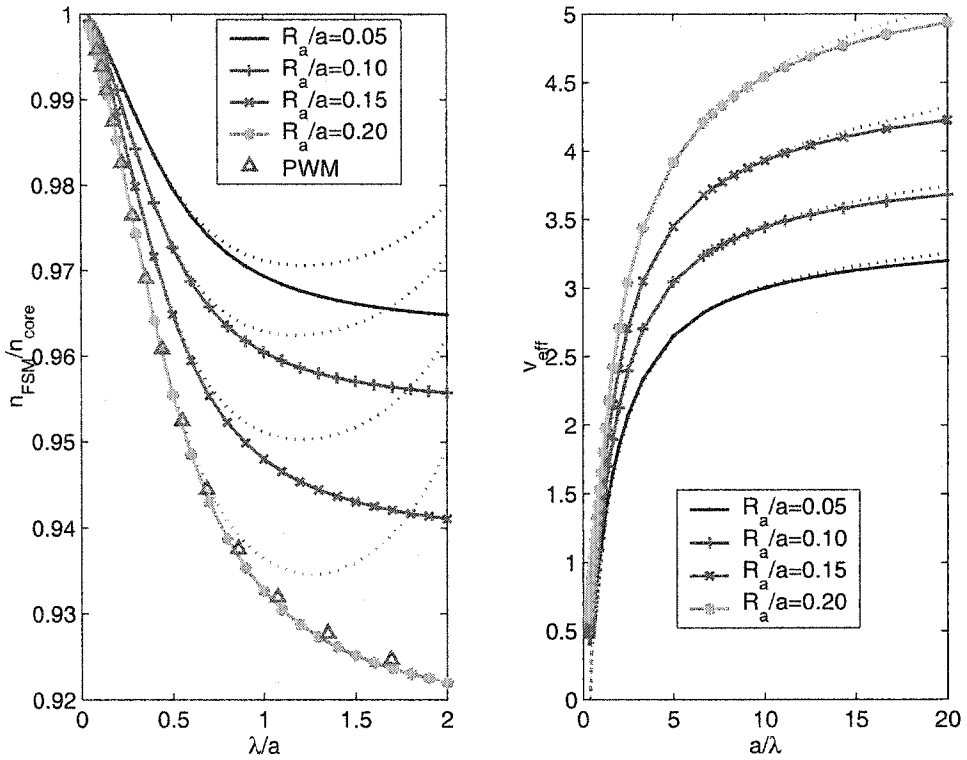

Figure 56. V and effective index of the cladding. Left: V vs a/λ. Right: n_{cl}/n_{co} vs a/λ.

When material dispersion is considered, the effective index of the periodic cladding and the normalized frequency V ($k_0 r_{co}\sqrt{n_{co}^2 - n_{cl}^2}$) is shown in Figure 56, where the radius of the core r_{co} is defined as *a*/2. The cladding shows similar property as the triangular PCF. However, there is a important difference between the triangular PCF and the tube PCF. The effective index of the cladding changes faster than the triangular one. This is reasonable since the interstitial air holes actually reduce the periodicity into about *a*/2.

Reproduced with permission of the copyright owner. Further reproduction prohibited without permission.

(3) Mode pattern of the first several modes

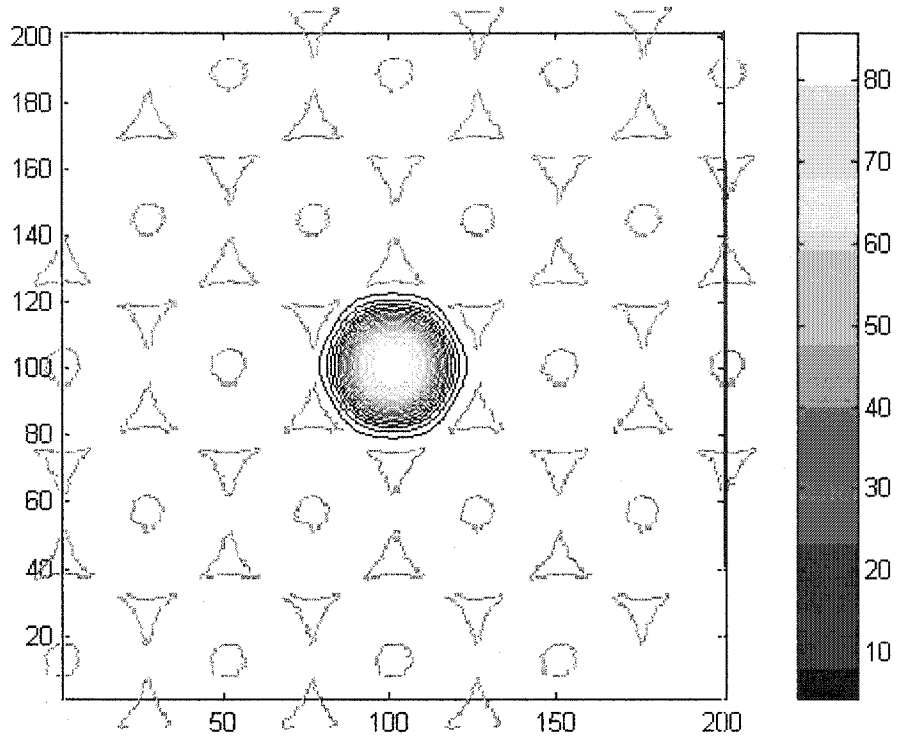

Figure 57. Transverse E field intensity of the x-polarized fundamental mode, R_a=0.10a, λ=0.2a, index of silica glass is assumed to be 1.46.

The fundamental mode is shown in Figure 57. We note that this fiber has a well-defined core-cladding boundary, unlike the PCF with no interstitial holes. The mode is tightly confined by the first ring composed of the interstitial triangular-like air holes, and the pattern is very circular, close to the mode patterns in conventional circular optical fiber. This mode pattern provides advantages in mode matching between the PCF and step-index single mode fiber.

The mode pattern of higher order modes is shown in Figure 59. The 2nd and 3rd modes are nearly degenerate, as is shown in Figure 58.

Reproduced with permission of the copyright owner. Further reproduction prohibited without permission.

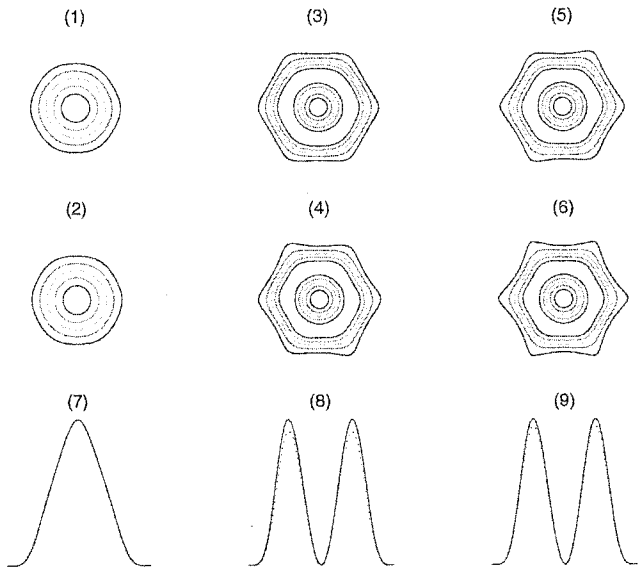

Figure 58. Transverse mode E-field intensity pattern of a capillary tube PCF with $R_a/a=0.15$, $\lambda=0.2a$. (1) to (6) represent mode 1-6.

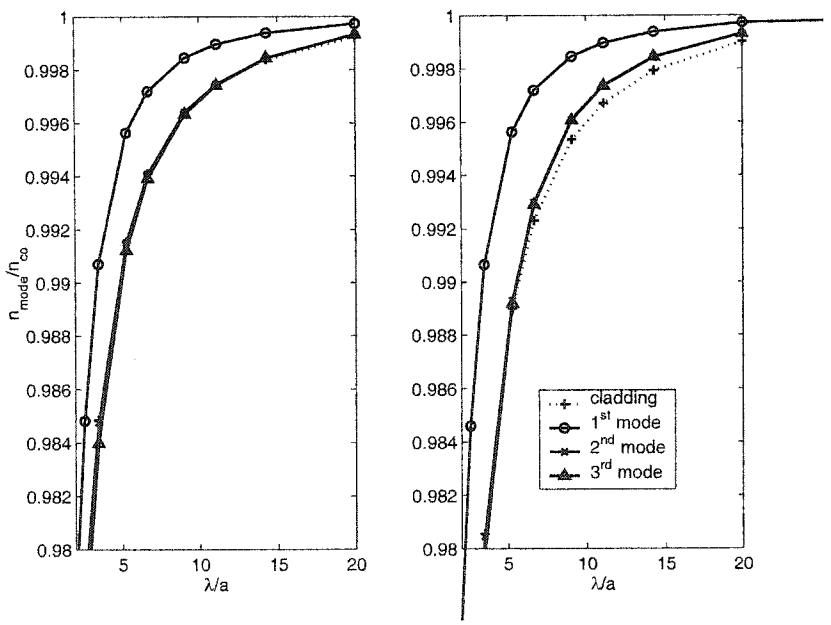

Figure 59. Mode index of the first several modes (y-polarization only). Left: $R_a=0.10a$, $a=3.0\mu m$, single mode supported in most wavelength region. Right: $R_a=0.15a$, $a=3.0\mu m$. Three modes are supported in most wavelength region.

Reproduced with permission of the copyright owner. Further reproduction prohibited without permission.

(4) Dispersion properties

a) V-b curve

Figure 60 shows the V-*b* curve for this capillary tube PCF with different air hole sizes, *b* is the normalized propagation constants, which is defined as: $b = \frac{n_{\text{mod}}^2 - n_{cl}^2}{n_{co}^2 - n_{cl}^2}$. Among these, R_a=0.50a is a conventional step-index fiber, and is shown in the graph as the dotted lines, which agree well with the analytical results found in any fiber optics books. The graph shows more clearly the cutoff V-value of the 2nd mode is not 2.405 any more. In addition, the V-b curves for PCF with different air hole size are different, which was first pointed out in [90]. However, the V-b curve remains the same if R_a/a remains the same, which keeps the significance of V in such fibers. According to the graph, the cutoff V-value of the 2nd order mode is: R_a=0.10a, V_c=3.8; R_a=0.15a, V_c=3.5; R_a=0.20a, V_c=3.0; R_a=0.50a, V_c=2.4. For R_a=0.05a, in the wavelength region (200nm-3000nm), it is all single mode.

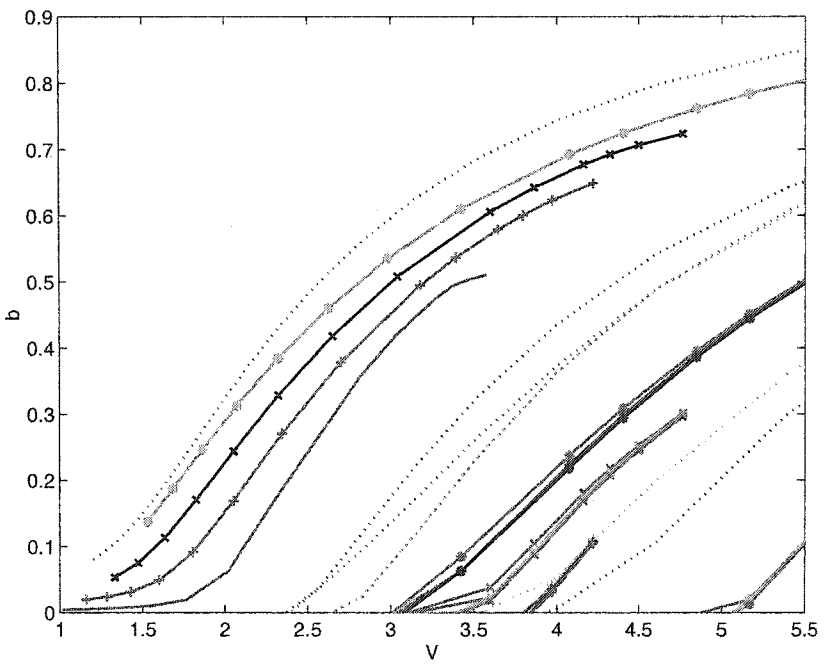

Figure 60. V-b curve of a capillary tube PCF. Solid lines are for R_a=0.05a; lines with '+' are for R_a=0.10a; lines with 'x' are for R_a=0.15a; Lines with '*' are for R_a=0.20a; dotted lines are for R_a=0.50a, this is a conventional step-index circular fiber with air cladding. Note all a=3μm and only the first 10 modes are recorded.

Reproduced with permission of the copyright owner. Further reproduction prohibited without permission.

b) Group velocity dispersion

The group velocity dispersion can be calculated using the following equation: $D_T = -\frac{\lambda}{c}\frac{d^2 n_{mod}}{d\lambda^2}$, where n_{mod} is the mode index. The 2nd order derivative is calculated using finite difference: $D_T = -\frac{\lambda}{c}\frac{n(\lambda+\Delta)-2n(\lambda)+n(\lambda-\Delta)}{\Delta^2}$, where the subscript *mod* is omitted for brevity. The dispersion calculation is sensitive to the errors accumulated in the calculation of n_{mod}. A wavelength step $\Delta = 0.005\lambda$ is used in the calculation. The dispersions for PCFs with different air hole sizes are illustrated in Figure 61.

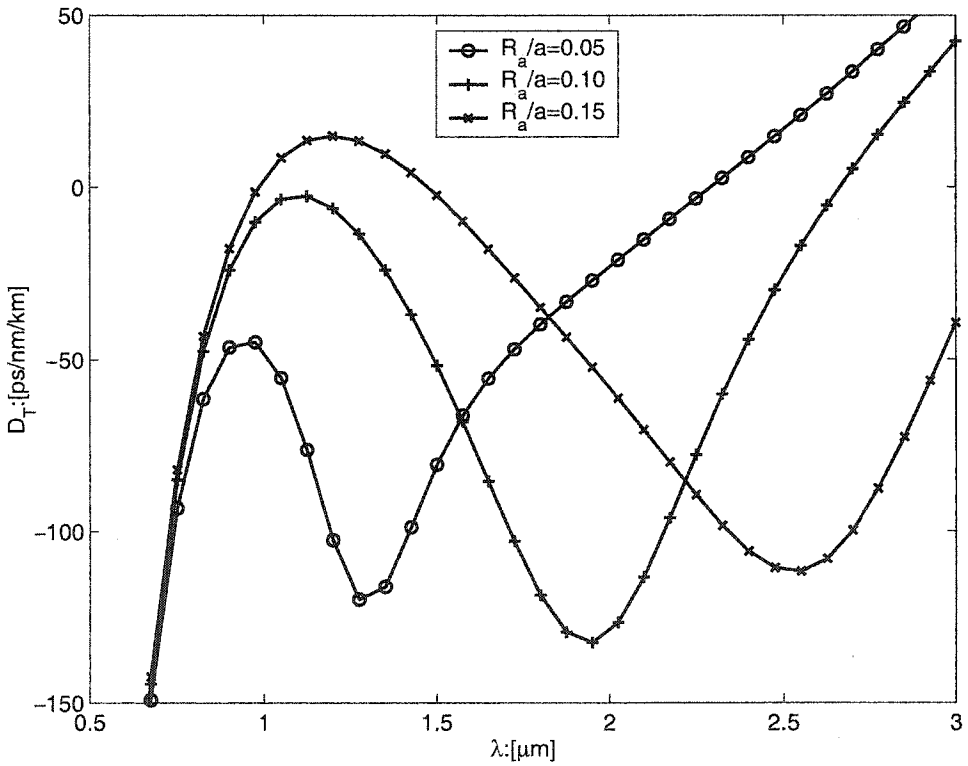

Figure 61. Dispersion property of the fundamental mode with different air hole sizes, the lattice constant=3.0μm.

As seen in a broad wavelength region, the GVD has a negative slope. When the air-filling fraction is larger, the region becomes broader and shifts to the longer wavelength, the slope changes not much. The PCF with capillary tubes shows different dispersion properties from the PCF with no interstitial triangular-like air holes, whose negative slope range is much smaller and flatter. This property may find applications acting as a dispersion-shifted fiber with a negative

Reproduced with permission of the copyright owner. Further reproduction prohibited without permission.

slope to cancel the dispersion of those conventional dispersion shift fibers since they usually have positive dispersion slopes. This also suggests that dispersion can be modified greatly by changing interstitial air hole shape or size.

c) Drawing ratio and waveguide dispersion

Dispersion is usually modified by changing waveguide geometry. Material dispersion $D_m = -\frac{\lambda}{c}\frac{d^2 n_{co}}{d\lambda^2}$ and waveguide dispersion, $D_g = -\frac{\lambda}{c}\frac{d^2 n_g}{d\lambda^2}$ where n_g is the effective mode index when material dispersion is not considered, are loosely coupled. The total dispersion can be estimated by the summation of the two. Waveguide dispersion depends only on the geometry parameters of the waveguide, which are the lattice constant a and air hole radius R_a (generally the normalized parameter R_a/a is used) for the capillary tube PCF.

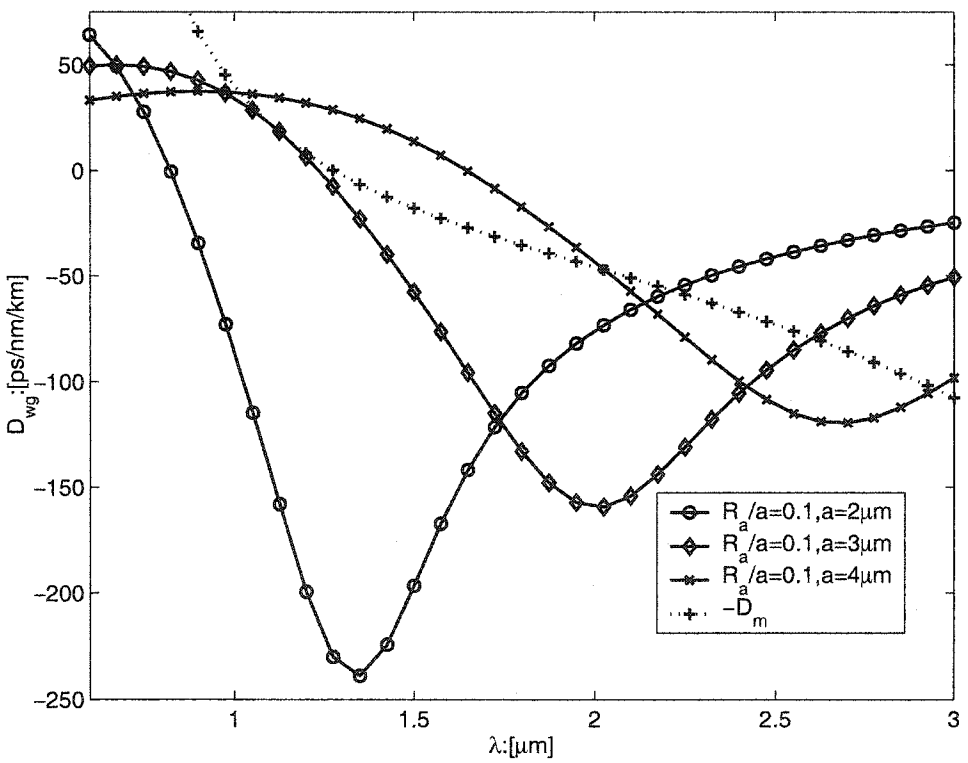

Figure 62. Waveguide dispersion with different core radius, i.e. different drawing ratio, with the same air-filling fraction. The negative material dispersion $-D_m$ is also shown in the figure (the dotted line with '+').

Reproduced with permission of the copyright owner. Further reproduction prohibited without permission.

Once the R_d/a ratio is determined, the dispersion is only affected by the drawing ratio s: $s = a/a_0$, a_0 is an arbitrary value for reference. Let $\varepsilon'(r) = \varepsilon(r/s)$, and plug it into (1) and follow the same procedure in [5] for the scaling properties of the Maxwell equations, we get: $\left(\nabla_t'^2 + \frac{k_0^2}{s^2}\varepsilon'\right)E_t' + \nabla_t'(E_t' \cdot \nabla_t' \ln \varepsilon') = \left(\frac{\beta_g}{s}\right)^2 E_t'$. This indicates that the wavelength $s\lambda$ corresponds a propagation constant β_g/s, or the effective mode index for the wavelength $s\lambda$ in the scaled system is the same as the referred one, hence, the waveguide dispersion in the scaled system can be predicted by [91]: $D_g'(\lambda) = \frac{1}{s} D_g(\lambda/s)$

For s>1, the waveguide dispersion curve will expand s along λ axis and attenuate s along D axis; for s<1, the curve will compress s along λ axis and amplify s along D axis. The effect of the drawing ratio on the waveguide dispersion is illustrated in Figure 62.

4.3 Air Guiding PCFs

The index guiding PCF usually uses a small air-filling ratio to ensure single mode operation. However, the air-guiding PCF uses a large air-filling ratio to generate a band gap and a defect mode in the band gap. The mode index of the defect mode guided in the air core is smaller than the index of air, 1.0.

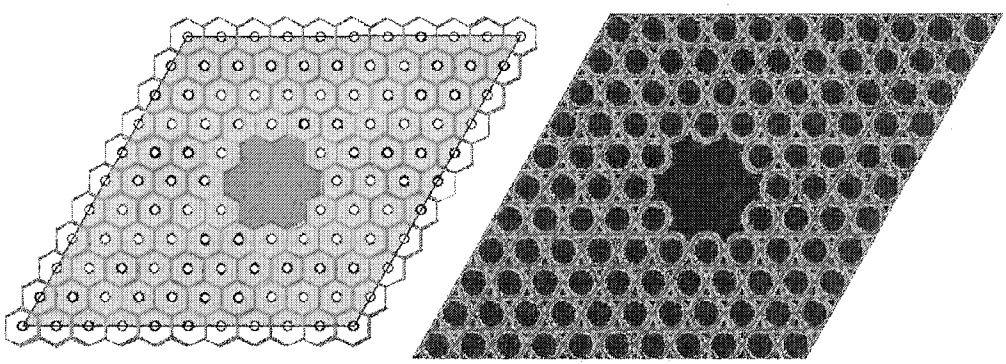

Figure 63. Air guiding PCFs. Left: PCF with hexagonal rods. Right: PCF with capillary tubes. In both cases, a big air core is formed by removing 7 rods in the center.

Figure 63 shows the schematic graph of possible air-guiding PCF's, where several rods are removed to form a big air hole. The calculation of this kind of fiber is much harder since it involves large supercell and large number of plane waves and the computation is very intensive. Also, due to the inherent weakness of the plane wave method, material dispersion is hard to include, hence dispersion properties are extremely hard to obtain.

Reproduced with permission of the copyright owner. Further reproduction prohibited without permission.

4.3.1 Band gap of the periodic cladding

We try the air guiding PCF with capillary tubes, assuming the inner hole: ε_a, R_a, the outer circle: ε_b, R_b, the background material is ε_c, the lattice constant: *a*. The band structure of the cladding material is shown in Figure 64 with $R_a/a=0.39$ and off-plane propagation constant $k_z=9.5$ using 289 plane waves. The band gap is from $k \bullet a=9.5$-9.6. The band structure shows there is a band gap close to $\beta=9.5$ between band 6 and 7, which means possible guidance in the air core.

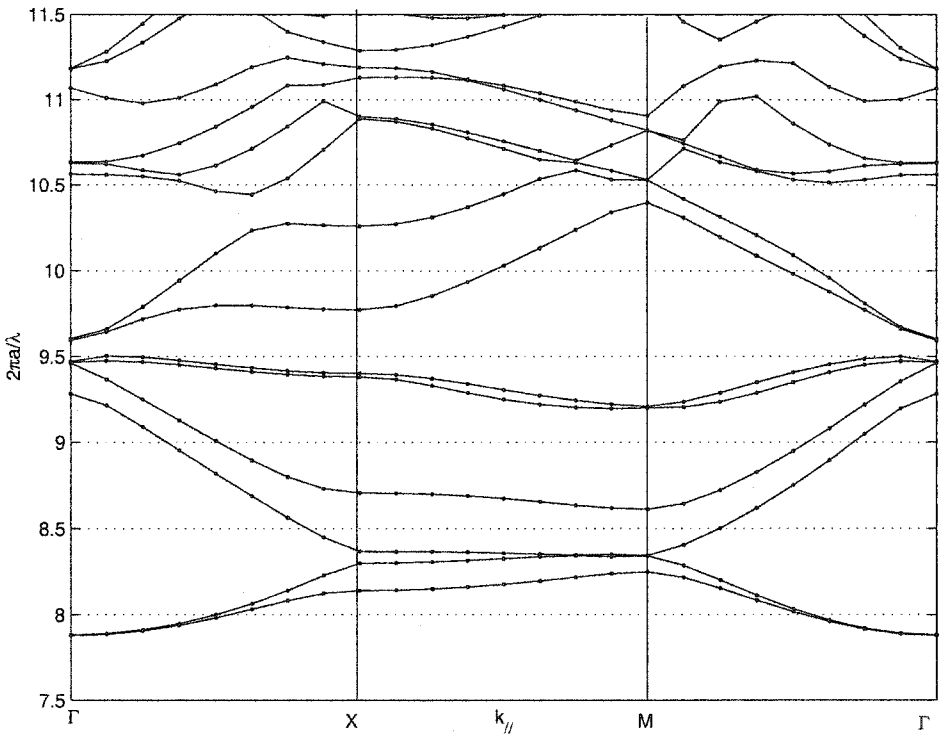

Figure 64. Band structure of a capillary PCF, $R_a=0.39a$, off-plane propagation constant=9.5. A band gap opens between band 6 and 7.

The variation of the band gap vs the propagation constants is calculated and shown in Figure 65. The glass line and air-line represent the dispersion relations when light propagates in infinite bulk glass and air, respectively; and the cladding line represents the dispersion relation when light propagates in the medium with an index of the average index of the cladding.

Reproduced with permission of the copyright owner. Further reproduction prohibited without permission.

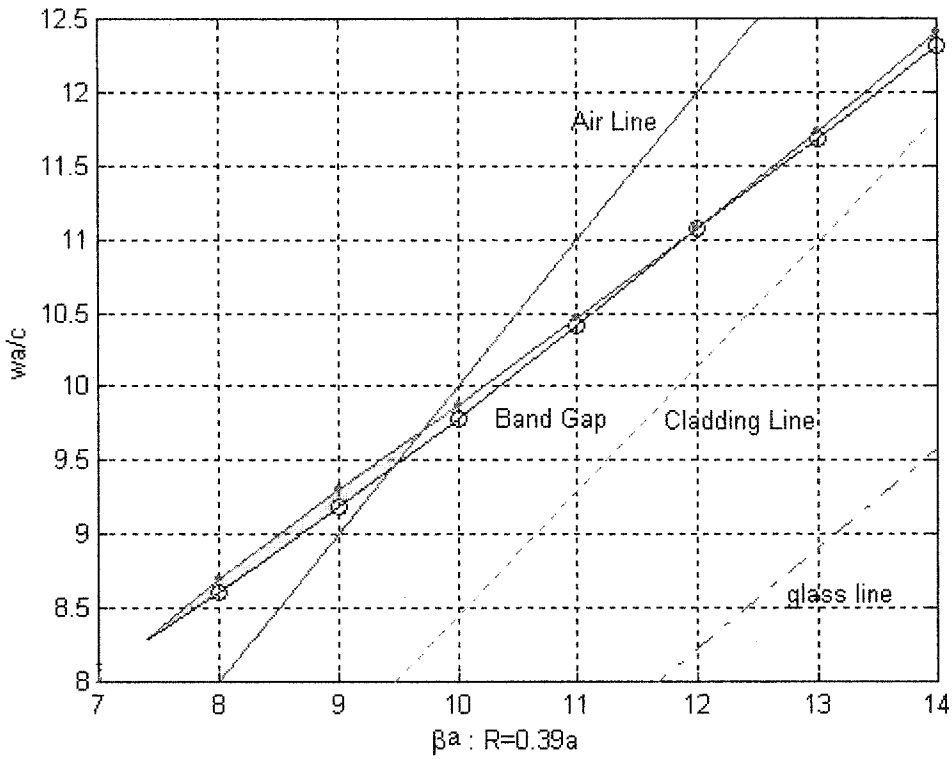

Figure 65. The variation of the first band gap of a capillary PCF vs the propagation constants along z-direction: R_a/a=0.39, calculated using plane wave method. The possible air guiding region is the shadowed one.

When the light state falls above the air-line, light propagates in air; when the light state falls below the air line, light decays in air. The yellow shadowed region falls above the air line and cladding line, also it is in the photonic band gap, so light will propagates in air and the cladding region, but is confined by PBG effect. The band gap which is below the air line shows some states decays in air and confined by PBG effect.

From the above two figures, we can get that the possible air guiding region for the PCF with R_a/a=0.39 is λ=0.64a-0.75a since k•a is from 8.3 to 9.7, and the propagation constant is β=7.5~9.5.

4.3.2 Air guiding mode

Since the large computation involved in the air-guiding PCFs, we used the approximation method for *H* mentioned above to reduce computation load. The parameters we use in the fiber analysis are: R/a=0.39, a 11x11 supercell, n=18 and number of plane waves=1165.

Reproduced with permission of the copyright owner. Further reproduction prohibited without permission.

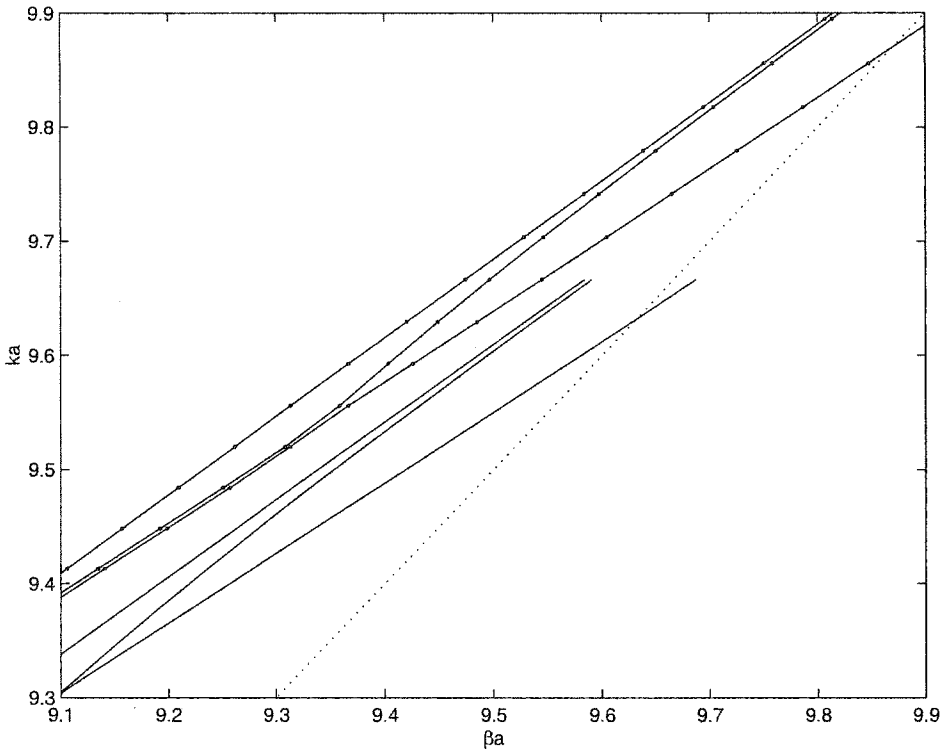

Figure 66. Air guiding mode (x-polarization) crossing the band gap. The line with solid dots represents the gap map with considering the material dispersion; the solid lines represents the gap map with no material dispersion; the dotted line is the air line.

Band gap for x- and y-polarization exists between mode 364 and 365, which is exactly the same as Figure 65 obtained by plane wave method. Defect mode introduced in the band gap, the defect mode is band 341. The dispersion curve for the x-polarization is shown in Figure 66.

When material dispersion is not considered, the wavelength range of the air guided mode: 0.66a-0.68a. When material dispersion is considered, (here lattice constant a=2.3um), The gap map shift upwards, the wavelength region for the air mode is 0.64a-0.66a. The three lines are band 340, 341 and 342, and the defect mode is band 341.

The GVD dispersion is very small since the dispersion relation is almost linear. Furthermore, since the light propagates in the air region, the nonlinear effect and loss is very small, which is excellent for high power transmission. Also, it is an omni-directional guide compared to conventional fiber base on total internal reflections.

The mode pattern of the defect air mode at λ=0.67a is shown in Figure 67. This shows remarkable difference from the index-guiding mode. The PBG-guided mode always shows the diffraction pattern of the structure, with several second maximums in the intensity pattern.

Reproduced with permission of the copyright owner. Further reproduction prohibited without permission.

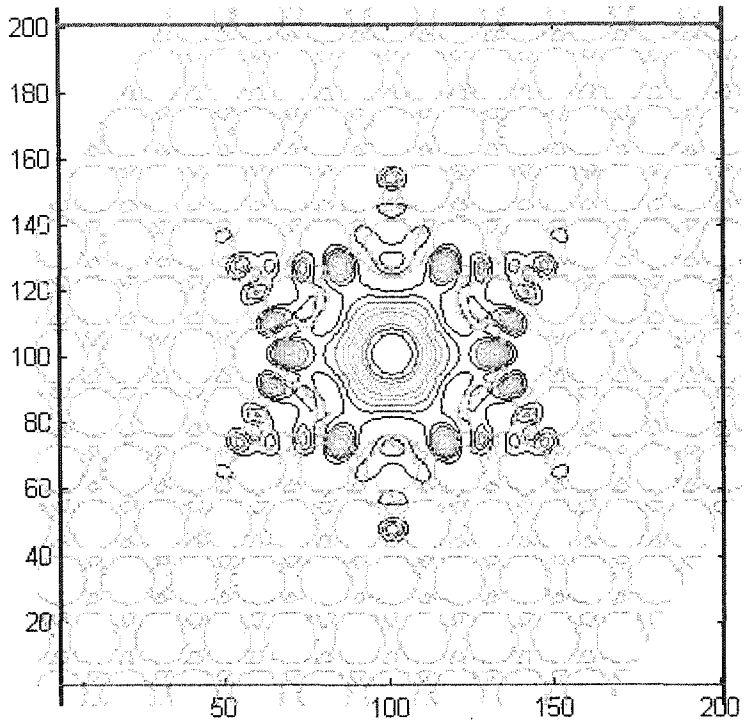

Figure 67. Intensity pattern of the transverse E field: fundamental mode guided in air core. The largest difference between the index-guided mode and the air-guided mode is that the PBG based defect mode presents a ring of diffraction pattern. λ=0.67a.

4.4 Discussion

Theoretically, other forms of PCF, such as the PCF with grapefruit cladding, non-periodic cladding can also be treated using this method. Recently, a new PCF fiber called Bragg fiber is proposed by MIT. This fiber is coaxial and can support a true single TEM mode, and this mode has no dispersion and is guided in the center air hole. The cladding is composed of periodic multi-layers with high index contrast, different and superior properties can be obtained. Further studies may be conducted in this area.

The different structure of the cladding gives more freedom in tailoring the mode pattern, group velocity dispersion. However, treating air-guiding fiber is not convenient and not very accurate since the fundamental mode is not the mode with lowest frequency, and the eigen frequency for the higher order is much less accurate than the lower one due to the limited number of plane waves. For this case, a FDTD method specialized for fiber analysis would be useful to yield accurate information. Also, other quantities, like the mode field diameter to measure the degree of confinement are not included.

Reproduced with permission of the copyright owner. Further reproduction prohibited without permission.

Other important properties, such as the transmission loss and bending loss are not included in this part, and they are also very important in practical purpose. Applications and fabrication of these fibers are in very active research. For example, PCF or holey fiber based fiber laser, large mode area fiber for high power transmission, large nonlinear fiber with very small mode area.

Reproduced with permission of the copyright owner. Further reproduction prohibited without permission.

CHAPTER V

FINITE DIFFERENCE TIME DOMAIN METHOD

5.1 INTRODUCTION

In the previous chapters, we have already solved many PBG problems. Those methods are all based on frequency-domain, using the steady state Maxwell equations plus the periodic boundary condition. They are stable, always able to give correct results. However, they have their own weakness: the heavy computation and large memory requirement for large PBG problems, difficulty in treating finite PBG structures, difficulty in obtaining dynamics in a PBG structure.

In this chapter, these difficulties are discussed and solved by the time-domain methods. First, the powerful finite difference time domain (FDTD) is used to solve open structures, and dynamic response of these structures. Some techniques to yield good and accurate results in FDTD are discussed, including the PML boundary condition, the total/scattered method, near-to-far field transformation, etc. Then the FDTD in generalized coordinates are discussed and the order-N method using this generalized FDTD for calculating the band structure of ideal photonic band gap structures is introduced.

5.2 SIMULATION OF PBG DEVICES USING FDTD METHOD

5.2.1 The Standard FDTD Algorithm

The FDTD algorithm was first introduced by Kane Yee in 1966, and it is now the most popular and robust method in modeling and simulating electromagnetic fields. In this section, the brief theory is described.

Consider a space with no electric or magnetic current sources, but there may exist materials that absorb electric or magnetic field energy. The time-dependent, differential form of Maxwell's equations is:

$$\nabla \times H = \sigma E + \varepsilon \frac{\partial E}{\partial t} \qquad \nabla \times E = -\left[\sigma_m H + \mu \frac{\partial H}{\partial t}\right] \tag{5.1}$$

where μ is the magnetic permeability, ε is the electric permittivity, σ is the electric conductivity and σ_m is an equivalent magnetic conductivity.

In $3D$ Cartesian rectangular coordinate system (x,y,z), the Maxwell's equations are decomposed into the following 6 equations:

$$\frac{\partial H_x}{\partial t} = \frac{1}{\mu}\left(\frac{\partial E_y}{\partial z} - \frac{\partial E_z}{\partial y} - \sigma_m H_x\right) \tag{5.2a}$$

Reproduced with permission of the copyright owner. Further reproduction prohibited without permission.

$$\frac{\partial H_y}{\partial t} = \frac{1}{\mu}\left(\frac{\partial E_z}{\partial x} - \frac{\partial E_x}{\partial z} - \sigma_m H_y\right) \tag{5.2b}$$

$$\frac{\partial H_z}{\partial t} = \frac{1}{\mu}\left(\frac{\partial E_x}{\partial y} - \frac{\partial E_y}{\partial x} - \sigma_m H_z\right) \tag{5.2c}$$

$$\frac{\partial E_x}{\partial t} = \frac{1}{\varepsilon}\left(\frac{\partial H_z}{\partial y} - \frac{\partial H_y}{\partial z} - \sigma E_x\right) \tag{5.2d}$$

$$\frac{\partial E_y}{\partial t} = \frac{1}{\varepsilon}\left(\frac{\partial H_x}{\partial z} - \frac{\partial H_z}{\partial x} - \sigma E_y\right) \tag{5.2e}$$

$$\frac{\partial E_z}{\partial t} = \frac{1}{\varepsilon}\left(\frac{\partial H_y}{\partial x} - \frac{\partial H_x}{\partial y} - \sigma E_z\right) \tag{5.2f}$$

Yee's algorithm solves the six coupled equations, both electric and magnetic fields in time and space. The main features of Yee's algorithm are:

E and H are interleaved. In 3D case, each E component is surrounded by four H components and each H component is surrounded by four E components, as shown in Figure 68. This provides a beautiful simple picture of a 3D structure.

The leapfrog time-stepping: All the E components in the 3D spaces are calculated and stored in memory for a particular time point using the H data previously stored in memory. Then all the H data are calculated and stored in memory using the E data just computed.

All derivatives in (5.3a-f), including the space derivatives and time derivatives, are replaced by central finite differences, which has a second order accuracy (2^{nd}-order FDTD scheme).

For simplicity, let u to represents the E_x, E_y, E_z, H_x, H_y, and H_z and use the notation as $u(i\Delta x, j\Delta y, k\Delta z, n\Delta t) = u_{ijk}^n$:

$$\frac{\partial u}{\partial x}(i\Delta x, j\Delta y, k\Delta z, n\Delta t) = \frac{\partial u_{ijk}^n}{\partial x} = \frac{u_{i+0.5,j,k}^n - u_{i-0.5,j,k}^n}{\Delta x} \tag{5.3}$$

$$\frac{\partial u}{\partial t}(i\Delta x, j\Delta y, k\Delta z, n\Delta t) = \frac{\partial u_{ijk}^n}{\partial t} = \frac{u_{i,j,k}^{n+0.5} - u_{i,j,k}^{n-0.5}}{\Delta t} \tag{5.4}$$

Reproduced with permission of the copyright owner. Further reproduction prohibited without permission.

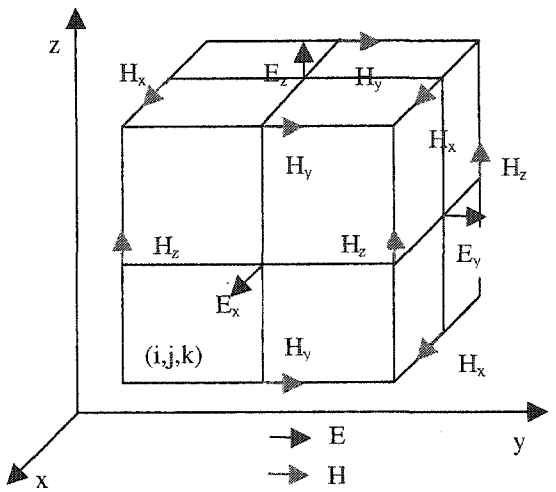

Figure 68. Position of the E and H about a cubic unit cell of the Yee space lattice.

First, assume we know all the values of E at the current time step n and all the H values at the previous half time step n-0.5, and then the H values at time step n+0.5 can be updated using the following equations:

$$H_x\Big|_{i,j,k}^{n+0.5} = \left(\frac{1-\frac{\rho'_{i,j,k}\Delta t}{2\mu_{i,j,k}}}{1+\frac{\rho'_{i,j,k}\Delta t}{2\mu_{i,j,k}}}\right) H_x\Big|_{i,j,k}^{n-0.5} + \left(\frac{\frac{\Delta t}{\mu_{i,j,k}}}{1+\frac{\rho'_{i,j,k}\Delta t}{2\mu_{i,j,k}}}\right)\left(\frac{E_y\Big|_{i,j,k+0.5}^{n} - E_y\Big|_{i,j,k-0.5}^{n}}{\Delta z} - \frac{E_z\Big|_{i,j+0.5,k}^{n} - E_z\Big|_{i,j-0.5,k}^{n}}{\Delta y}\right) \tag{5.5a}$$

$$H_y\Big|_{i,j,k}^{n+0.5} = \left(\frac{1-\frac{\rho'_{i,j,k}\Delta t}{2\mu_{i,j,k}}}{1+\frac{\rho'_{i,j,k}\Delta t}{2\mu_{i,j,k}}}\right) H_y\Big|_{i,j,k}^{n-0.5} + \left(\frac{\frac{\Delta t}{\mu_{i,j,k}}}{1+\frac{\rho'_{i,j,k}\Delta t}{2\mu_{i,j,k}}}\right)\left(\frac{E_z\Big|_{i+0.5,j,k}^{n} - E_z\Big|_{i-0.5,j,k}^{n}}{\Delta x} - \frac{E_x\Big|_{i,j,k+0.5}^{n} - E_x\Big|_{i,j,k-0.5}^{n}}{\Delta z}\right) \tag{5.5b}$$

$$H_z\Big|_{i,j,k}^{n+0.5} = \left(\frac{1-\frac{\rho'_{i,j,k}\Delta t}{2\mu_{i,j,k}}}{1+\frac{\rho'_{i,j,k}\Delta t}{2\mu_{i,j,k}}}\right) H_z\Big|_{i,j,k}^{n-0.5} + \left(\frac{\frac{\Delta t}{\mu_{i,j,k}}}{1+\frac{\rho'_{i,j,k}\Delta t}{2\mu_{i,j,k}}}\right)\left(\frac{E_x\Big|_{i,j+0.5,k}^{n} - E_x\Big|_{i,j-0.5,k}^{n}}{\Delta y} - \frac{E_y\Big|_{i+0.5,j,k}^{n} - E_y\Big|_{i-0.5,j,k}^{n}}{\Delta x}\right) \tag{5.5c}$$

Now we will advance another half time step: using the E values at time step n and H values at time step n+0.5, we can update E values at time step n+1:

$$E_x\Big|_{i,j,k}^{n+1} = \left(\frac{1-\frac{\sigma_{i,j,k}\Delta t}{2\varepsilon_{i,j,k}}}{1+\frac{\sigma_{i,j,k}\Delta t}{2\mu_{i,j,k}}}\right) E_x\Big|_{i,j,k}^{n} + \left(\frac{\frac{\Delta t}{\varepsilon_{i,j,k}}}{1+\frac{\sigma_{i,j,k}\Delta t}{2\varepsilon_{i,j,k}}}\right)\left(\frac{H_z\Big|_{i,j+0.5,k}^{n+0.5} - H_z\Big|_{i,j-0.5,k}^{n}}{\Delta y} - \frac{H_y\Big|_{i,j,k+0.5}^{n} - H_y\Big|_{i,j,k-0.5}^{n}}{\Delta z}\right) \tag{5.6a}$$

Reproduced with permission of the copyright owner. Further reproduction prohibited without permission.

$$E_y\Big|_{i,j,k}^{n+1} = \left(\frac{1-\frac{\sigma_{i,j,k}\Delta t}{2\varepsilon_{i,j,k}}}{1+\frac{\sigma_{i,j,k}\Delta t}{2\mu_{i,j,k}}}\right) E_y\Big|_{i,j,k}^{n} + \left(\frac{\frac{\Delta t}{\varepsilon_{i,j,k}}}{1+\frac{\sigma_{i,j,k}\Delta t}{2\varepsilon_{i,j,k}}}\right)\left(\frac{\frac{H_x\Big|_{i,j,k+0.5}^{n+0.5} - H_x\Big|_{i,j,k-0.5}^{n}}{\Delta z} - \frac{H_z\Big|_{i+0.5,j,k}^{n} - H_z\Big|_{i-0.5,j,k}^{n}}{\Delta x}}\right) \tag{5.6b}$$

$$E_z\Big|_{i,j,k}^{n+1} = \left(\frac{1-\frac{\sigma_{i,j,k}\Delta t}{2\varepsilon_{i,j,k}}}{1+\frac{\sigma_{i,j,k}\Delta t}{2\mu_{i,j,k}}}\right) E_z\Big|_{i,j,k}^{n} + \left(\frac{\frac{\Delta t}{\varepsilon_{i,j,k}}}{1+\frac{\sigma_{i,j,k}\Delta t}{2\varepsilon_{i,j,k}}}\right)\left(\frac{\frac{H_y\Big|_{i+0.5,j,k}^{n+0.5} - H_y\Big|_{i-0.5,j,k}^{n}}{\Delta x} - \frac{H_x\Big|_{i,j+0.5,k}^{n} - H_x\Big|_{i,j-0.5,k}^{n}}{\Delta y}}\right) \tag{5.6c}$$

For 2D TE/TM and 1D cases, these equations are greatly simplified.

For those points at the boundary, special attention should be paid to. For time, we use initial condition, i.e., we assume we know all the E or H components at all grid points at the time beginning. For space, we use boundary condition, depending on the physics of the problem. At each time step, all the E and H components at all grid points in the whole space should be updated and stored properly. In the time step, we performed the updating of E at the first half and H at the second half. Thus, as the time goes, the electromagnetic waves in the space are simulated.

To guarantee the stability of the leap-frog algorithm, there is a requirement for the time and space length of the Yee mesh. For 3D cases, it should be (for 2nd-order FDTD scheme only):

$$\Delta t \le \frac{1}{c\sqrt{\frac{1}{(\Delta x)^2}+\frac{1}{(\Delta y)^2}+\frac{1}{(\Delta z)^2}}} \tag{5.7}$$

For 2D FDTD problem:

$$\Delta t \le \frac{1}{c\sqrt{\frac{1}{(\Delta x)^2}+\frac{1}{(\Delta y)^2}}} \tag{5.8}$$

The general procedure of FDTD algorithm can be like this:

Reproduced with permission of the copyright owner. Further reproduction prohibited without permission.

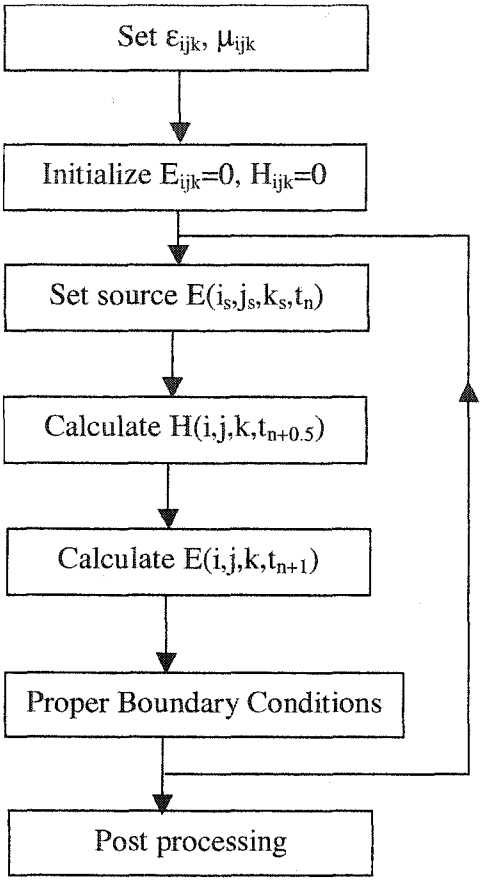

Figure 69. The flowchart of a general FDTD algorithm.

5.2.2 Absorption Boundary Condition (ABC)

Absorption boundary condition is used to simulate 'open' electromagnetic region, and it cannot be obtained from Maxwell's equations. So this kind of boundary is not a physical boundary, and its function is to terminate the region of study by absorbing all outgoing electromagnetic waves, regardless of the polarization, frequency, direction or intensity. The reflection coefficient of the boundary should be very close to zero in any cases. Hence, all the outgoing waves from inside never returns, which simulates the object in a free space.

5.2.3 Perfectly Matched Layer (PML)

PML was first introduced by J. P. Berenger in 1994 [92]. This technique introduces several absorptive media layers to absorb both E and H waves inside the layers. By carefully design of the perfectly matched layers, absorption can be controlled to be very low and suppression can be up to 80dB.

Reproduced with permission of the copyright owner. Further reproduction prohibited without permission.

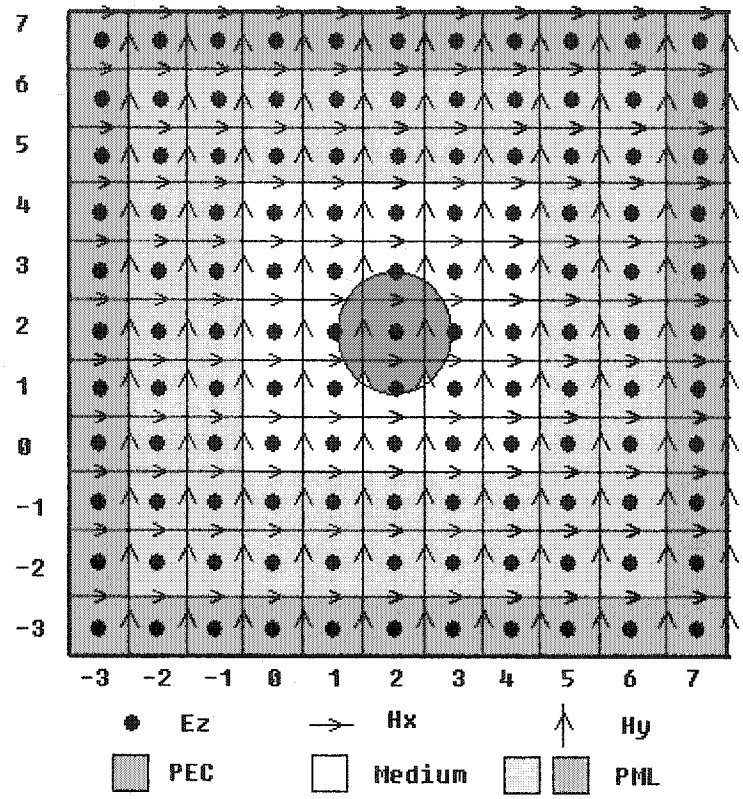

Figure 70. The PML boundary condition for FDTD in a 2D TM problem.

The scheme is described using a 2D TM as below. Figure 70 shows the FDTD algorithm using PML boundary condition. The white area is the one we have to study. Outside it is a 2-layer PML to absorb the outgoing waves. The outermost layer is a perfect electric conductor and it can reflect 100% waves incident upon it.

The PML medium is a non-physical medium and it has the same ε and μ as the vacuum, but it is absorptive and has the electric and magnetic conductivity which satisfy:

$$\frac{\sigma}{\varepsilon_0} = \frac{\sigma_m^*}{\mu_0} \tag{5.9}$$

The PML layers are constructed as follows:

Assuming each cell has a conductivity denoted by $PML(\sigma_x, \sigma_x^*, \sigma_y, \sigma_y^*)$, the PML layer in the x-direction is $PML(\sigma_x, \sigma_x^*, 0, 0)$, and in the y-direction is $PML(0, 0, \sigma_y, \sigma_y^*)$. The four corners should be $PML(\sigma_x, \sigma_x^*, \sigma_y, \sigma_y^*)$. The distribution of σ and σ* can be power-law, increasing from zero at the innermost cell to the maximum at the outermost layer, i.e.:

Reproduced with permission of the copyright owner. Further reproduction prohibited without permission.

$\sigma(\rho) = \sigma_{\max}\left(\frac{\rho}{\Delta}\right)^n$. The reflection coefficient can be calculated for PML layers with a thickness of Δ can be evaluated as: $R(\theta) = e^{-2\Delta(\sigma\cos\theta/\varepsilon_0 c)}$.

All the E and H components are divided into two components, for 2D TM cases, they are:

$$E_z = E_{zx} + E_{zy} \qquad H_x = H_{xx} + H_{xy} \qquad H_y = H_{yx} + H_{yy}. \tag{5.10}$$

And the Maxwell's equations for TM case are:

$$\varepsilon\frac{\partial E_{zx}}{\partial t} + \sigma_x E_{zx} = \frac{\partial(H_{yx} + H_{yy})}{\partial x} \tag{5.11a}$$

$$\varepsilon\frac{\partial E_{zy}}{\partial t} + \sigma_y E_{zy} = -\frac{\partial(H_{xx} + H_{xy})}{\partial y} \tag{5.11b}$$

$$\mu\frac{\partial(H_{xx} + H_{xy})}{\partial t} + \sigma_y^*(H_{zx} + H_{xy}) = -\frac{\partial(E_{zx} + E_{zy})}{\partial y} \tag{5.11c}$$

$$\mu\frac{\partial(H_{yx} + H_{yy})}{\partial t} + \sigma_x^*(H_{yx} + H_{yy}) = -\frac{\partial(E_{zx} + E_{zy})}{\partial x} \tag{5.11d}$$

In the PML layers, the uniform time-stepping cannot be used, the exponential time-stepping is used instead.

5.2.3 Sources and Dispersion Optimization

Generally, a source is needed to emit electromagnetic waves into the medium. Point sources can be used to form spherical waves, and line sources can be used to form cylindrical waves and plane waves. Dipole source can emit directional waves and is ideal for wave-guiding structures.

Also, the source can be a pulse or a continuous wave. A pulse wave is especially useful since it contains all the needed frequency components. Analysis of the input and output pulse can easily get the response of the medium. A continuous source can be used to analyze the steady state response of the system.

The coupling between source and the mode of study is important in order to excite that mode. If the excitation source and the mode to be excited are orthogonal and have a zero coupling, no mode will be excited. Symmetry plays an important role in this analysis.

The physics of a system determines largely how many time steps are needed to achieve a satisfactory result. Generally, a continuous single-frequency sine wave needs only number of time steps which is large enough to let the wave propagate through the system. Pulse source requires generally much longer time steps especially for PBG structures, since those eigen modes in PBG

Reproduced with permission of the copyright owner. Further reproduction prohibited without permission.

structures involve a lot of multiple scatterings, which can be seen through a microcavity calculation in the next sections.

Sources can be included in the FDTD grid as "soft" or "hard" sources. The soft source will update as a normal FDTD cell, and the hard source will not. The soft source will not introduce any reflection from the source grid, but the hard source will. However, the waveform of hard source is exactly known but soft source is unknown since it is added on the normal FDTD cell. The reflections caused by hard sources are especially serious for line sources.

To produce ideal plane wave sources, the total-field/scattered-field has to be used. It uses a 1D FDTD grid to produce a wave along it, and use the value to update the source in the whole space. This could also offer other flexibility in choosing any incident direction, which can be used to differentiate those degenerate modes in photonic crystals.

Since Yee's method cut the isotropic space into anisotropic cells, it will introduce inherent dispersion. These numerical dispersion can be accumulated to a considerable amount which is harmful for scattering problem since it involves many phase canceling. Although the dispersion can be reduced by using small enough cells and time-step, the computation will grow rapidly. In photonic band gap devices, many multi-scatterings take place and the dispersion may cause accumulated phase error, which if large enough will finally produce inaccurate description of the problem. A dispersion optimized 4^{th} order FDTD for PBG device simulation is used to reduce the numerical dispersion.

5.3 The Order-N Method For Ideal PBG Structures

As mentioned in Chapter II, the complexity of the plane wave method is $O(N^3)$. The computation time for a large system is so long that its performance becomes unacceptable. FDTD method was first brought out to overcome this weakness [93]. Just like the plane wave method (PWM), FDTD can also be used to calculate the band structure of the infinite ideal PBG structures, using the periodic boundary condition (PBC). Compared to the plane wave method, the complexity of this approach is $O(N)$ [93, 94], and hence is superior when dealing with really big and complicated problems.

In this method, the unit cell of the periodic structure is the space to be studied for the FDTD algorithm, and periodic boundary condition is used to treat cells on the boundary. An initial field distribution, $E(\mathrm{r})$ or $H(\mathrm{r})$ is given at time zero. After some time of scattering, only those eigen modes can remain in the space, and other modes are gone as radiation loss. Fourier analysis of these modes left can reveal its band structure.

Reproduced with permission of the copyright owner. Further reproduction prohibited without permission.

5.3.1 Non-orthogonal lattice

Since the unit cell of an ideal PBG structure is not always a cubic in 3D or a rectangle in 2D, the standard Yee mesh and FDTD algorithm should be modified to solve this kind of problem. One good method is given by [66, 95]. A brief description is given below:

In a generalized coordinates denoted by (u_1,u_2,u_3), the Maxwell's equations (5.1) become:

$$\nabla_q \times \hat{H} = \hat{\sigma}\hat{E} + \varepsilon_0 \hat{\varepsilon}(r)\frac{\partial \hat{E}}{\partial t} \qquad \nabla_q \times \hat{E} = -\left[\hat{\sigma}_m \hat{H} + \mu_0 \hat{\mu}(r)\frac{\partial \hat{H}}{\partial t}\right] \tag{5.12}$$

where q is 1, 2, 3 and the renormalized fields are:

$$\hat{E}_i = Q_i E_i \qquad \hat{H}_i = Q_i H_i \tag{5.13}$$

with
$$Q_i = \sqrt{\left(\frac{\partial x}{\partial q_i}\right)^2 + \left(\frac{\partial y}{\partial q_i}\right)^2 + \left(\frac{\partial z}{\partial q_i}\right)^2} \tag{5.14}$$

The effective ε and μ tensors are:

$$\hat{\varepsilon}^{ij}(r) = \varepsilon(r) g^{ij} |u_1 \cdot u_2 \times u_3| \frac{Q_1 Q_2 Q_3}{Q_i Q_j Q_0} \qquad \hat{\mu}^{ij}(r) = \mu(r) g^{ij} |u_1 \cdot u_2 \times u_3| \frac{Q_1 Q_2 Q_3}{Q_i Q_j Q_0} \tag{5.15}$$

$$\hat{\sigma} = \frac{\Delta t \sigma}{\varepsilon_0 \varepsilon(r)} \qquad \hat{\sigma}_m = \frac{\Delta t \sigma_m}{\mu_0 \mu(r)} \tag{5.16}$$

where g is the metric which can be obtained using the 3 unit vectors,

$$g = \begin{bmatrix} u_1 \cdot u_1 & u_1 \cdot u_2 & u_1 \cdot u_3 \\ u_2 \cdot u_1 & u_2 \cdot u_2 & u_2 \cdot u_3 \\ u_3 \cdot u_1 & u_3 \cdot u_2 & u_3 \cdot u_3 \end{bmatrix} \tag{5.17}$$

As in Chapter II, in the generalized coordinates, we have:

$$\left|r^2\right| = \vec{r}^{\,T}[g]\vec{r} \tag{5.18}$$

Use forward finite difference for E-field, backward finite difference for H-field (both space and time):

$$\begin{aligned} \hat{E}_1(r, t+\Delta t) = {} & [1-\hat{\sigma}]\hat{E}_1(r,t) \\ & + \left[\hat{\varepsilon}^{-1}(r)\right]^{11}\left\{\hat{H}'_3(r,t) - \hat{H}'_3(r-b,t) - \hat{H}'_2(r,t) + \hat{H}'_2(r-c,t)\right\} \\ & + \left[\hat{\varepsilon}^{-1}(r)\right]^{12}\left\{\hat{H}'_1(r,t) - \hat{H}'_1(r-c,t) - \hat{H}'_3(r,t) + \hat{H}'_3(r-a,t)\right\} \\ & + \left[\hat{\varepsilon}^{-1}(r)\right]^{13}\left\{\hat{H}'_2(r,t) - \hat{H}'_2(r-a,t) - \hat{H}'_1(r,t) + \hat{H}'_1(r-b,t)\right\} \end{aligned} \tag{5.19a}$$

Reproduced with permission of the copyright owner. Further reproduction prohibited without permission.

$$\begin{aligned}\hat{E}_2(r,t+\Delta t) = [1-\hat{\sigma}]\hat{E}_2(r,t) \\ &+ [\hat{\varepsilon}^{-1}(r)]^{21}\{\hat{H}_3'(r,t) - \hat{H}_3'(r-b,t) - \hat{H}_2'(r,t) + \hat{H}_2'(r-c,t)\} \\ &+ [\hat{\varepsilon}^{-1}(r)]^{22}\{\hat{H}_1'(r,t) - \hat{H}_1'(r-c,t) - \hat{H}_3'(r,t) + \hat{H}_3'(r-a,t)\} \\ &+ [\hat{\varepsilon}^{-1}(r)]^{23}\{\hat{H}_2'(r,t) - \hat{H}_2'(r-a,t) - \hat{H}_1'(r,t) + \hat{H}_1'(r-b,t)\}\end{aligned} \tag{5.19b}$$

$$\begin{aligned}\hat{E}_3(r,t+\Delta t) = [1-\hat{\sigma}]\hat{E}_3(r,t) \\ &+ [\hat{\varepsilon}^{-1}(r)]^{31}\{\hat{H}_3'(r,t) - \hat{H}_3'(r-b,t) - \hat{H}_2'(r,t) + \hat{H}_2'(r-c,t)\} \\ &+ [\hat{\varepsilon}^{-1}(r)]^{32}\{\hat{H}_1'(r,t) - \hat{H}_1'(r-c,t) - \hat{H}_3'(r,t) + \hat{H}_3'(r-a,t)\} \\ &+ [\hat{\varepsilon}^{-1}(r)]^{33}\{\hat{H}_2'(r,t) - \hat{H}_2'(r-a,t) - \hat{H}_1'(r,t) + \hat{H}_1'(r-b,t)\}\end{aligned} \tag{5.19c}$$

$$\hat{H}_1'(r,t+\Delta t) = [1+\hat{\sigma}_m]^{-1}\begin{bmatrix}\hat{H}_1'(r,t) \\ -\left(\frac{\Delta t c_0}{Q_0}\right)^2[\hat{\mu}^{-1}(r)]^{11}\{\hat{E}_3(r+b,t) - \hat{E}_3(r,t) - \hat{E}_2(r+c,t) + \hat{E}_2(r,t)\} \\ -\left(\frac{\Delta t c_0}{Q_0}\right)^2[\hat{\mu}^{-1}(r)]^{12}\{\hat{E}_1(r+c,t) - \hat{E}_1(r,t) - \hat{E}_3(r+a,t) + \hat{E}_3(r,t)\} \\ -\left(\frac{\Delta t c_0}{Q_0}\right)^2[\hat{\mu}^{-1}(r)]^{13}\{\hat{E}_2(r+a,t) - \hat{E}_2(r,t) - \hat{E}_1(r+b,t) + \hat{E}_1(r,t)\}\end{bmatrix} \tag{5.19d}$$

$$\hat{H}_2'(r,t+\Delta t) = [1+\hat{\sigma}_m]^{-1}\begin{bmatrix}\hat{H}_2'(r,t) \\ -\left(\frac{\Delta t c_0}{Q_0}\right)^2[\hat{\mu}^{-1}(r)]^{21}\{\hat{E}_3(r+b,t) - \hat{E}_3(r,t) - \hat{E}_2(r+c,t) + \hat{E}_2(r,t)\} \\ -\left(\frac{\Delta t c_0}{Q_0}\right)^2[\hat{\mu}^{-1}(r)]^{22}\{\hat{E}_1(r+c,t) - \hat{E}_1(r,t) - \hat{E}_3(r+a,t) + \hat{E}_3(r,t)\} \\ -\left(\frac{\Delta t c_0}{Q_0}\right)^2[\hat{\mu}^{-1}(r)]^{23}\{\hat{E}_2(r+a,t) - \hat{E}_2(r,t) - \hat{E}_1(r+b,t) + \hat{E}_1(r,t)\}\end{bmatrix} \tag{5.19e}$$

Reproduced with permission of the copyright owner. Further reproduction prohibited without permission.

$$\hat{H}_3'(r,t+\Delta t)=\left[1+\hat{\sigma}_m\right]^{-1}\begin{bmatrix}\hat{H}_3'(r,t)\\ -\left(\frac{\Delta t c_0}{Q_0}\right)^2\left[\hat{\mu}^{-1}(r)\right]^{\beta 1}\left\{\hat{E}_3(r+b,t)-\hat{E}_3(r,t)-\hat{E}_2(r+c,t)+\hat{E}_2(r,t)\right\}\\ -\left(\frac{\Delta t c_0}{Q_0}\right)^2\left[\hat{\mu}^{-1}(r)\right]^{\beta 2}\left\{\hat{E}_1(r+c,t)-\hat{E}_1(r,t)-\hat{E}_3(r+a,t)+\hat{E}_3(r,t)\right\}\\ -\left(\frac{\Delta t c_0}{Q_0}\right)^2\left[\hat{\mu}^{-1}(r)\right]^{\beta 3}\left\{\hat{E}_2(r+a,t)-\hat{E}_2(r,t)-\hat{E}_1(r+b,t)+\hat{E}_1(r,t)\right\}\end{bmatrix} \tag{5.19f}$$

where $\hat{H}'=\dfrac{\Delta t}{\varepsilon_0 Q_0}\hat{H}$ and $a=Q_1, b=Q_2, c=Q_3$.

The stability condition is: $\Delta t < \dfrac{1}{c\sqrt{\dfrac{1}{Q_1^2}+\dfrac{1}{Q_2^2}+\dfrac{1}{Q_3^2}}}$.

5.3.2 Periodic Boundary Condition (PBC)

The ABCs are apparently unsuitable for this case, since the reflection at the boundary exists and cannot be discarded. These reflections reflect the existence of the surrounding periodic cells.

When updating the cells on the boundary, we need again the Bloch theory. Take H as example:

$$\hat{H}(r+R_l)=e^{ik\cdot R_l}\hat{H}(r) \qquad \hat{E}(r+R_l)=e^{ik\cdot R_l}\hat{E}(r) \tag{5.20}$$

Figure 71 shows a 2D triangular unit cell with a cylinder in the center. The sub-cells in the boundary can be updated using the inside cells. The gray cells represent the boundary of the unit cell, and the cells outside the boundary are obtained using the above Bloch's theorem. Hence, all the cells can be updated using the above finite difference equations.

Reproduced with permission of the copyright owner. Further reproduction prohibited without permission.

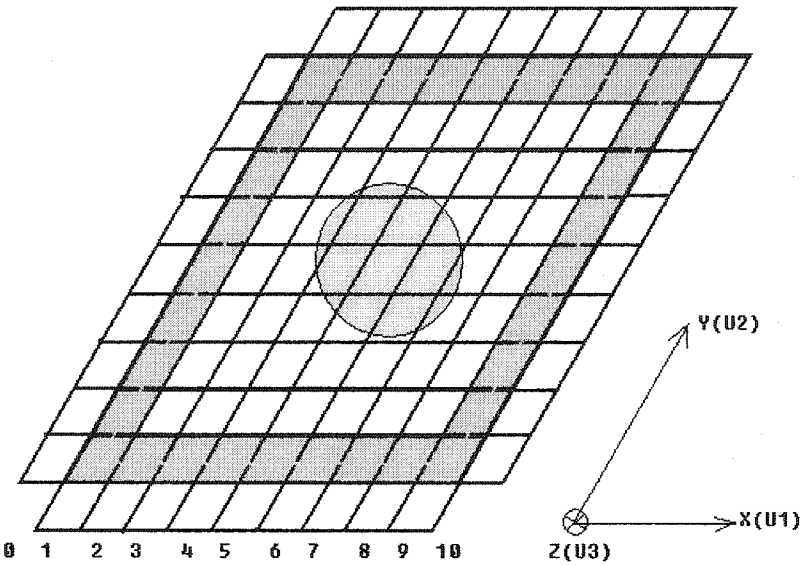

Figure 71. Periodic Boundary Condition for a 2D triangular unit cell. The unit cell is divided into cells along the unit vectors. The gray cells are the boundary and the cells outside the boundary are updated using periodic boundary condition. All the cells in the unit cell (including the boundary) can be updated using the FDTD algorithm.

5.3.3 Initial Condition

The initial condition is very important while calculating a PBG band. The initial field should contain all the components of all eigen modes, or else some eigen modes will be missing. The common initial field distribution while calculating the bands of a PBG structure is [94]:

$$H(r)=\sum_{G} h_0\left(\vec{k}+\vec{G}\right)e^{i\left(\vec{k}+\vec{G}\right)\vec{r}} \tag{5.23}$$

$$h_0\left(\vec{k}+\vec{G}\right)=v\times\left(\vec{k}+\vec{G}\right) \tag{5.24}$$

and:

$$v=[1,1,1],\ E(r)=0 \tag{5.25}$$

5.3.4 Example: 2D triangular lattice

To show how this algorithm works, we show how a 2D triangular lattice with air holes in GaAs substrate is calculated. The parameters for this structure are: ε_a=13, ε_b=1, R/a=0.28. The wave vector k is from Γ to M, and 20 points are taken. TE and TM modes are calculated at the same time. The lattice constant is 0.5482μm, and each direction is divided into 21 sections. The time step dt=5.5634e-17s. The precision of the eigen frequencies is largely affected by the fineness of the mesh, so we make sure to have a fine enough mesh. The band is also calculated

Reproduced with permission of the copyright owner. Further reproduction prohibited without permission.

using PWM method. As seen from Figure 72, there is a good agreement between these two methods.

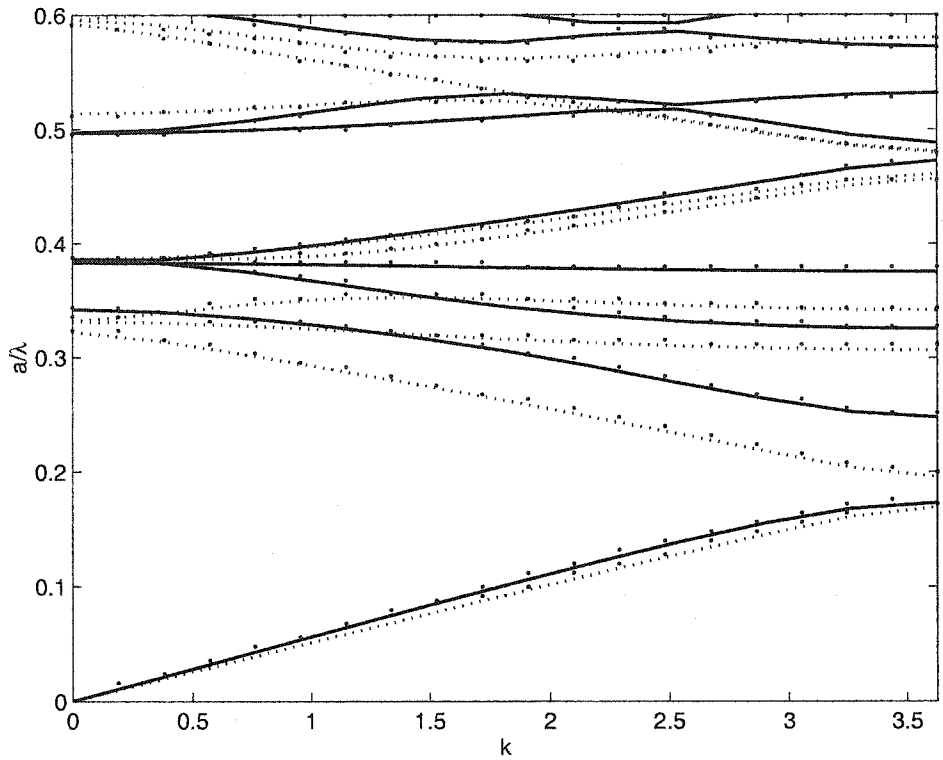

Figure 72. Band gap of a 2D triangular lattice using FDTD method. Solid line: TE using PWM; dotted line: TM using PWM; dot: FDTD.

5.4 PBG Dynamics Analysis Using FDTD

A finite sized PBG structure is of more interest. In this case, a FDTD and PML boundary are mostly used in simulation. To do efficient and accurate simulations, some factors need careful considerations. First, the studied geometry should be represented using a fine enough mesh. Also, the time step should be small enough to achieve minimized dispersion. The FDTD algorithm may accumulate large numerical dispersion and it will affect seriously the accuracy to those problems with multiple-scattering process since they involve many phase cancels. Since PBG devices involve many coherent scattering, dispersion is vital for obtaining reliable results. The simulation requires fine mesh and small time step and long time simulation. However, when Δt or Δx is getting smaller, more number of time steps is needed and simulation time is much longer. Generally, the safe time step can be chosen as 1/10~1/20 of the shortest wavelength, which indicates if the shortest wavelength is longer, a larger Δt can be used.

Reproduced with permission of the copyright owner. Further reproduction prohibited without permission.

When spectral information is to be extracted from the time domain field variations, proper excitation sources should be chosen to get satisfactory results. Generally, a Gaussian pulse is used in this case, which has a form of $A\exp\left[-\frac{(t-t_0)^2}{t_w^2}\right]\sin[2\pi f_0(t-t_0)]$. t_0 should be large enough to make the signal changes slowly from zero at the time of start point, and t_w should be small enough to cover the frequency range since the FWHP bandwidth can be calculated as $B_W = 2/t_w$. The number of time steps n_t is crucial to get meaningful spectral information. Using FFT, the normalized frequency (to c/a) for ith component is calculated as $\frac{i}{n_t c\Delta t}$ and the highest frequency is $\frac{0.5n_t}{n_t c\Delta t}$. The more number of time steps is used, the higher spectrum resolution will be obtained, which is crucial to get those very narrow filter spectra.

Another important point when finding the spectral information from time-varied fields is that, field at one single location is generally not sufficient to guarantee correct information. Since modes in PBG structures are well defined, the detection point may be on the field nodes of some specific eigen modes, thus leading an incorrect reporting of these frequencies. A safe approach is to choose sufficient number of detectors at symmetric and non-symmetric locations.

5.4.1 PBG Micro-cavity

Consider a finite PBG structure in free space: the PBG is a 5x5 lattice with GaAs rods (ε_a=11.56 and R=0.20a, a=1μm) in air, and the center rod is enlarged with R=0.60a, as is shown in Figure 73. The whole space is discretized into a 200x200 mesh, with Δx=Δy=0.025μm, time step Δt=5.89e-17s and number of time steps=50,000.A Gaussian pulse with a center frequency of 1.05e14Hz.covering the whole band gap is used. The number of PML layers is 10.
According to PWM analysis, this micro-cavity supports four modes as shown in Chapter III, and they are listed in the table below.

Table 9. Defect mode frequencies and their symmetries.

Defect Mode	Frequency	Mode pattern symmetry
Mode 1	0.2970	Odd-odd quadrupole
Mode 2	0.3190	Even-even quadrupole, odd-odd to the axis rotated 45°
Mode 3	0.3345	Even-even 2nd monopole
Mode 4	0.3916	Doubly degenerate, odd-even mode and even-odd mode

Reproduced with permission of the copyright owner. Further reproduction prohibited without permission.

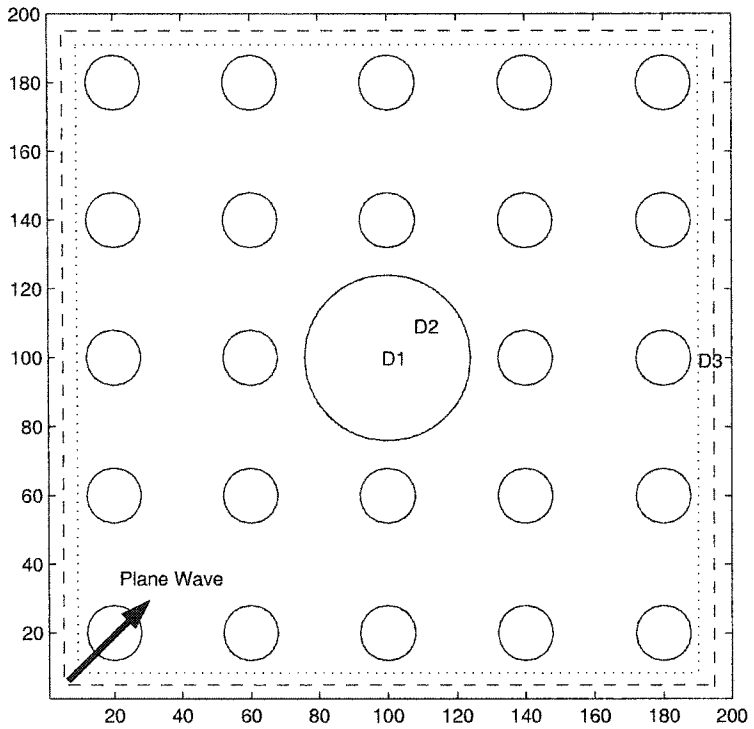

Figure 73. The setup for calculation of the defect modes in a microcavity. 5x5 GaAs rod in the air with radius of 0.20a, the bigger rod has a radius of 0.60a.

Three receivers are placed inside crystal. Detector 1 is placed in the center of the defect, detector 2 is placed in the direction of 45 degrees, and detector 3 is placed on the x-axis outside the micro-cavity. According to the symmetries of these defect modes, detector 1 will only detect mode 1 since other modes has no field at this point; detector 2 will not detector mode 2 and detector 3 will not detect mode 1 since they are located on the nodal plane of these modes.

Four simulations are done with the incident plane wave incidence angles of 0, 45, 60 and 90 degrees. To create an ideal plane wave source, total-field/scattered-field FDTD scheme is used. The far field pattern is calculated at the same time.

Fourier transform of these fields can reveal the mode spectrum as shown in Figure 74 (obtained using the 60 degree incidence). Just as predicted, a single detector cannot detect all the defect modes in the cavity.

Reproduced with permission of the copyright owner. Further reproduction prohibited without permission.

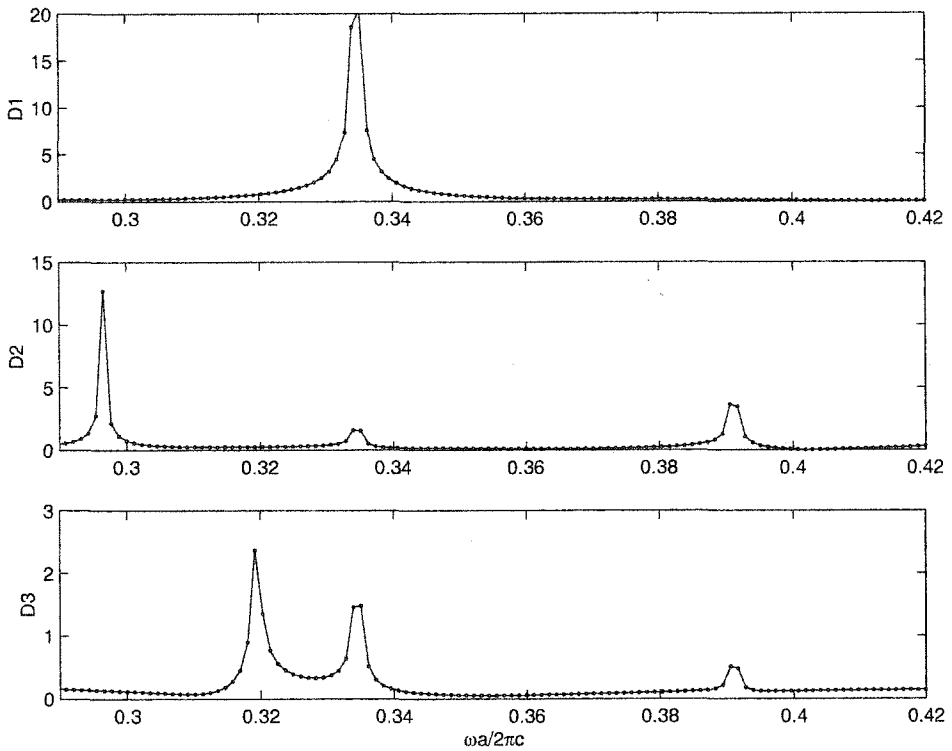

Figure 74. The spectrum obtained from the three detectors inside the crystal.

The symmetry can be studied using the different incidence. The spectral analysis can disclose those modes excited by the incidence, which is shown in Table 10. To differentiate the degenerate modes, orthogonal incidences should be used to excite each of them individually.

Table 10. Excited defect modes in the micro-cavity by plane waves with different incident angles.

Incidence	Mode 1	Mode 2	Mode 3	Mode 4(1)	Mode 4(2)
0°	No	Yes	Yes	Yes	No
45°	Yes	No	Yes	Yes	Yes
60°	Yes	Yes	Yes	Yes	Yes
90°	No	Yes	Yes	No	Yes

The far field pattern is important to its coupling strength and its direction dependence. Figure 75 shows the pattern for each mode. Special attention should be paid to the degenerate modes

Reproduced with permission of the copyright owner. Further reproduction prohibited without permission.

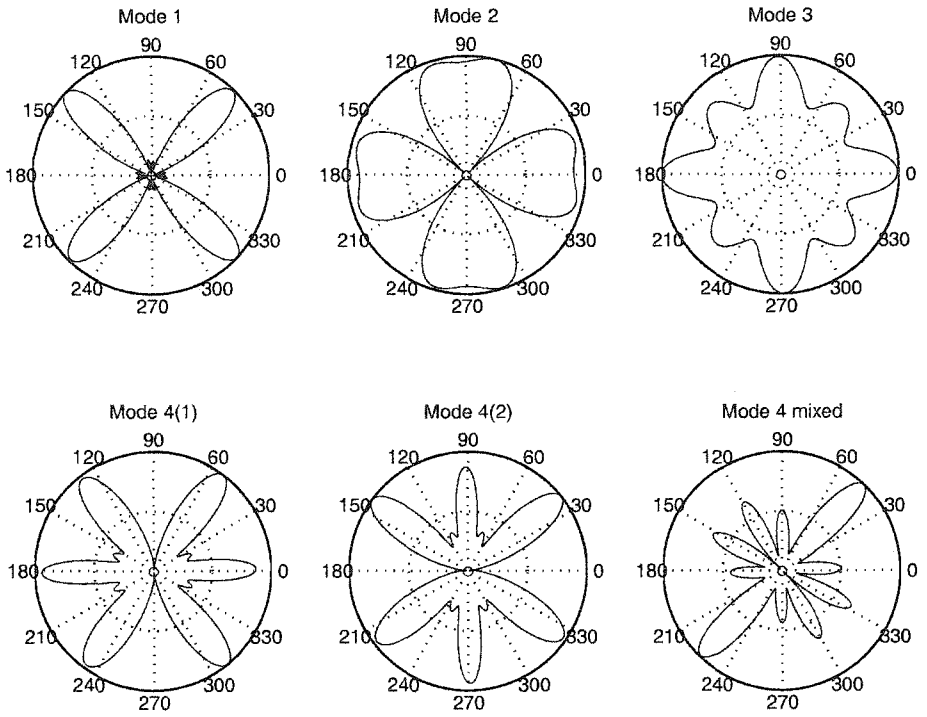

Figure 75. Far field pattern of the four defect modes in the cavity. Note mode 4(1) is excited using a 0° incidence and mode 4(2) is excited using a 90° incidence. The mixed is excited using a 45° incidence. The pattern is also dependent on its quality factors, for higher Q values, it will be more direction dependent.

The defect mode evolution can be obtained using a narrow bandwidth Butterworth digital filter. The obtained signals are shown in Figure 76 (60° incidence is used here). The evolution for mode 4 are calculated separately using the 0° and 90° incidence so we can get the Q information for each of them. As seen from the figure, the field in the defect is enhanced at those eigen frequencies due to the coherent interference in the microcavity. After the excitation is gone, the resonant mode can reach steady state and energy decays in an exponentially way. We can easily evaluate the decay rate and the quality factor of the micro-cavity or the Q values.

Reproduced with permission of the copyright owner. Further reproduction prohibited without permission.

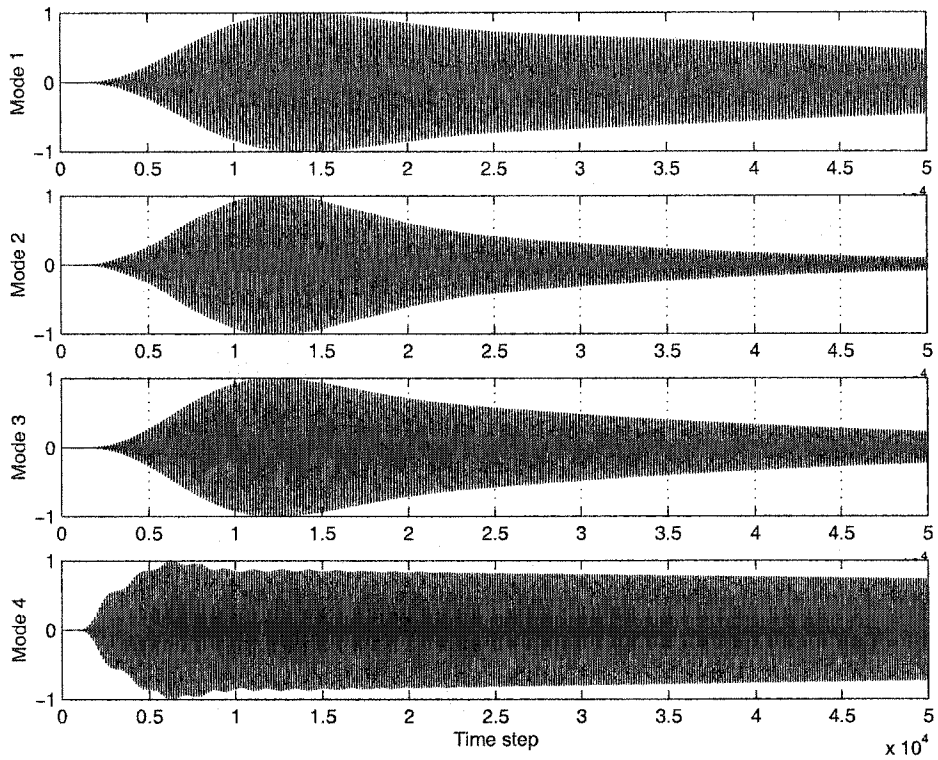

Figure 76. The mode evolution of each resonant modes, which can yield the quality factors of them.

The quality factor Q can be roughly estimated using the above figures. the energy in the micro-cavity decays in the form of $e^{-\frac{\omega_0}{Q}t}$, so the E field amplitude will decay in a form of $e^{-\frac{\omega_0}{2Q}t}$. Therefore, Q can be evaluated using $Q = -\frac{\omega_0(t_1 - t_0)\Delta t}{2\ln E_1/E_0}$ supposing we know the amplitudes E_1 and E_0 at time t_1 and t_0. Taking mode 1 as an example, it reaches an amplitude E_0=1.0 at t_0=7500 time steps, and its amplitude decays to E_1=0.40 at time step t_1=50,000. This gives us a value of 764. The Q values for mode 2, 3 and 4 are calculated the same way and they are 276, 466 and 2936, respectively. The two degenerate modes and the mixed mode 4 have similar quality factors or Q values.

5.4.2 Finite PBG waveguiding

Line defect is another important defect in PBG devices since it can act as a waveguide. Figure 77 shows such a waveguide, the cladding area consists of a 2D square lattice of periodic GaAs rods, and the core is formed by removing the center row of GaAs rods. The mode will be

Reproduced with permission of the copyright owner. Further reproduction prohibited without permission.

confined by photonic band gap effect and will be guided in the air core. The core can also be other form of higher index or lower index area.

The finite PBG device is composed of 11x11 rod with the center row of rods being removed. The parameter is the same as the above section: R/a=0.20, ε_a=11.56, a=1μm. The whole space is cut into a 440x440 mesh, with Δx=Δy=0.025μm, Δt=4e-11μs and number of time steps is 3,000. A continuous point source is located right at the center of the entry. This source will emit a continuous, monochromatic sine wave with frequency f=1.05e14Hz, or λ=2.8571μm, the normalized frequency a/λ=0.3500 is in the band gap and could form a guide mode, see Chapter 3.

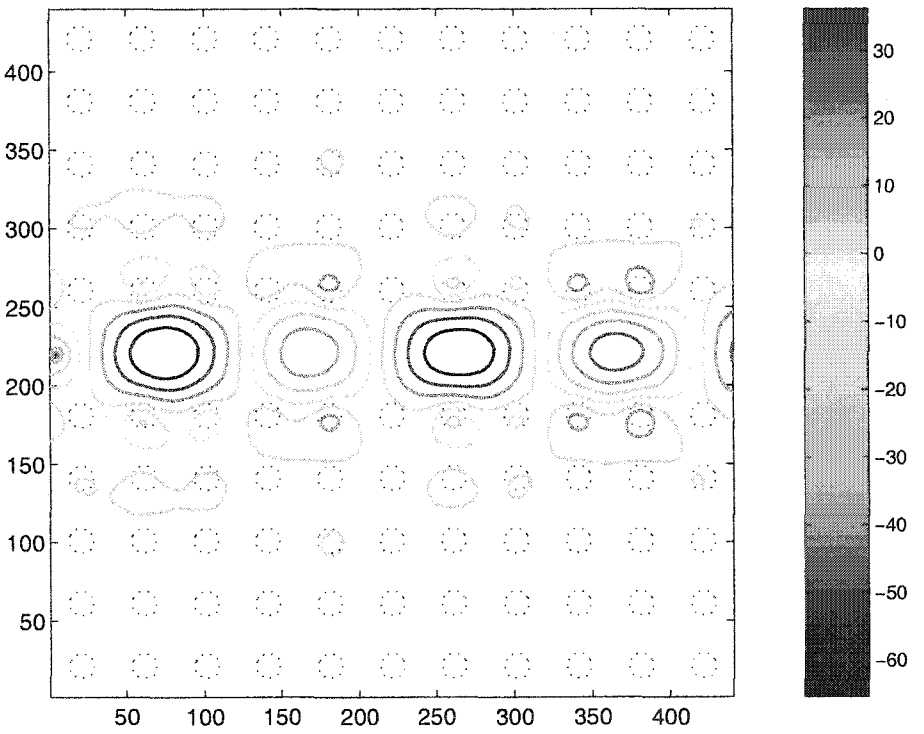

Figure 77. The PBG waveguide. A point source emits a monochromatic sine wave with a/λ=0.3500.

As is seen in Figure 77, though the point source emits uniformly in all directions, the forward semi-sphere is confined well in the waveguide. The wave vector k can be obtained from the well-formed field pattern. Also from the figure, we can see that the field is well confined in the range from above 3 rows of rods to the down 3 rows of rods, which means that to minimize the interference between neighboring channels, the separation should be about 5-6 rows. If a short

Reproduced with permission of the copyright owner. Further reproduction prohibited without permission.

pulse with wide bandwidth is sent, those frequencies outside the bandgap will become radiation soon, acting as an ideal band filter.

5.4.3 Finite PBG sharp bending

A sharp bend is formed in the same PBG structure by removing half a row and half a column rods. The parameters are all the same as the above section and the region size is 11ax11a. A point source emits a continuous monochromatic sine wave, it forms a guide mode in the waveguide, and this guide mode can pass the sharp bend with very low loss. The bend is 90 degrees and is comparable to the light wavelength.

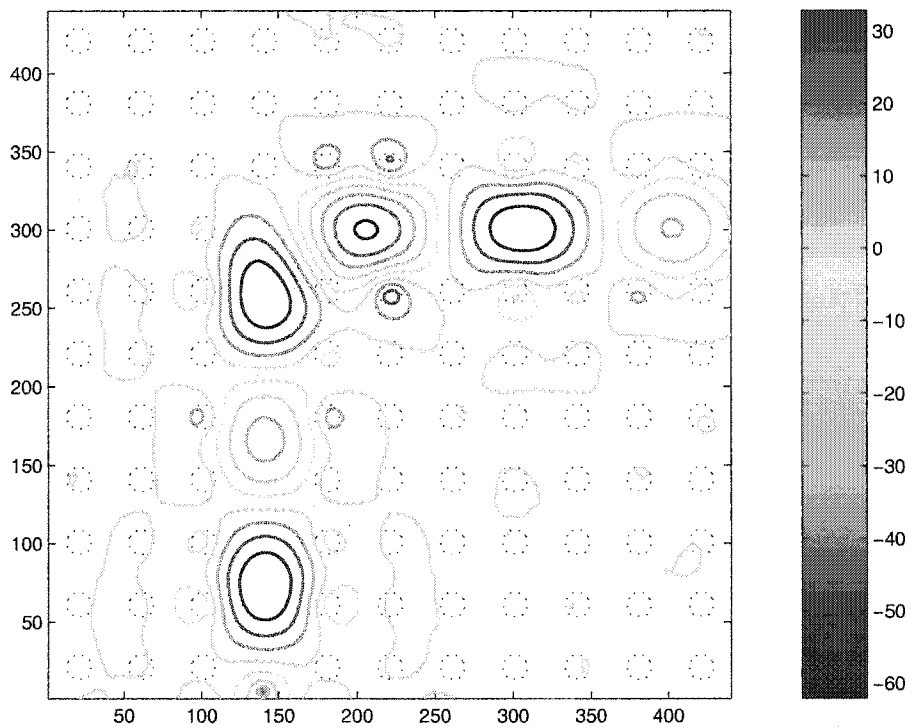

Figure 78. A sharp PBG bending, guide mode can pass the sharp bend with very low loss and high efficiency.

There will be no radiation loss at the corner since the light cannot pass through the bulk material due to the band gap. Only back reflection by the corner may affect the transmission efficiency. The overall efficiency can be over 80%. This can be compared with ~30% transmission efficiency in a similar high index dielectric waveguide bend.

A remarkable feature of this kind sharp bending is that light at some wavelengths can have 100% transmission. This happens when resonant coupling between the traveling wave along

Reproduced with permission of the copyright owner. Further reproduction prohibited without permission.

<10> and <11>, which can be modeled using a 1D scatter problem. The light in the horizontal and vertical waveguide has the same dispersion, however, different for the short waveguide along <11> direction. Assuming the dispersion for the x or y direction is $k_1(f)$, and $k_2(f)$ for <11> direction, the reflection coefficient is expressed as [13, 15-17]: $R(f)=16\left(\frac{k_1-k_2}{k_1+k_2}\right)^2 \sin^2(k_2 L)$ where L is the length of <11> waveguide section.

5.4.4 Add/drop filter for WDM applications

As mentioned in Chapter III, waveguides composed of periodically point defects can act as a narrow band waveguide, which can be a candidate of add/drop channel for WDM applications. A design of such device is shown in Figure 79. It contains one bus and three drop in a 2D square lattice with circular alumina rods (R=0.20a). The bus waveguide is composed a line defect with the center rod removed. Three drop-channels are constructed by periodic point defects separated by two rods, and each channel is separated by four columns. In waveguide 1, the defect is formed by removing the rod; in waveguide 2, the defect is formed by a rod with reduced dielectric constant of 4.9; in waveguide 3, the defect is formed by an increased dielectric constant of 11.56. A frequency domain analysis (see Figure 28 and Figure 29) shows the defect frequency for these stand alone cavities is 0.39 (monopole) for the first one, 0.34 (monopole) for the second one and no modes in the third one. Same discretization resolution and time parameters as above are used for simulation. A point source is located at the entrance of the bus and emits a Gaussian pulse. Five detectors are placed in the four ends of the bus and drop-channels, one after the source to monitor the pulse.

The result shows the drop-channel can draw the signal from the bus-channel efficiently. However, the channel 3 with higher index rods does not drop any signal from the bus in the whole spectrum (limited in the band gap) since it is not sufficient to support the monopole mode. Channel 3 is an index guiding waveguide that supports mode in a low frequency region.

Reproduced with permission of the copyright owner. Further reproduction prohibited without permission.

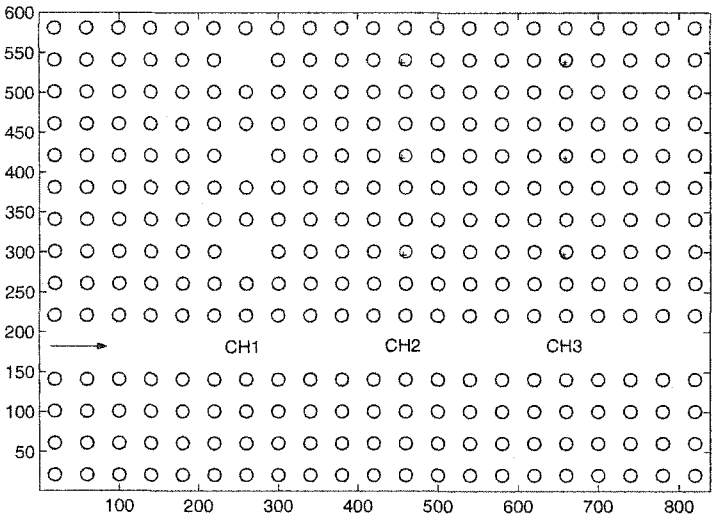

Figure 79. Multiple channel drop for WDM applications. Channel 1 removes 3 rods, channel 2 reduces the dielectric constants, channel 3 increases the dielectric constants.

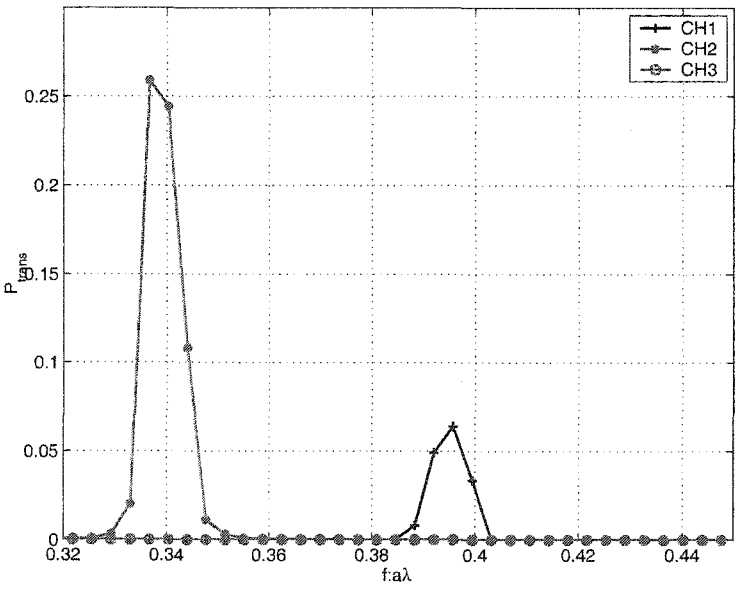

Figure 80. The spectrum of the three drop channels. The channel with high index rods doesn't couple any energy from the bus channel.

Reproduced with permission of the copyright owner. Further reproduction prohibited without permission.

5.5 Discussion

FDTD is proved powerful in treating PBG devices. The discussions covered many important applications. However, 3D applications are not done. Other geometries such as coaxial structures need FDTD in cylindrical coordination.

Analysis is focused on spectral information; some quantities such as the power delivered are not yet included. These quantities are important to discuss the transmission efficiency of waveguiding or bending. The Q values and mode spectral widths obtained are highly sensitive to numerical quantities, and so are not very accurate.

Reproduced with permission of the copyright owner. Further reproduction prohibited without permission.

CHAPTER VI

SUMMARY AND FUTURE WORK

We have studied and analyzed the photonic band gap materials using several analysis techniques, including mainly the plane wave method and FDTD. Photonic crystal fiber is analyzed separately since it develops in its own way.

The frequency domain method using plane wave expansion is carefully discussed and implemented using MATLAB. The computation increases exponentially with supercell size and number of plane waves. The accuracy of the eigen-frequencies is important and mode properties is especially useful for device designs.

Basic structures in two-dimensional planar devices are studied. Two polarizations TE and TM mode are independent. Complete band gap does not exist in square lattice with dielectric rods in air, but does for more complex structures. The band gap is strongly dependent on the dielectric constant ratio, filling ratio, and lattice geometry. Point defects introduced in the structure can generate localized states in band gap. These states can be classified as donors and acceptors, depending on whether they are from the band top or bottom. These states are independent of the wave vectors and are confined in the cavity, and the degree of confinement (measured by the imaginary k-vector) is directly related to the position of the frequency in the gap and its mode pattern or its angular momentum. Line defects can form waveguiding, and the dispersion relation can be obtained from the band structure. These waveguides can be linear, have very small dispersion, and have the capability to carry large power in air.

Interactions between defects are discussed in two-dimensional planar device. Coupling is not negligible when neighboring defects exist. This coupling effect decreases exponentially with the distance. When phase matches or modes reach resonant condition, highly efficient energy transfer can occur through tunneling process.

Photonic crystal fibers are evolving into several types, including the all-single mode holey fiber, hollow fiber possessing band gaps, and Bragg fibers. They are the most feasible photonic crystal based devices so far. The propagation property and modes are analyzed in detail.

FDTD can be a compensation tool for photonic crystal modeling. Furthermore, it can act as a powerful simulation tool to verify designs. Perfectly matched layer boundary condition and dispersion control are important for achieving accurate simulation.

More theoretical work is needed to reach a better understanding of the interaction between defects. Nonlinear effects and quantum effects are also of interest and are not covered. Calculation is still a burden for complex systems, and new algorithms are expected to improve the

Reproduced with permission of the copyright owner. Further reproduction prohibited without permission.

computing efficiency. Further work may still be needed to study modes in photonic crystal fiber, such as the mode field diameter, polarization dispersion, confinement loss, etc. The capability of FDTD for dealing with different coordinations and different dimensions is currently limited and more work is required in improving efficiency and providing capability to normalize some quantities.

Reproduced with permission of the copyright owner. Further reproduction prohibited without permission.

APPENDIX I. DERIVATION OF PLANE WAVE METHOD

First, we have:

$$\nabla\times\left[\frac{1}{\varepsilon}\nabla\times H(r)\right]=\frac{\omega^2}{c^2}H(r) \tag{A1-1}$$

$$H(r)=\sum_{G,\lambda}h_{G\lambda}\hat{e}_\lambda e^{i(k+G)r} \tag{A1-2}$$

$$\frac{1}{\varepsilon}=\sum_{G}\varepsilon_G^{-1}e^{iG\cdot r} \tag{A1-3}$$

Apply (A1-2, A1-3) into (A1-1), the left hand side is:

$$\begin{aligned}
LHS &= \nabla\times\left[\frac{1}{\varepsilon}\nabla\times\sum_{G\lambda}h_{G\lambda}\hat{e}_\lambda e^{i(k+G)r}\right]\\
&= \nabla\times\left[\frac{1}{\varepsilon}\sum_{G\lambda}h_{G\lambda}\hat{e}_\lambda\times\nabla e^{i(k+G)r}\right]\\
&= \nabla\times\left[\frac{1}{\varepsilon}\sum_{G\lambda}h_{G\lambda}\hat{e}_\lambda\times i(k+G)e^{i(k+G)r}\right]\\
&= \nabla\times\left[\sum_{G'}\varepsilon_{G'}^{-1}e^{iG'r}\sum_{G\lambda}h_{G\lambda}\hat{e}_\lambda\times i(k+G)e^{i(k+G)r}\right]\\
&= \nabla\times\left[\sum_{G'}\sum_{G\lambda}\varepsilon_{G'}^{-1}h_{G\lambda}\hat{e}_\lambda\times i(k+G)e^{i(k+G+G')r}\right]\\
&= \sum_{G'}\sum_{G\lambda}\varepsilon_{G'}^{-1}h_{G\lambda}\hat{e}_\lambda\times i(k+G)\times\nabla e^{i(k+G+G')r}\\
&= \sum_{G'}\sum_{G\lambda}\varepsilon_{G'}^{-1}h_{G\lambda}\hat{e}_\lambda\times i(k+G)\times i(k+G+G')e^{i(k+G+G')r}\\
&= \sum_{G'}\sum_{G\lambda}\varepsilon_{G'}^{-1}h_{G\lambda}(k+G)\times\hat{e}_\lambda\times(k+G+G')e^{i(k+G+G')r}
\end{aligned} \tag{A1-4}$$

let $G''=G+G'$, then $G'=G''-G$, the above equation is:

$$\begin{aligned}
LHS &= \sum_{G''-G}\sum_{G\lambda}\varepsilon_{G''-G}^{-1}h_{G\lambda}(k+G)\times\hat{e}_\lambda\times(k+G'')e^{i(k+G'')r}\\
&= \sum_{G\lambda}\sum_{G'-G}\varepsilon_{G'-G}^{-1}h_{G\lambda}(k+G)\times\hat{e}_\lambda\times(k+G')e^{i(k+G')r}
\end{aligned} \tag{A1-5}$$

Since $G'-G$ and G is the same set of grid vectors,

$$LHS=\sum_{G\lambda}\sum_{G'}\varepsilon_{G'-G}^{-1}h_{G\lambda}(k+G)\times\hat{e}_\lambda\times(k+G')e^{i(k+G')r} \tag{A1-6}$$

exchange G and G':

Reproduced with permission of the copyright owner. Further reproduction prohibited without permission.

$$LHS = \sum_{G'\lambda'} \sum_{G} \varepsilon^{-1}_{G-G'} h_{G'\lambda'} (k+G') \times \hat{e}_{\lambda'} \times (k+G) e^{i(k+G)r} \tag{A1-7}$$

Now the right hand side:

$$RHS = \frac{\omega^2}{c^2} \sum_{G\lambda} h_{G\lambda} \hat{e}_{\lambda} e^{i(k+G)r} \tag{A1-8}$$

Equating each plane wave with $e^{i(k+G)r}$ in the right and left side, we have:

$$\sum_{G'\lambda'} \varepsilon^{-1}_{G-G'} h_{G'\lambda'} \hat{e}_{\lambda} \cdot [(k+G') \times \hat{e}_{\lambda'} \times (k+G)] = \frac{\omega^2}{c^2} h_{G\lambda} \hat{e}_{\lambda} \tag{A1-9}$$

This becomes a standard eigen-value problem:

$$\sum_{G'\lambda'} \varepsilon^{-1}_{G-G'} h_{G'\lambda'} [(k+G') \times \hat{e}_{\lambda'}] \cdot [(k+G) \cdot \hat{e}_{\lambda}] = \frac{\omega^2}{c^2} h_{G\lambda} \tag{A1-10}$$

Reproduced with permission of the copyright owner. Further reproduction prohibited without permission.

APPENDEX II. DERIVATION OF THE PCF ALGORITHM USING E

The vectorial wave equation for E_t:

$$\left(\nabla_t^2 + k_0^2\varepsilon\right)E_t + \nabla_t\left(E_t \cdot \nabla_t \ln\varepsilon\right) = \beta^2 E_t \tag{A2-1}$$

with:
$$E_t = \sum_G \left(E_{Gx}\hat{x} + E_{Gy}\hat{y}\right)e^{i\vec{G}\cdot\vec{r}} \tag{A2-2}$$

and
$$\varepsilon = \sum_G \varepsilon_G e^{iG\cdot r}, \ln\varepsilon = \sum_G \kappa_G e^{iG\cdot r} \tag{A2-3}$$

Then we have:

$$\begin{aligned}
\nabla_t\left(E_t \cdot \nabla_t \ln\varepsilon\right) &= \nabla_t\left[\sum_G \left(E_{Gx}\hat{x} + E_{Gy}\hat{y}\right)e^{i\vec{G}\cdot\vec{r}} \cdot \nabla_t \sum_{G'} \kappa_{G'} e^{i\vec{G}'\cdot\vec{r}}\right] \\
&= \nabla_t\left[\sum_G \left(E_{Gx}\hat{x} + E_{Gy}\hat{y}\right)e^{i\vec{G}\cdot\vec{r}} \cdot \sum_{G'} \kappa_{G'} i\vec{G}' e^{i\vec{G}'\cdot\vec{r}}\right] \\
&= \nabla_t\left[\sum_G \sum_{G'} \left(E_{Gx}G'_x + E_{Gy}G'_y\right)i\kappa_{G'} e^{i\left(\vec{G}+\vec{G}'\right)\vec{r}}\right] \\
&= -\sum_G \sum_{G'} \left(E_{Gx}G'_x + E_{Gy}G'_y\right)\kappa_{G'}\left(\vec{G}+\vec{G}'\right)e^{i\left(\vec{G}+\vec{G}'\right)\vec{r}}
\end{aligned} \tag{A2-4}$$

let $G' \Rightarrow \vec{G} + \vec{G}'$, and exchange G and G', then the above equation is:

$$\begin{aligned}
&= -\sum_G \sum_{G'} \left[E_{Gx}\left(G'_x - G_x\right) + E_{Gy}\left(G'_y - G_y\right)\right]\kappa_{\vec{G}'-G}\vec{G}' e^{i\vec{G}'\cdot\vec{r}} \\
&= -\sum_G \sum_{G'} \left[E_{G'x}\left(G_x - G'_x\right) + E_{G'y}\left(G_y - G'_y\right)\right]\kappa_{\vec{G}-\vec{G}'}\left(G_x\hat{x} + G_y\hat{y}\right)e^{i\vec{G}\cdot\vec{r}} \\
&= -\sum_G \sum_{G'} \left[\kappa_{\vec{G}-\vec{G}'}\left(G_x - G'_x\right)E_{G'x} + \kappa_{\vec{G}-\vec{G}'}\left(G_y - G'_y\right)E_{G'y}\right]\left(G_x\hat{x} + G_y\hat{y}\right)e^{i\vec{G}\cdot\vec{r}}
\end{aligned} \tag{A2-5}$$

$$\begin{aligned}
\left(\nabla_t^2 + k_0^2\varepsilon\right)E_t &= \left(\nabla_t^2 + k_0^2\varepsilon\right)\sum_G \left(E_{Gx}\hat{x} + E_{Gy}\hat{y}\right)e^{i\vec{G}\cdot\vec{r}} \\
&= \sum_G -\left|G\right|^2\left(E_{Gx}\hat{x} + E_{Gy}\hat{y}\right)e^{i\vec{G}\cdot\vec{r}} + k_0^2\sum_G \sum_{G'} \varepsilon_{G-G'}\left(E_{G'x}\hat{x} + E_{G'y}\hat{y}\right)e^{i\vec{G}\cdot\vec{r}}
\end{aligned} \tag{A2-6}$$

So the vectorial wave equation becomes:

$$\begin{aligned}
&\sum_G -\left|G\right|^2\left(E_{Gx}\hat{x} + E_{Gy}\hat{y}\right)e^{i\vec{G}\cdot\vec{r}} + k_0^2\sum_G \sum_{G'} \varepsilon_{G-G'}\left(E_{G'x}\hat{x} + E_{G'y}\hat{y}\right)e^{i\vec{G}\cdot\vec{r}} - \\
&\sum_G \sum_{G'} \left[\kappa_{\vec{G}-\vec{G}'}\left(G_x - G'_x\right)E_{G'x} + \kappa_{\vec{G}-\vec{G}'}\left(G_y - G'_y\right)E_{G'y}\right]\left(G_x\hat{x} + G_y\hat{y}\right)e^{i\vec{G}\cdot\vec{r}} \\
&= \beta^2\sum_G \left(E_{Gx}\hat{x} + E_{Gy}\hat{y}\right)e^{i\vec{G}\cdot\vec{r}}
\end{aligned} \tag{A2-7}$$

Equating each item in the left-hand and the right-hand side:

Reproduced with permission of the copyright owner. Further reproduction prohibited without permission.

$$-|G|^2\left(E_{Gx}\hat{x}+E_{Gy}\hat{y}\right)+k_0^2\sum_{G'}\varepsilon_{G-G'}\left(E_{G'x}\hat{x}+E_{G'y}\hat{y}\right)-$$
$$\sum_{G'}\left[\kappa_{\vec{G}-\vec{G}'}(G_x-G'_x)E_{G'x}+\kappa_{\vec{G}-\vec{G}'}\left(G_y-G'_y\right)E_{G'y}\right]\left(G_x\hat{x}+G_y\hat{y}\right) \qquad \text{(A2-8)}$$
$$=\beta^2\left(E_{Gx}\hat{x}+E_{Gy}\hat{y}\right)$$

Write in a matrix form:

$$\begin{bmatrix}M_1 & M_2\\ M_3 & M_4\end{bmatrix}\begin{bmatrix}E_{G'x}\\ E_{G'y}\end{bmatrix}=\beta^2\begin{bmatrix}E_{Gx}\\ E_{Gy}\end{bmatrix} \qquad \text{(A2-9)}$$

$$M_1=-|G|^2 I+k_0^2\varepsilon(G-G')-\kappa(G-G')(G_x-G'_x)G_x \qquad \text{(A2-10)}$$

$$M_2=-\kappa(G-G')(G_y-G'_y)G_x \qquad \text{(A2-11)}$$

$$M_3=-\kappa(G-G')(G_x-G'_x)G_y \qquad \text{(A2-12)}$$

$$M_4=-|G|^2 I+k_0^2\varepsilon(G-G')-\kappa(G-G')(G_y-G'_y)G_y \qquad \text{(A2-13)}$$

Reproduced with permission of the copyright owner. Further reproduction prohibited without permission.

APPENDIX III. DERIVATION OF THE PCF ALGORITHM USING H

For H_t:

$$\left(\nabla_t^2 + k_0^2\varepsilon\right)H_t + \nabla_t \ln\varepsilon \times \left(\nabla_t \times H_t\right) = \beta^2 H_t \tag{A3-1}$$

$$H_t = \sum_G \left(H_{Gx}\hat{x} + H_{Gy}\hat{y}\right)e^{i\vec{G}\cdot\vec{r}} \tag{A3-2}$$

Apply the property of $\nabla\times(\varphi\vec{a}) = \varphi\nabla\times\vec{a} + \nabla\varphi\times\vec{a}$ and $\nabla e^{i\vec{G}\cdot\vec{r}} = i\vec{G}e^{i\vec{G}\cdot\vec{r}}$:

$$\begin{aligned}
\nabla_t \ln\varepsilon \times \left(\nabla_t \times H_t\right) &= \nabla_t \ln\varepsilon \times \left[\nabla_t \times \sum_G \left(h_{Gx}\hat{x} + h_{Gy}\hat{y}\right)e^{i\vec{G}\cdot\vec{r}}\right] \\
&= -\nabla_t \ln\varepsilon \times \left[\sum_G \left(h_{Gx}\hat{x} + h_{Gy}\hat{y}\right)\times\nabla_t e^{i\vec{G}\cdot\vec{r}}\right] \\
&= -\nabla_t \ln\varepsilon \times \left[\sum_G \left(h_{Gx}\hat{x} + h_{Gy}\hat{y}\right)\times i\vec{G}e^{i\vec{G}\cdot\vec{r}}\right] \\
&= -\nabla_t \ln\varepsilon \times \sum_G \left(h_{Gx}G_y - h_{Gy}G_x\right)e^{i\vec{G}\cdot\vec{r}}i\hat{z} \\
&= -\nabla_t \sum_{G'} \kappa_{G'}e^{i\vec{G}'\cdot\vec{r}} \times \sum_G \left(h_{Gx}G_y - h_{Gy}G_x\right)e^{i\vec{G}\cdot\vec{r}}i\hat{z} \\
&= -\sum_{G'} \kappa_{G'}i\vec{G}'e^{i\vec{G}'\cdot\vec{r}} \times \sum_G \left(h_{Gx}G_y - h_{Gy}G_x\right)e^{i\vec{G}\cdot\vec{r}}i\hat{z} \\
&= \sum_G\sum_{G'} \kappa_{G'}\left(h_{Gx}G_y - h_{Gy}G_x\right)e^{i\left(\vec{G}+\vec{G}'\right)\vec{r}}\vec{G}'\times\hat{z} \\
&= -\sum_G\sum_{G'} \kappa_{G'}\left(h_{Gy}G_x - h_{Gx}G_y\right)e^{i\left(\vec{G}+\vec{G}'\right)\vec{r}}\left(G'_y\hat{x} - G'_x\hat{y}\right)
\end{aligned} \tag{A3-3}$$

Replace G+G' with G' and then exchange G and G':

$$\begin{aligned}
&= -\sum_G\sum_{G'} \kappa_{G'-G}\left(h_{Gy}G_x - h_{Gx}G_y\right)\left[\left(G'_y - G_y\right)\hat{x} - \left(G'_x - G_x\right)\hat{y}\right]e^{i\vec{G}'\cdot\vec{r}} \\
&= -\sum_G\sum_{G'} \kappa_{G-G'}\left(h_{G'y}G'_x - h_{G'x}G'_y\right)\left[\left(G_y - G'_y\right)\hat{x} - \left(G_x - G'_x\right)\hat{y}\right]e^{i\vec{G}\cdot\vec{r}}
\end{aligned} \tag{A3-4}$$

The wave equation for H_t will be:

$$\begin{aligned}
&\sum_G -|G|^2\left(H_{Gx}\hat{x} + H_{Gy}\hat{y}\right)e^{i\vec{G}\cdot\vec{r}} + k_0^2\sum_G\sum_{G'}\varepsilon_{G-G'}\left(H_{G'x}\hat{x} + H_{G'y}\hat{y}\right)e^{i\vec{G}\cdot\vec{r}} - \\
&\sum_G\sum_{G'} \kappa_{\vec{G}-G'}\left(h_{G'y}G'_x - h_{G'x}G'_y\right)\left[\left(G_y - G'_y\right)\hat{x} - \left(G_x - G'_x\right)\hat{y}\right]e^{iG\cdot\vec{r}} \\
&= \beta^2\sum_G \left(H_{Gx}\hat{x} + H_{Gy}\hat{y}\right)e^{i\vec{G}\cdot\vec{r}}
\end{aligned} \tag{A3-5}$$

Equating each item in the left-hand and the right-hand side:

Reproduced with permission of the copyright owner. Further reproduction prohibited without permission.

$$
\begin{aligned}
&-|G|^2\left(H_{Gx}\hat{x}+H_{Gy}\hat{y}\right)+k_0^2\sum_{G'}\varepsilon_{G-G'}\left(H_{G'x}\hat{x}+H_{G'y}\hat{y}\right)- \\
&\sum_{G'}\kappa_{G-G'}\left(h_{G'y}G'_x-h_{G'x}G'_y\right)\left[\left(G_y-G'_y\right)\hat{x}-\left(G_x-G'_x\right)\hat{y}\right] \\
&=\beta^2\left(H_{Gx}\hat{x}+H_{Gy}\hat{y}\right)
\end{aligned}
\tag{A3-6}
$$

Write in a matrix form:

$$
\begin{bmatrix} M_1 & M_2 \\ M_3 & M_4 \end{bmatrix}\begin{bmatrix} h_{G'x} \\ h_{G'y} \end{bmatrix}=\beta^2\begin{bmatrix} h_{Gx} \\ h_{Gy} \end{bmatrix} \tag{A3-7}
$$

$$
M_1=-|G|^2 I+k_0^2\varepsilon(G-G')+\kappa(G-G')\left(G_y-G'_y\right)G'_y \tag{A3-8}
$$

$$
M_2=-\kappa(G-G')\left(G_y-G'_y\right)G'_x \tag{A3-9}
$$

$$
M_3=-\kappa(G-G')\left(G_x-G'_x\right)G'_y \tag{A3-10}
$$

$$
M_4=-|G|^2 I+k_0^2\varepsilon(G-G')+\kappa(G-G')\left(G_x-G'_x\right)G'_x \tag{A3-11}
$$

Reproduced with permission of the copyright owner. Further reproduction prohibited without permission.

REFERENCES

1. P. Yeh, A. Yariv, and C. Hong, J. Opt. Soc. Am. **67**, 423 (1977).
2. E. Yablonovitch, Phys. Rev. B **72**, 187 (1987).
3. E. Yablonovitch, Phys. Rev. Lett. **58**, 2059 (1987).
4. S. John, Phys. Rev. Lett. **58**, 2486 (1987).
5. J. D. Joannopoulos, R. D. Meade, and J. N. Winn, *Photonic crystals - Molding the flow of light* (Princeton University Press, 1995).
6. C. M. Soukoulis Ed., *Photonic band gap materials* (Kluwer Academic Publisher, 1996).
7. C. M. Bowden and J. P. Dowling Ed., Photonic band gaps: development and applications of materials exhibiting photonic band gaps, J. Opt. Soc. Am. B**10** (1993).
8. A. Scherer Ed., Electromagnetic crystal structures: design, synthesis, and applications, J. Lightwave Technol. **17** (1999).
9. A. Scherer Ed., *Photonic crystal in microwave,* IEEE trans. on MTT. (1999).
10. K. M. Ho, C. T. Chan, and C. M. Soukoulis, Phys. Rev. Lett. **65**, 3152 (1990).
11. K. M. Leung and Y. F. Liu, Phys. Rev. Lett. **65**, 2646 (1990).
12. K. M. Ho, C.T. Chan, and C. M. Soukoulis, in *Photonic band gaps and localization*, C. M. Soukoulis Ed., (Plenum Press, New York, 1993).
13. E. Chow, S. Y. Lin, S. G. Johnson, J. D. Joannopoulos, Opt. Lett. **26**, 286 (2001).
14. R. L. Espinola, R. U. Ahmad, F. Pizzuto, M. J. Steel, and R. M. Osgood, Opt. Express **8**, 517 (2001).
15. S. Lin, E. Chow, V. Hietala, P. R. Villeneuve, and J. D. Joannopoulos, Science **282,** 274 (1998).
16. R. D. Meade, A. Devenyi, and J.D. Joannopoulos, J. Appl. Phys. **75**, 4753 (1994).
17. A. Mekis, J. C. Chen, I. Kurland, S. Fan, P. R. Villeneuve, and J. D. Joannopoulos, Phys. Rev. Lett. **77**, 3787 (1996).
18. R. Coccioli, M. Boroditsky, K. W. Kim, Y. Rahmat-Samii, E. Yablonovitch, http://www.ee.ucla.edu/labs/photon/preprints/modeopt.pdf (2000).
19. O. Painter and R. K. Lee, *Two-dimensional photonic crystal nanocavity lasers*, MURI annual report: http://www.ee.ucla.edu/labs/photon/ (1998).
20. R. K. Lee and O.Painter, J. Opt. Soc. Am. B**17**, 629 (2000).
21. E. R. Brown, C.D.Parker, E. Yablonovitch, J. Opt. Soc. Am. B**10**, 404 (1993).
22. E. R. Brown, C.D.Parker, O. B. McMahon, Appl. Phys. Lett. **64**, 3345 (1994).

Reproduced with permission of the copyright owner. Further reproduction prohibited without permission.

23. Y. Rahmat-Samii, *Antenna Systems for Current Generation Precision GPS*, in Photonic Band Engineering MURI Annual Review Meeting: http://www.ee.ucla.edu/labs/photon/ (1999).
24. R. G. P. Maagt and M. Sorlla., IEEE trans. MTT. **47, No. 11** (1999).
25. M. Thevenot, IEEE Trans. MTT. **47, No.** 11 (1999).
26. M. Meier, A. Dodabalapur, and J. A. Rogers, J. Appl Phys. **86**, 3502 (1999).
27. A. Mekis, M. Meier, A. Dodabalapur, R. E. Slusher, J. D. Joannopoulos, Appl. Phys. A **69,** 111 (1999).
28. O. Painter and R. K. Lee, Science **284,** 1819 (1999).
29. A. Scherer, J. L. Jewell, J.P. Harbison, Optics and Photonics News **2**, 9 (1991).
30. T. Søndergaard, J. Lightwave Technol. **18**, 589 (2000).
31. S. Fan, PhD Dissertation, in Department of Physics. MIT (1997).
32. M. Boroditsky, T. F. Krauss, R. Coccioli, R. Vrijen, R. Bhat, and E. Yablonovitch, Appl. phys. lett. **75**, 1036 (1999).
33. S. Fan, P. R. Villeneuve, and J. D. Joannopoulos, Opt. Express **3**, 4 (1998).
34. S. Fan and P. R. Villeneuve, Phys. Rev. Lett. **80**, 960 (1998).
35. S. Fan, P. R. Villeneuve, and J. D. Joannopoulos, Phys. Rev. B **59**, 15882 (1999).
36. F. Yang, IEEE trans. MTT. **47** (1999).
37. C. Jin, B. Cheng, B. Man, Z., and D. Zhang, Appl. Phys. lett. **75**(13), 1848 (1999).
38. S. Y. Lin, Opt. Lett. **25**, 1297 (2000).
39. J. B. Nielsen, IEEE Photonic technology lett, **12**, 630 (2000).
40. S. G. Johnson, P. R. Villeneuve, S. Fan, and J. D. Joannopoulos, Phys. Rev. B **62**, 8212 (2000).
41. E. Silvestre, J. M. Pottage, and P. S. J. Russel, Appl. Phys. Lett. **77**, 942 (2000).
42. S. G. Johnson, C. Manolatou, S. Fan, R. Villeneuve, J. D. Joannopoulos, H. A. Haus, Opt. Lett. **23**, 1855 (1998).
43. T. A. Birks, J. C. Knight, and P. S. J. Russel, Opt. Lett. **22**, 961 (1997).
44. J. Broeng, S. E. Barkou, T. Sndergaard, and A. Bjarklev, Opt. Lett. **25**, 96 (2000).
45. R. K. Lee, Y. Xu, and A. Yariv, J. Opt. Soc. Am. B **17**, 1438 (2000).
46. T. Quang, M. Woldeyohannes, and S. John, Phys. Rev. Lett. **79**, 5238 (1997).
47. S. John and J. Wang, Phys. Rev. Lett. **64**, 2418 (1990).
48. S. John and T. Quang, Phys. Rev. Lett. **76**, 1320 (1996).
49. S. Saltiel and Y.S. Kivshar, Opt. Lett. **25**, 1204 (2000).
50. P. Tran, Opt. Lett. **21**, 1138 (1996).
51. K. M. Engenhardt and S. Gregory, J. Opt. Soc. Am. B**17**, 593 (2000).

Reproduced with permission of the copyright owner. Further reproduction prohibited without permission.

52. H. F. Ghaemi, T. Thio, and D. E. Grupp, Phys. Rev. B **58**, 6779 (1998).
53. S. Y. Lin and J. G. Fleming, J. Lightwave Technol. **17**, 1944 (1999).
54. K. Busch and S. John, Phys. Rev. E **58**, 3896 (1998).
55. S. Rowson, A. Chelnokov, J. Lightwave Technol. **17**, 1989 (1999).
56. M. Born and E. Wolf, *Principle of Optics,* (Pergamon, Oxford, 1959).
57. J. B. Pendry and P. M. Bell, in *Photonic band gaps and localization*, C. M. Soukoulis Ed., (Plenum Press, NY., 1993).
58. K. Busch, C. T. Chan, and C. M. Soukoulis, in *Photonic band gap materials*, Ed. by C. M. Soukoulis (Plenum Press, NY., 1996).
59. J. Yonekura, J. Lightwave Technol. **17**, 1500 (1999).
60. K. M. Leung, in *Photonic band gaps and localizations*, Ed. by C.M. Soukoulis, (Plenum Press, NY., 1993).
61. E. Yablonovitch, T. J. Gmitter, and K. M. Leung, Phys. Rev. B **67**, 2295 (1991).
62. A. Mekis, S. Fan, and J. D. Joannopoulos, IEEE Microwave & Guided wave letters, **9**, 502 (1999).
63. F. Brechet, J. Marcou, D. Pagnoux, Opt. Fiber Technol. **6,** 181 (2000).
64. A. Figotin and Y.A. Godin, J. Comp. Phys. **136,** 585 (1997).
65. D. C. Champeney, *Fourier transforms and their physical applications*, Ed. G. K. T. Conn and K.R. Coleman (Academic Press, 1973).
66. A. J. Ward and J. B. Pendry, J. Modern Optics **43,** 773 (1996).
67. G. Arfken, *Mathematical methods for physicists*, (Academic press, 1985).
68. M. Plihal and A.A. Maradudin, Phys. Rev. B **44**, 8565 (1991).
69. R. D. Meade, A. M. Rappe, K. D. Brommer, and J. D. Joannopoulos, Phys. Rev. B **48**, 8434 (1993).
70. S. G. Johnson and J.D. Joannopoulos, Opt. Express **8**, 173 (2001).
71. A. Brandt and S. McCormick, SIAM J. Sci. Stat. Comput. **4,** 244 (1983).
72. D. Hermann, M. Frank, and K. Busch, Opt. Express **8**, 167 (2001).
73. P. R. Villeneuve, S. Fan, and J. D. Joannopoulos, Phys. Rev. B **54**, 7837 (1996).
74. A. A. Maradudin, V. Kuzmiak, and A. R. Ncgurn, in *Photonic band gaps and localizations*, Ed. C M Soukoulis (Plenum Press, NY., 1993).
75. V. Kuzmiak, A. A. Maradudin, and F. Pincemin, Phys. Rev. B **50**, 16835 (1994).
76. M. Qiu and S. He, J. Opt. Soc. Am. B**17**, 1027 (2000).
77. K. Sakoda, Phys. Rev. B **51**, 4672 (1995).
78. K. Sakoda, J. Appl. Phys. **84**, 1210 (1998).

Reproduced with permission of the copyright owner. Further reproduction prohibited without permission.

79. D. Cassagne, C. Jouanin, and D. Bertho, Appl. Phys. Lett. **70**, 289 (1997).
80. K. Sakoda, Phys. Rev. B **52**, 7982 (1995).
81. C. Jin, B. Cheng, B. Man, Z. Li, and D. Zhang, Phys. Rev. B **61**, 10762 (2000).
82. E. Silvestre, Appl. Phys. Lett. **75**, 1848 (1999).
83. M. E. Zoorob, Nature **404,** 740 (2000).
84. J. P. Dowling and C. M. Bowden, J. Opt. Soc. Am. B **10**, 353 (1993).
85. J. C. Knight, T. A. Birks, and P. S. J. Russel, J. Opt. Soc. Am. A**15**, 748 (1998).
86. T. M. Monro, J. Lightwave Technol. **17**, 1093 (1999).
87. A. Ferrando, E. Silvestre, J. J. Miret, P. Andrs, M. V. Andrs, Opt. Lett. **24**, 276 (1999).
88. Z. Zhu and T. G. Brown, Opt. Express **8**, 547 (2001).
89. R. F. Cregan, B. J. Mangan, J. C. Knight, T. A. Birks, P. St. J. Russell, P. J. Roberts, and D. C. Allan, Science **285,** 1537 (1999).
90. R. Ghosh, Electron. Lett., **35**, 1873 (1999).
91. A. Ferrando, Opt. Lett., **25**, 790 (2000).
92. J. P. Berenger, J. Comp. Phys. **114,** 185 (1994).
93. C T Chan, Q. L. Yu, and K.M. Ho, Phys. Rev. B **51**, 16635 (1995).
94. J. Arriaga, A. J. Ward, and J.B. Pendry, Phys. Rev. B **59**, 1874 (1999).
95. M. Qiu, and S. He, J. Appl. Phys. **87**, 8268 (2000).

Reproduced with permission of the copyright owner. Further reproduction prohibited without permission.

VITA

Shangping Guo

Education

- B.S. in Electronic Engineering, Tsinghua University, Beijing 100084 China, 1993
- M.S. in Institute of Lightwave Technology, Northern Jiaotong University, Beijing 100044, China 1996
- Ph,D in Electrical & Computer Engineering, Old Dominion University, USA, 2003.

His main research interests are in theory and simulation on fiber optics, photonic devices, micro-optics and electromagnetics.

Selected publications

1. S. Guo, S. Albin, "Simple plane wave implementation for photonic crystal calculations," Optics Express 11, 167-175 (2003).
2. S. Guo, S. Albin, "Transmission property and evanescent wave absorption of cladded multimode fiber taper," Optics Express 11, 215-223 (2003)
3. S. Guo, S. Albin, "Numerical techniques for excitation and analysis of defect modes in photonic crystals," Optics Express 11, 1080-1089 (2003)
4. Arnel C Larvarias, J. Albin, S. Guo, S. Albin,, "Multimode fiber optic tapers for chemical sensing," 1999 OSA Annual Meeting & Exhibit/ILS-XV: 15th Interdisciplinary Laser Science Conference
5. S. Guo, et al, "Design of a Laser-CCD Scanning Sensor to Measure Moving Object's Profile," Journal of Northern Jiaotong University 20(1) (In Chinese)
6. S. Guo, et al, "A Powerful Tool For Fiber Analysis: Modified Galerkin Method," Journal of Northern Jiaotong University 20(1) (In Chinese)
7. S. Guo, et al, "Propagation Properties of W-fiber," Optical Fiber & Electric Cable (In Chinese)
8. S. Guo, et al, "Calculation of Propagation Parameters of Single Mode Fiber With Arbitrary Index Profile," Optical Communication Technology (In Chinese)
9. S. Guo, et al, "Effect of Outer Index Ring to the Transmission Characteristics of Optical Fiber," 7th China National Conference on Optical Comm. (In Chinese)
10. S. Guo, et al, "Effect of Higher Order Dispersion to the Propagation Characteristics of Single Mode Fiber at Zero-dispersion Wavelength," 7th China National Conference on Optical Comm. (In Chinese)

Reproduced with permission of the copyright owner. Further reproduction prohibited without permission.